Investigating moisture ingress in PV modules

Alternative simulation methods for improved accuracy

Tabitha Minett

Delft University of Technology

TU Delft

Investigating moisture ingress in PV modules

Alternative simulation methods for improved accuracy

by

Tabitha Minett

to obtain the degree of Master of Science at the Delft University of Technology
to be defended publicly on 18th July, 2024 at 14:00.

Chair:	Prof.dr. Arno Smets
Supervisors:	Dr. Malte Vogt
	Youri Blom
External examiner:	Prof.dr. Simon Watson
Project Duration:	December, 2023 - July, 2024
Faculty:	EEMCS
Student number:	4656997

Faculty of Electrical Engineering, Mathematics and Computer Science · Delft University of Technology

TU Delft

Acknowledgements

First, I would like to express my deepest gratitude and appreciation to my supervisors, Malte Vogt and Youri Blom, for their support and guidance throughout this thesis, as well as their kindness and patience. I would like to sincerely thank Arno Smets and Simon Watson for sitting on this thesis assessment committee. Additionally, thank you to Stefaan Heirman and Shuang Hao for their assistance with the planned experiment.

There are numerous people, students, staff, and others, who have enriched my two years at TU Delft; I am very grateful for the opportunities they have provided. To name a few: Boards 13/14 of Delft S.E.A.; fellow 'Solar Engineering' TAs; and the Heliostrome JIP team. They have helped me learn and grow over the last two years, and prepare me for the future.

Lastly, I would like to thank my family, for always supporting me; my friends, for brightening every day; and Emmanuel, for being my rock and cheerleader through it all.

Tabitha Minett
Delft, July 2024

Abstract

Degradation of PV modules reduces their operational lifetime, resulting in an increased levelised cost of electricity (LCOE) and shortening the useful lifetime of valuable materials. One of the leading cause of degradation is moisture. Understanding how this moisture diffuses through PV materials and in different conditions can help prolong modules' lifetime. This thesis investigates moisture ingress in PV modules, specifically looking at alternative, and potentially more accurate, ways of modelling it.

An existing moisture ingress model provides the foundation for this research. It is optimised to ensure it delivers accurate results and adapted to reduce the computational time. Models typically assume Fickian diffusion to simulate moisture ingress; this assumption does not always hold, and deviation between these simulations and experimental results has been reported. Therefore, two mechanisms that are not in the model are explored: non-Fickian diffusion and material degradation. To simulate non-Fickian diffusion, a dual-transport method is used; the study finds the approach to deliver more accurate results for EVA, but not for PET. Optimal non-Fickian factors of NF: 32 and NF: 40 are found, corresponding to units of dimension $(0.625 \times 0.625) \times 10^{-4}$ m^2 and $(0.5 \times 0.5) \times 10^{-4}$ m^2, respectively, which is smaller than that found in literature. To simulate material degradation, an adapted version of the diffusion coefficient equation is proposed, incorporating a degradation constant based on the materials' properties. Degradation constants γ_{EVA} = 0.04 and γ_{PET} = 0.005 are found following a statistical analysis. This constant is able to match the simulation closer to the experimental data.

These findings are then used to analyse the behaviour of other PV materials (TPO and ionomer encapsulants, and TPT and PA backsheets) and behaviour in different climates. The simulations find very slow moisture ingress for ionomer under non-Fickian diffusion and a strong deviation from Fickian diffusion. In EVA/PET simulations, non-Fickian behaviour is found to deviate more from Fickian behaviour in warmer climates. Using an acceleration factor, A_f, to relate accelerated tests and realistic-operation, the degradation constants for EVA and PET are converted for real-world simulations. They are also found for other PV materials, based on their material properties. The approach shows promising results for the TPO/PET and ionomer/PET simulations, showing degradation in proportion with their material properties. However, simulations that include EVA appear to strongly limit moisture diffusion, indicating a revision of the EVA degradation constant should be made. TPO/PET degradation simulations in show minimal degradation over 20 years in different climates, but more material degradation in colder climates is found.

Contents

Nomenclature

Abbreviations

a-Si	Amorphous silicon
ACD	Analog-to-digital converter
c-Si	Crystalline silicon
CdTe	Cadmium telluride
CIGS	Copper indium gallium selenide
EL	Electroluminescence
EVA	Ethylene-vinyl acetate
FEA	Finite-element analysis
FTIR	Fourier-transform infrared spectroscopy
GaAs	Gallium Arsenide
KGC	Köppen-Geiger classification
LCOE	Levelised cost of electricity
LID	Light-induced degradation
MAD	Mean Absolute Difference
MID	Moisture-induced degradation
NF	Non-Fickian factor
PA	Polyamide
PCB	Printed circuit board
PDMS	Polydimethyl siloxane
PET	Polyethylene terephthalate
PIB	Polyisobutylene
PID	Potential-induced degradation
POE	Polyolefin elastomer
PP	Polypropylene
PV	Photovoltaic
PVB	Polyvinyl butyral
PVDF	Polyvinylidene fluoride
PVF	Polyvinyl fluoride
RH	Relative humidity
RMC	Relative moisture content
SCL	Serial clock
SDA	Serial data
TPO	Thermoplastic polyolefin
TPT	Tedlar-Polyester-Tedlar
TPU	Thermoplastic polyurethane
UV	Ultraviolet
VAc	Vinyl acetate
WVTR	Water vapour transmission rate

Symbols

α	Diffusion ratio parameter
β	Degradation factor for realistic-operation
γ	Degradation factor for accelerated tests
ϵ	Dielectric constant ([permittivity) [F/m]
ϵ	Statistical parameter
ν	Wind speed [m/s]
A	Area of plate surface [m^2]
A_f	Acceleration factor
C	Concentration [mol/m^3]
C_0	Capacitance [F]
d	Plate separation [m]
E_a	Activation energy [J/mol]
D	Diffusion coefficient [m^2/s]
D_0	Pre-exponential constant
F	Diffusion flux [mol/m^2/s]
G	Irradiance incident on plane of module [W/m^2]
k	Rate of reaction [/s]
l	Thickness [m]
M	Mass [kg]
N	Number of cycles to failure
n	Reaction order
P	Permeability coefficient [kg/m/s]
P	Power [W]
P	Precipitation [cm]
R	Resistivity [Ω]
RH	Relative humidity [%]
S	Solubility coefficient [kg/m^3]
S_0	Pre-exponential constant
S_c	Share of channels in material [%]
T	Temperature [K, $^\circ$C]
T_g	Glass transition temperature [K]
t	Thickness [m]
t	Time [s, h, d]
Z	Impedance [Ω]

Constants

k_B	Boltzmann constant
R	Universal gas constant

List of Figures

List of Tables

1 Introduction

As the global energy demand continues to grow over the 21st century, it is imperative that the energy supply decarbonises and becomes more efficient. To realise this transition, photovoltaic (PV) energy plays an essential role; it is the world's most abundant form of energy and can help mitigate issues surrounding climate change and energy security [1]. The growth in PV over the last two decades has been immense, primarily due to technological improvements resulting in cost reductions and government policies, and this growth is expected to continue in the coming decades [2].

Since 2010, the weighted-average levelised cost of electricity (LCOE) for PV technologies has decreased by 89%, from 0.455 USD/kWh in 2010 to 0.049 USD/kWh in 2022; the reduction means the cost has been comparable with fossil fuels since 2014, making it a strong contender in the global electricity mix [3]. To further reduce the LCOE, the operating life and efficiency of PV modules can be improved [4]. While there are recent advancements and trends in different types of PV technologies [5], crystalline silicon (c-Si) solar cells are the preferred PV technology on the market due to their long-term durability and reliability [6]. As the efficiency of c-Si modules is intrinsically limited 29% [7] and researchers continue to move advances towards this limit, analysis into failure and degradation modes has increased in the last two decades to understand the causes of shortened operating lifetime.

As installed PV capacity continues to grow in the coming decades, PV waste is expected to rise to around 78 million tonnes by 2050 [8]. It is therefore imperative, not only that recycling solutions are found, that PV modules fulfil their expected operational lifetime and do not reach their end of life prematurely. Discerning how modules degrade can lead to finding preventative measures to prolong operational lifetime and make best use of the valuable materials.

This chapter presents an overview of the causes and modes of PV module degradation. Section 1.1 outlines the components of PV module, focussing on encapsulant and backsheet materials. In section 1.2, the leading causes (stress factors) of PV module degradation are discussed, and how they degrade (degradation modes) are describe in section 1.3. Different approaches to modelling degradation are considered in section 1.4. The research gap is summarised in section 1.5. Finally, the objective of this thesis is stated in section 1.6, outlining the research questions and scope.

1.1. Solar energy and module characteristics

A solar cell is a device that converts sunlight into electrical power via photovoltaic phenomena. A PV system primarily consists of solar modules, inverters, and charge controllers, where different materials are used to obtain desired efficiencies or costs [9]. Figure 1.1 depicts the general setup of c-Si PV module. The aluminium frame holds all the components together and protects against external elements. The glass is used as a module front cover, typically low-iron soda-lime float glass because of its high transparency, robustness, low cost, and impermeability to gas and moisture [10]. The polymer backsheet covers the back of the PV module, protecting it from the external environment. Backsheets typically comprise three primary layers: weathering weathering-resistant outer layer, an electrically in-

sulating core layer, and adhesion promoting inner layer [11]. The choice of backsheet is independent of the chosen encapsulant material [12]. The most commonly used backsheet material is polyethylene terephthalate (PET) due to its good cost-performance ratio [13]. The junction box, typically connected on the backside of the PV module rather than the edge, protects the module connection, external wiring, and bypass diodes [10].

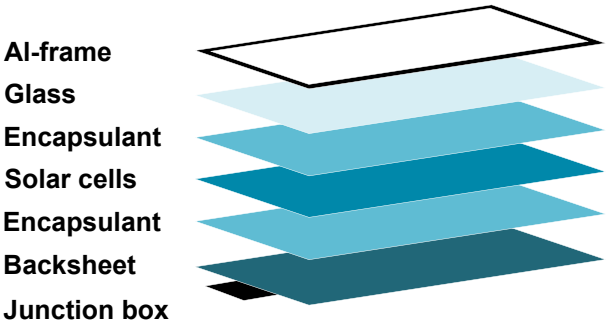

Figure 1.1: Composition of a standard PV module.

Solar cells
Solar cells consist of semiconductor materials; the PV market is dominated by wafer-based silicon solar cells, due to the material's favourable properties and abundance [14]. However, thin-film technologies, including amorphous silicon (a-Si), cadmium telluride (CdTe), copper indium gallium selenide (CIGS), have shown potential for competition, as well as gallium arsenide (GaAs), and perovskites [15].

Encapsulant materials
The encapsulant is a vital layer in PV modules, providing structural support, optical coupling, electrical isolation, and protection from external factors [16]. In their early development, PV modules used encapsulants based on polydimethyl siloxane (PDMS) because of its exceptional stability against ultraviolet (UV) light and thermal stresses [17]. However, since the 1980s, ethylene-vinyl acetate (EVA) has dominated the industry due to its low cost and high thermal stability [18]. The polymer is typically designed to form chemical cross-links to limit material flow to situations where mechanical stresses are sufficient to break chemical bonds. Furthermore, the presence of chemical cross-links enhances the efficiency of primers in facilitating adhesion at surface interfaces. This enables a cross-linked system to bond to surfaces chemically, ensuring proper adhesion with the backsheet and glass. About 1 to 2 wt% of EVA film comprises of a thermally activated peroxide, utilised for cross-linking at elevated temperatures in the lamination process [19]. Besides the peroxide curing agent, additional chemicals, such as stabilisers and additives, are integrated into the EVA encapsulant [20]. However, numerous studies report that PV module performance reduces due to the degradation of the EVA [21]. Producing acetic acid during oxidation is a major drawback of EVA [22]. The acid can lead to corrosion of metal components in the module and loss of adhesion, which in turn can lead to delamination of the encapsulant [18, 23].

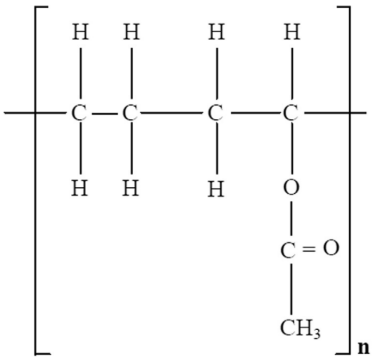

Figure 1.2: Chemical structure of EVA [24].

Other encapsulant materials, such as silicone, ionomer, polyvinyl butyral (PVB), and thermoplastic polyurethane (TPU), are alternatives to EVA. Still, they present concerns over cost or long-term stability [25]. Polyolefin encapsulant materials have emerged as promising alternatives to EVA because of their low price and high encapsulant efficiency [26]; among them are thermoplastic polyolefin (TPO) and polyolefin elastomer (POE). The main advantage of these materials is that acetic acid cannot be formed [27]. Additionally, TPO encapsulants do not require chemical cross-linking due to their higher melting temperature, which provides stability to the module. This has two key benefits: (i) all products required for cross-linking are no longer needed, and (ii) the lamination cycle time can be greatly reduced as the curing time is removed [21]. Like TPO, POE's main chain is polyethylene, but it has a different side group. POE has a high transmittance, forms strong bonds, and has high ageing resistance [26]. However, POE films contain cross-linking agents, so the lamination process is similar to that of EVA [27].

Backsheet materials
The backsheet is critical to protecting the module from harsh environments and ensuring the long-term reliability of PV modules [28]. It primarily protects the environment and acts as a moisture barrier. Backsheets typically have a multilayer structure, allowing the tailoring of optical, thermo-mechanical, electrical, and barrier properties [29]. Multilayer backsheets are typically made up of three main layers: a weather-resistant outer layer, an electrically insulating inner core layer, and an adhesion promoting cell side layer [11]. The layers are mostly comprised of polymers, such as polyethylene terephthalate (PET), polyamide (PA), polypropylene (PP), polyvinyl fluoride (PVF), and polyvinylidene fluoride (PVDF). PET is the most commonly used backsheet due to its good cost-performance ratio [13]. However, the lower costs may come with reduced weather ability and lifetime [11]. Specifically, PET is known to be degraded by hydrolysis from water vapour [30].

1.2. Stress factors

Throughout operation, PV modules are exposed to stress factors influencing their power performance and long-term reliability. These factors can be external climatic stressors or stressors in the module. Different stressors degrade modules in different ways, depending on the conditions and properties.

Moisture
Moisture can be present in the environment in the form of water vapour (humidity), condensation, rain, snow, and ice. The amount of moisture in the environment depends on the climate; in hot and humid climates, the corrosion, delamination, and discolouration of encapsulants have been observed in older field PV modules as a result of moisture and gaseous ingress modules [31, 32]. Moisture can enter the module through the edges, backsheet, and through cracks and voids [33]. The ingress of this moisture in modules through the packaging materials can degrade components. Specifically, it can weaken adhesive bonds at module component interfaces, which results in delamination. In larger quantities, moisture ingress can lead to mechanical stresses because of the hydro-dynamic volume changes [10]. In combination with temperature and UV radiation, moisture in the EVA layer can produce acetic acid through hydrolysis reactions, leading to corrosion, delamination, and discolouration [12, 34, 35].

Moisture ingress in a PV module is a diffusion phenomenon, usually described by Fickian's 2nd law of diffusion:

$$\frac{\partial C}{\partial t} = \nabla \cdot (D \nabla C), \tag{1.1}$$

where C is the concentration of the permeant and D is the experimentally determined diffusion coefficient [36]. For 1-dimensional diffusion, Equation 1.1 is the differential equation of the rate of flow of permeant per unit area, known as diffusion flux (F), and is given by

$$F = -D \cdot \frac{\partial C}{\partial x}, \tag{1.2}$$

where x is the space coordinate measured normal to the section and $-\partial C/\partial x$ is the driving force for the diffusion [12]. The rate of moisture ingress in a module can be experimentally measured by the water vapour transmission rate (WVTR). The material's WVRT could be taken as the value of F, as measured experimentally. Encapsulants with high WVTR see more corrosion of the solder bonds [25].

The WVTR is given by the following equation:

$$WVTR(t) = \frac{DC_s}{l}\left[1 + 2\sum_{n=1}^{\infty}(-1)^n \exp\left(-\frac{Dn^2\pi^2 t}{l^2}\right)\right], \tag{1.3}$$

where C_s is the saturation concentration and l is the membrane thickness [37].

UV radiation
One of the critical stress factors affecting module performance is UV radiation [24]. Modules are exposed to incident solar irradiance, covering a wavelength range of 280 - 4000 nm. However, the photons in the UV region (280 - 400 nm), despite only corresponding to 4.6% of the solar energy, are the most harmful to the encapsulant material [10]. UV radiation is further classified into three ranges: UVA (315 - 400 nm), UVB (280 - 315 nm), and UVC (280 - 100 nm), of which UVB is the most harmful for polymer materials [24]. The amount of photodegradation depends on the geographical location; places that receive higher solar irradiance receive more UV irradiance [34].

The degradation of EVA encapsulant causes a yellow or brown discolouration; this change in colour results in optical transmission losses, which decreases the module's power output [9]. It is reported that the main degradation reactions for EVA are Norrish I and Norrish II, which produce acetaldehyde and acetic acid, respectively [18, 38]. These reactions can be seen in Figure 1.3. These degradation products catalyse the degradation of EVA, causing corrosion to the metal [18]. The energy of the photons in UV radiation is great enough to break the C-C and C-O bonds in EVA, as seen in Figure 1.2 [10].

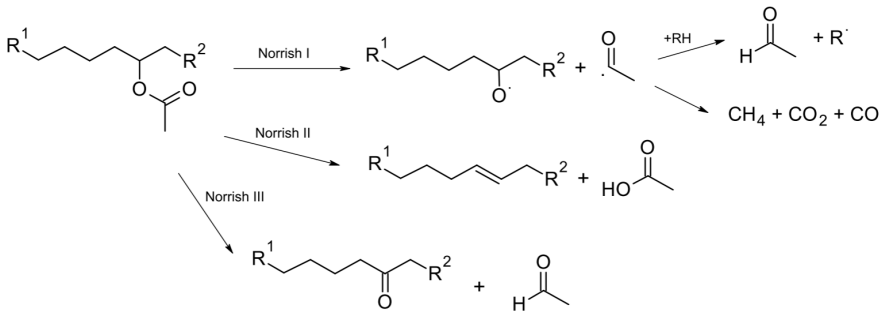

Figure 1.3: UV induced degradation mechanisms (Norrish I-III) [39].

Temperature
The ambient temperature and temperature of the module are both key stress factors influencing the system's performance. These two temperatures typically differ because of incident irradiance and additional factors, such as wind speed, module configuration, and the thermal conductivity of the materials. Consequently, permeation and reaction rates of materials may accelerate, and cause mechanical stress, which can affect the module's performance [10].

The Arrhenius equation is the most common model of temperature dependence; it models the temperature effect on the rate of chemical reactions as [40, 41]:

$$k = A \cdot \exp\left(-\frac{E_a}{k_B \cdot T}\right), \tag{1.4}$$

where A is the rate constant, E_a is the activation energy (the minimum amount of energy needed for a specific reaction to occur), k_B is the Boltzmann constant, and T is the ambient temperature. The Arrhenius relationship approximates the behaviour of a complicated chemical process over a range of temperatures with the assumption that there is a step that is rate-limiting [42]. While the equation is applicable in numerous scenarios, there are some instances where it is not appropriate, such as for modelling the encapsulant discolouration because it does not consider UV intensity [40].

High voltage
In a PV system, modules are usually connected in series to reduce the loss caused by high currents and the module frames are grounded for safety reasons. The electrical potential difference between the cells and the frame at either end of a module string may be increased, depending on the type of inverter employed in the system. This difference induces leakage currents, flowing from the frame to the cells and results in potential difference degradation. This can be particularly concerning as the voltage of a PV system is usually maximised to reduce overall costs [43].

Soiling
Soiling is a form of shading; it describes the accumulation of dust, air pollution, bird droppings, and other particulates on PV modules [44]. Unlike the aforementioned stress factors, soiling does not affect the long-term reliability of PV modules. Still, it can decrease the module's power output as it can reduce the amount of sunlight reaching the cells [10].

Chemicals
Chemicals, both natural and industrial, can cause corrosion in PV modules. The most common depends on the area: salt mist in offshore areas, ammonia in agricultural areas, and sulphuric and nitric acid in industrial areas. These chemicals can degrade PV components, resulting in performance degradation and potentially causing safety issues [10].

1.3. Degradation modes

Solar panels degrade in various ways over their lifetime, decreasing their power output and their operational lifetime. Typically, a 20% decline in power output is considered the point at which the module has reached failure [24, 45]. However, there is no unanimous agreement on the definition of failure, as a high-efficiency module degraded by 50% may still exhibit greater efficiency than a non-degraded module of a less efficient technology [24]. Identifying the underlying degradation mechanism through experiments and modelling can directly contribute to improvements over the module's entire operational life [45].

Discolouration
Discolouration is one of the most common degradation modes in solar panels [44, 46]. Ideally, the encapsulant of a PV module should be transparent, enabling maximum light penetration to reach the underlying solar cell. However, exposure to stress factors, such as UV light and moisture, degrades the EVA over long-term field operation [47]. A by-product of this degradation is chromophores, which cause strong absorption in the UV spectral region, turning the encapsulant yellow, then brown on the module surface [48]. This discolouration reduces the transmittance of light reaching the cells, decreasing the photocurrent of the module and power generated [9, 24]. When subjected to prolonged exposure to external stressors, strong discolouration can lead to delamination, embrittlement, and mechanical failure [48]. It has been reported that the transmittance reduced can result in a power production loss of up to 0.5% [45], and even up to 1% per year in subtropical climates [49].

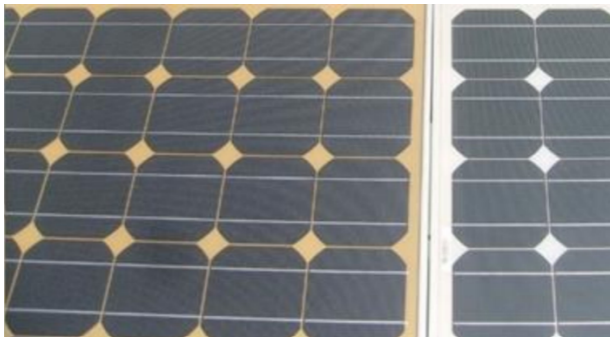

Figure 1.4: A PV module with discolouration on the left [28].

Corrosion
A PV module's materials deteriorate over time due to chemical, electrochemical, and physical reactions with the surroundings, resulting in corrosion [12]. Electrochemical corrosion can occur in the presence of oxygen, moisture, temperature fluctuations, and corrosive substances [50]. The moisture and oxygen are retained by the module's frame, initiating the corrosion process. This corrosion attacks the metallic connections of the cells, resulting in performance loss due to increased leakage currents. Additionally, the adhesion between the cells and the metallic frame degrades, and subsequently, there is water diffusion in the encapsulant [51]. Furthermore, the acetic acid produced from EVA due to environmental stressors corrodes the metal grid and other components [36]. The formation of corrosion by-products can disrupt the current flow, which reduces conversion efficiency [52]. Corrosion can also affect the module's optical properties, reducing light absorption; the transparent conductive oxide (TCO) layers can be prone to corrosion, changing their transparency and conductivity [53]. Various corrosion mitigation strategies are being explored, such as the use of protective coatings to insulate from environmental stressors, and the use of corrosion-resistant materials and optimised designs [52].

Breakages and cracks
The glass used in PV modules is processed to increase its strength. Despite this, breakage is the most common failure mode [10]. Glass breakage usually occurs during transportation, installation, and maintenance of PV modules [54]. It may also occur during operation because of thermal or mechanical stresses, such as from static or dynamic loads and hotspots [10]. This failure mode is less severe in c-Si modules as the other elements are still intact, but it is a bigger concern in thin-film modules because of the delicate configuration. Backsheet cracking is an increasingly frequent problem. Modules with cracks are reported to have insignificant power degradation, but the damage does increase the risk of electrical shock [51]. It further exposes the module to environmental stress, resulting in aforementioned degradation modes [55].

Delamination
Delamination is the adhesion loss between the encapsulant layer and the cells, or between cells and the front glass. This deterioration could be due to inadequate lamination process, vacuum pressure, the presence of contamination, the absence of adhesion-promoting additives, or it could be due to climate degradation of module components [18, 35, 56, 57, 58]. Significant issues can arise as it causes two effects: (i) it can increase light reflection, and (ii) it can increase water penetration inside the module [59]. The most severe degradation occurs at the module's edges, posing a threat to power efficiency and introducing electrical risks to both the module and the entire installation [51]. Figure 1.5 shows a severe scenario in which the back half of the encapsulant has separated from the glass. In less severe cases, delamination typically leads to the lightening of an area [46].

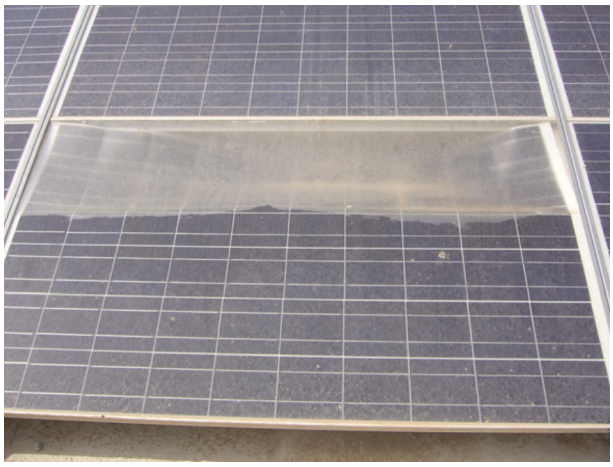

Figure 1.5: A PV module with extreme delamination where the back half of the encapsulant has separated from the glass [59].

Hot spots
A hot spot is an area of the module experiencing a very high temperature; this elevated temperature can damage the cell or any other element of the module, reducing the module's power performance and accelerating cell degradation [59]. The cause of the hot spot could be due to various cell failures, including cell mismatch, partial shadowing, or issues in the interconnection between cells [60]. Nowadays, bypass diodes are used to relieve hot spotting, but this equipment does not prevent hot spotting, nor does it fix the damage it causes [61].

Bubbles
Similar to delamination, adherence loss can occur in small areas to form bubbles. They usually occur due to a chemical reaction in which gases are produced. The defect suppresses heat dissipation, causing cells to overheat and reduce cell lifetime [59, 62]. However, bubbles were not found to significantly the performance of modules [62].

Potential-induced degradation (PID)
Potential-induced degradation (PID) describes the degradation of PV modules after being exposed to voltage stress [63]. In a PV system, the modules are usually connected in series to increase the system's voltage, which gives a lower loss of yield and produces an efficient power transmission. Therefore, the system potential difference can reach a very high voltage [64]. At high voltages, particularly in humid conditions, leakage currents enable the migration of species within modules, resulting in PID, which can dramatically reduce power production [65]. The process sees the negative ions move away from the solar cells and positive ions move from the glass and other packaging materials towards the cells [48]. This attracts sodium (Na) to the cell's surface, which results in delamination due to the weakening of the adhesion bonds of the EVA and the cell [66]. The materials used in the module and its environment are critical to PID degradation. A study by Singh et al. reported that PID could reduce a module's power output by 20-80% [67].

Light-induced degradation (LID)
Light-induced degradation (LID) describes the decline in cell efficiency observed during excess carrier injection through above-bandgap illumination and forward biasing [68, 69]. In this degradation process, the short-circuit current and the open-circuit voltage of the silicon cell decreases, resulting from increased minority-carrier recombination in the bulk of c-Si [70]. It is well understood that LID strongly affects c-Si cells made on Czochralski wafers, arising from boron-oxygen defects in the wafer [71]. It is reported that the cells could lose 3-4% of output power as a result of LID [50].

1.4. Modelling of degradation

Degradation models are used to predict solar modules' failure times. To model degradation modes, an understanding of external and internal parameters is required. Models are typically either statistical or analytical; integrating both models can improve the understanding of functions within PV systems [72].

1.4.1. Statistical models

Statistical models are employed to estimate degradation rates based on real data to identify performance trends. A time series can be decomposed into several elements: the *trend* is long-term movement in the mean; the *seasonality* is the cyclical fluctuation related to the calendar; and the *residuals* are other random or systematic fluctuations [73]. While these models can be useful for data extrapolation and predictions, they do not consider additional factors that affect performance. Hence, discussing a performance loss rate (PLR) is more precise than referring to a degradation rate [72].

Simple linear regression
Simple linear regression (SLR) is frequently used due to its straightforward approach, which aims to evaluate the impact of a variable on the outcome [74, 75]. The algorithm used the method of least squares to fit a linear trend. However, the method puts more weight on outliers, so it can result in large uncertainties [72].

Classical Seasonal Decomposition
Classical seasonal decomposition (CSD) is an analysis technique that separates the seasonality and error of the time-series data to give a trend. An additive or multiplicative model may be used, depending on the stability of the seasonality [72].

Autoregressive integrated moving average
The autoregressive integrated moving average (ARIMA) model combines autoregression, differencing, and moving averages to analyse and predict time-dependent data points [72]. It can be used to model many time series [73].

Seasonal-trend decomposition using LOESS
LOESS is a method used to estimate non-linear relationships. Seasonal-trend decomposition using LOESS (STL) is similar to CSD; it decomposes a time series into a trend, seasonality, and residuals [76]. Compared to CSD, it is less affected by outliers and missing data, and is a more robust model [72].

1.4.2. Analytical models

The following analytical models use physical and chemical theories of a particular degradation mode. While they are based on understood processes, they still lack the influence of some parameters.

Models for corrosion
Several models have been developed with the key assumption that the degradation rate is proportional to the amount of water in PV models, and there is a temperature dependence [72]. Peck's model, Equation 1.5, evaluates degradation due to relative humidity (RH) and module temperature:

$$k_{\text{Peck}} = A_H \cdot \exp\left(-\frac{E_a}{k_B \cdot T_m}\right) \cdot RH^n, \tag{1.5}$$

where $R_{D,\text{Peck}}$ is the rate constant, A_H is the pre-exponential constant, E_a is the activation energy of the degradation process (eV), k_B is the Boltzmann constant (8.62×10^{-5}), T_m is the module temperature (Kelvin), n_{RH} is the exponential constant based on module characteristics, and $RH(\%)$ is the effective module relative humidity (RH) proposed by Koehl et al. [77]. (The relative humidity is defined as the raio of the mass of water vapour in a unit volume compared to the mass of water vapour which that volume could hold if the vapour were saturated at the mixture temperature [78].)

Other models also determine the degradation rate based on RH, namely the Eyring model:

$$k_{\text{Eyring}} = A_H \cdot \exp\left(-\frac{E_a}{k_B \cdot T_m} - \frac{b}{RH}\right), \tag{1.6}$$

and the exponential model:

$$k_{\text{Exp}} = A_H \cdot \exp\left(-\frac{E_a}{k_B \cdot T_m}\right) \cdot \exp(m \times RH), \tag{1.7}$$

where b and m are model parameters. Peck's model is most commonly used because it shows the best performance in experimental calibration [79]. The models have several limitations; the greatest is using the relative humidity of the environment as a key input. Moisture ingress is a key stress factor leading to degradation, and the amount of moisture in the module is not the same as the humidity of the environment because the module has been designed to protect its components from such climatic stressors.

Model for UV degradation
To model the degradation of polymer materials due to UV radiation, the temperature of the module and the RH must also be considered. Therefore, Braisaz et al. [80] proposed modifying Peck's model, and using the Arrhenius model for the temperature stress, resulting in the following equation:

$$k_P = A_P \cdot \exp\left(-\frac{E_P}{k_B \cdot T_m}\right) \cdot (1 + RH^n) \cdot UV^X, \tag{1.8}$$

where A_P is the pre-exponential constant, E_P is the activation energy for power degradation due to photoreactions, UV is the integral UV dose (kW/m^2), and X is the model parameter indicating the impact of UV dose on degradation [79]. The factor that is most affected by UV stress is the short-circuit current (I_{sc}), so k_P is the degradation rate of I_{sc} [72]. Therefore, this model assumes that the degradation rate of I_{sc} is proportional to the UV dose.

Model for thermomechanical stress
Thermomechanical stress arises from temperature cycles; to model thermal cycling (TC), the Coffin-Manson relationship is often used:

$$N = \frac{1}{(\Delta T)^{\alpha}}, \tag{1.9}$$

where N is the number of cycles to failure, ΔT is the cyclic temperature (Kelvin), and α is a constant based on material characteristics [81]. According to Escobar and Meeker, the impact of temperature cycling may depend significantly on the maximum temperature, T_U [42]. The distribution of cycles-to-failure in temperature cycling may also depend on the cycling rate, for instance, due to heat build-up. To include this effect, Kaaya et al. modified the Coffin-Manson relationship to give the following:

$$k_{Tm} = A_{Tm} \cdot (\Delta T)^{\theta} \cdot C_N \cdot \exp\left(-\frac{E_{Tm}}{k_B \cdot T_U}\right), \tag{1.10}$$

where C_N is the cycling rate, T_U and T_L are the module's upper and lower temperature limits (Kelvin), $\Delta T = (T_U - T_L)$, and E_{Tm} is the activation energy of power degradation (eV).

Model for potential-induced degradation
To model PID, the contribution of each stress factor to the degradation mode has to be considered; high temperatures, high relative humidity, and voltage contribute to the degradation [82]. Annigoni et al. proposed the following relation to describe the power degradation as a function of PID, using an equation previously proposed by Hacke et al. [82, 83]:

$$\frac{P_{max}(t)}{P_{max}(0)} = 1 - A \cdot \exp\left(\frac{-E_a}{k_B \cdot T}\right) \cdot RH^n \cdot t^2 \cdot V, \tag{1.11}$$

where $P(t)$ is the module's measured power after exposure to stress for t hours, $P(0)$ is the initial power, and V is the voltage.

Model for combined stress
Given numerous degradation modes will contribute to the demise of the module's performance, it is also important to combine individual models to give a combined stress model. A combined model was proposed by Kaaya et al. which considers the effects of RH, UV degradation, and thermomechanical stress [79]:

$$\begin{aligned} k_T &= A_N \cdot (1 + k_h)(1 + k_p)(1 + k_{Tm}) - 1 \\ &= A_N \cdot \prod_{i=1}^{n} (1 + k_i) - 1, \end{aligned} \tag{1.12}$$

where k_T is the total degradation rate (%/year), k_i is the ith rate constant, and n is the total number of degradation processes. A_N is the normalisation constant (year^{-2}/%).
Additionally, Subramaniyan et al. suggested an alternative method, shaped by the Norris-Landzberg approach [81, 84]:

$$k_C = A_C \cdot (\Delta T)^{\alpha} \cdot UV^{\beta} \cdot RH^{\gamma} \cdot \exp\left(-\frac{E_a}{k_B \cdot T_{max}}\right), \tag{1.13}$$

where k_C is the reaction rate due to climatic stressors such as module temperature, cyclic module temperature, UV radiation, and RH. ΔT is the daily cyclic temperature of the module (Kelvin), UV is the daily daytime average UV irradiance (W/m^2), and RH is the daily average RH (%). The parameters to be estimated are A_C, which is the frequency factor (sec^{-1}), E_a, the activation energy (eV), α, which is the effect of cyclic temperature, β, the effect of UV radiation, and γ, the effect of RH.

1.5. Research gap

The degradation of PV modules is an increasingly researched area in the field of photovoltaics. However, while stress factors for PV modules are well known, but the mechanisms behind them are still being understood [28, 46, 85]. Most degradation models consider the combination of stress factors (typically module temperature, UV irradiance and relative humidity), while few consider the stress factors individually, with further research required and additional ageing factors to be employed [79]. Analytical models are more commonly used than statistical ones, which use fundamental physics to build the model but they can lack detail; calibration of these models relies on experimental data, possessing a challenge when no data is available [77, 79, 82]. Furthermore, the modelling of degradation is usually assumed to be linear, but reports indicate that degradation is nonlinear. The investigation into nonlinear degradation is still in its preliminary phase [86, 87].

The stress factors described in section 1.2 are being explored, mostly qualitatively rather than quantitatively. The number of publications on moisture-induced degradation (MID) in PV modules has seen a sharp increase in publications in the last 15 years, indicating increased interest [12]. Since relative humidity influences moisture penetration within the module, which influences delamination and corrosion, relative humidity can be considered an “indirect” stress factor, compared to temperature and UV irradiance. Understanding the relation between RH and moisture ingress is therefore of high importance. It has widely been reported that MID occurs more in tropical (hot and humid) climates, and less in polar (cold and dry) climates [34, 40, 46, 88]. Investigation into MID for different types of solar cells has begun [89, 90, 91, 92, 93], but MID for different types of encapsulants and backsheets is largely unexplored. Furthermore, the modelling of the ingress of moisture into a PV module has been started by Daniel Jimenez Pelarda, as well as power degradation caused by moisture ingress [94]. These models have laid the foundation for modelling MID but the model’s ability to accurately represent reality may be constrained by some assumptions, including how moisture permeates materials and how the composition of materials changes in the presence of water.

1.6. Thesis objective

The objective of this thesis is to investigate moisture ingress in PV modules, specifically studying **improving the accuracy of the simulations by investigating alternative means of modelling moisture diffusion**. In order to achieve this, the following research goals have been formulated:

1. **Optimise the existing moisture ingress model to reduce computational time.** A model was previously developed in COMSOL by Daniel Jimenez Pelarda to simulate moisture ingress in PV modules; the accuracy of the model’s results will be verified and the computational time will be reduced.
2. **Investigate potential model improvements.** There is some deviation between the simulation and experimental results; adaptations to the model are proposed to better simulate realistic-operation.
3. **Consider the effect of these improvements in various PV materials and climates.** While EVA and PET dominate the market, other materials have favourable properties and modules are installed in vastly different climates, strongly affecting moisture ingress.
4. **Design an experiment to measure moisture ingress in PV samples.** There is insufficient data to which the simulation results can be compared; experimental data can support or contradict the simulation findings.

1.7. Thesis outline

The thesis begins with a review of the existing moisture ingress model in chapter 2, after which the model is optimised to ensure it delivers accurate results and adapted to reduce the computational time of the simulations. Chapter 3 explores non-Fickian diffusion, using a dual transport method to simulate it, and proposes a means of simulating material degradation. The findings in this chapter are then applied to other PV materials and various climates in chapter 4. An experimental method to measure moisture ingress in PV samples under is detailed in chapter 5. Finally, in chapter 6, the conclusions from the thesis are summarised, and ideas for future work are outlined.

2

Development of the moisture ingress model

Simulating moisture ingress in PV modules is valuable for understanding degradation rates in different climates, and can further be used to understand its effect on PV performance. This chapter reviews the existing moisture ingress model and possible improvements. In section 2.1, the theory of moisture diffusion is discussed. Then, section 2.2 addresses the model configuration, assumptions, and validation of the model. Section 2.3 reports the convergence test run to ensure the model delivers satisfactory results, and the model is adapted to reduce its computational time. Finally, section 2.4 discusses the limitations of the model and the optimisation process.

2.1. Moisture transport

Moisture ingress describes the diffusion of water molecules and other gaseous species (e.g. oxygen, nitrogen, carbon dioxide, etc.) into a PV module [12]. When gaseous or water molecules are adsorbed onto an encapsulant's surface, they begin to diffuse when they pass through and desorb onto other PV module components at the proper concentration gradient. Moisture diffusion is usually described using Fick's law, given in Equation 1.1, and it assumes the diffusion coefficient is independent of concentration.

Diffusion

The diffusion coefficient expresses the rate at which water vapour diffuses through a material [95]. A two-step process comprising the absorption of water vapour into the encapsulant and the diffusion of the water vapour, until equilibrium is reached, describes the diffusion of moisture through polymer materials [96]. In Fickian diffusion, the diffusion coefficient is concentration-independent and strongly influenced by temperature, T. In a homogeneous material, it can be accurately described by the Arrhenius equation as [12]:

$$D = D_0 \exp\left(\frac{-E_{a,D}}{R \cdot T}\right), \tag{2.1}$$

where D_0 is the pre-exponential constant, $E_{a,D}$ is the activation energy for diffusion to occur, and R is the universal gas constant (8.314 J/mol·K). This relation features two assumptions: (1) water diffusion has no influence on the physical properties of polymers; (2) the activation energy of a diffusion process is temperature-independent [97]. Diffusivity measurements for EVA and PET are in good agreement that diffusivity increases with increasing temperature [31, 98, 99], and it has been shown that diffusion is more sensitive to temperature changes than other environmental stressors [12].

Solubility

While diffusion considers the rate of the process, the solubility coefficient indicates how much water can be dissolved. Diffusion is driven by the concentration gradient, which is determined by the amount of

dissolved water vapour in the encapsulant. Similar to the diffusivity coefficient, the solubility coefficient can be described by the Arrhenius equation as [12]:

$$S = S_0 \exp\left(\frac{-E_{a,S}}{R \cdot T}\right), \tag{2.2}$$

where S_0 is the pre-exponential constant and $E_{a,S}$ is the activation energy for solubility.

The permeability, P, of a material that obeys Fickian behaviour is defined as the product of the diffusivity and solubility [100]:

$$P = D \cdot S. \tag{2.3}$$

The permeability of a material represents the amount of permeating water through a polymer material [31]. It is found that the solubility and permeability of encapsulant materials significantly increases with increasing temperature [95, 101, 102]. These transport properties are typically determined using water vapour transmission rate (WVTR) experiments.

2.2. Current moisture ingress model

Daniel Jimenez Pelarda developed the moisture ingress model in COMSOL Multiphysics, a software package that uses finite-element analysis (FEA) to solve physics and engineering problems [94]. The theory provided in the previous section was used to build a model which simulates moisture ingress in a PV module. This section shows the module configuration and outlines Jimenez Pelarda's assumptions in the development of the model.

2.2.1. Model configuration

Moisture diffuses through the backsheet into the module. The moisture then diffuses through the module, as shown in Figure 2.1. The glass acts as an impenetrable barrier, through which moisture cannot escape. Moisture egress may occur when the concentration outside the module is less than inside, which is not depicted in the figure.

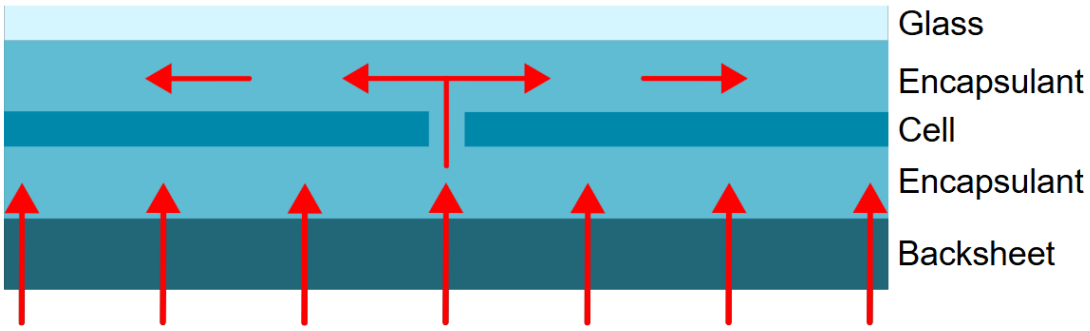

Figure 2.1: Moisture ingress in a PV module indicated by the red arrows (not to scale).

The COMSOL model considers the moisture transport and module configuration while aiming to reduce computational costs. Due to symmetry, the model only considers half of the diagram in Figure 2.1. Additionally, as the glass is impenetrable, it need not be included in the model, and instead the top of the encapsulant is a boundary. As the diffusion of moisture through the backsheet is considered to be uniform, only the area below the cell gap needs to be modelled. Furthermore, as this model does not investigate the effect of moisture on the solar cell, the cell does not need to be modelled. Thus, the model is set up as shown in Figure 2.2 (not to scale). The points A-F marked on the model are used in section 2.3.

2.2.2. Moisture ingress model

The model makes the following assumptions:

- The ambient pressure is 1 atm and remains constant.
- No reaction of water is considered.
- The interfaces are in equilibrium. Henry's law (Equation 2.6) describes the equilibrium. Henry's law states that there is a linear relationship between the concentration of two phases.
- Solar cells and glass frontsheet are taken to be impermeable layers.
- The diffusion of water in the modules is assumed to be Fickian.
- Material properties are assumed to remain the same throughout the module's life.
- The temperature of the module is calculated using the Faiman model; the temperature is homogeneous and determines the properties related to moisture ingress.
- The backsheet is treated as one homogeneous layer.

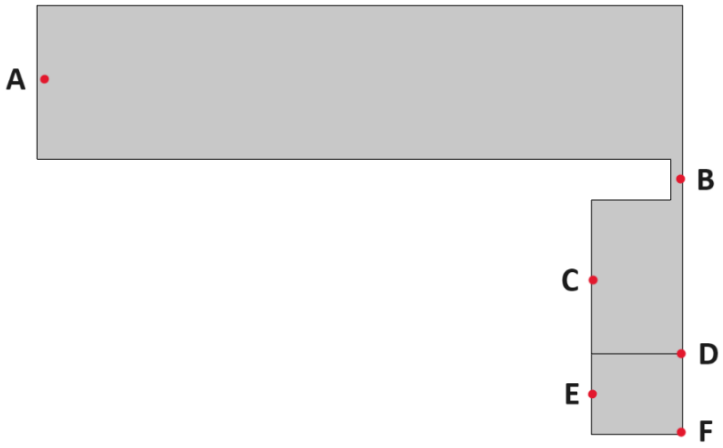

Figure 2.2: COMSOL model configuration, with A-F indicating the measurement points of interest.

Module temperature affects the performance of the module, as well as the rate of moisture ingress, so it is integral to the model. Various models have been proposed, ranging from purely empirical models, such as the Sandia model, to models based on simplified heat transfer equations. The Faiman model is a steady-state model, using a time series of solar irradiance, ambient temperature, and wind speed to calculate the module temperature [103] in the following way:

$$T_m = T_a + \frac{G}{u_0 + u_1 \cdot \nu}, \tag{2.4}$$

where T_m is the module temperature (K), T_a is the ambient temperature (K), G is the irradiance incident of the plane of the module (W/m^2), u_0 and u_1 are the constant and convective heat transfer components, respectively (W/m^{2}K, Ws/m^{3}K), to be experimentally determined, and ν is the wind speed (m/s). u_0 and u_1 have been experimentally determined and are equal to 32.6 W/m^{2}K and 3.8 Ws/m^{3}K. Compared to other models, the Faiman model delivers the most conservative results in the calculation of module energy output [104].

Additionally, vapour pressure as a function of temperature is required. The Clausius-Clapeyron relationship relates the vapour pressure of an ideal substance to temperature, but it is limited in that it is only reliable over small temperature intervals [105]. To overcome this, the Antoine equation has proved to be the most useful in determining the saturation pressure of water in the air, described as [106]:

$$log_{10}(p_{sat,H_2O}) = a - \frac{b}{T + c} = 101325 \cdot \left(4.654 - \frac{1435.264}{T - 68.848}\right), \tag{2.5}$$

where a, b, and c are constants derived from experimental data, and the pre-factor (101325) converts the equation to the appropriate units. Furthermore, understanding the concentration at the interface is essential to the model. Henry's law, adapted for this scenario, calculates concentration at the interface:

$$C_{sat} = S(T) \cdot p_{act}(T) \cdot \frac{1}{M_{\mathsf{H_2O}}} = S(T) \cdot p_{sat}(T) \cdot RH_{eff} \cdot \frac{1}{M_{\mathsf{H_2O}}}, \tag{2.6}$$

where $S(T)$ is the solubility of the material, $p_{act}(T)$ is the actual pressure of moisture in the air, $M_{\mathsf{H_2O}}$ is the molar mass of water, $p_{sat}(T)$ is the saturation pressure of moisture in the air, and RH_{eff} is the effective relative humidity.

2.2.3. Model validation

The moisture ingress model was run using parameters and conditions found in literature and validated by comparing the model's results with those in the corresponding literature. The same climate conditions had to be simulated, literature diffusion and solubility coefficients for the encapsulant and backsheet were used, and the module was sized in the same way. Numerous studies were used, so damp heat tests and real-world conditions could both be simulated and verified.

One example is the model and experiment presented by Kyranaki, who simulated and experimentally measured moisture ingress through a PET backsheet and two EVA encapsulant layers, without the presence of solar cells [107]. The model used in this thesis was adapted to simulate the same scenario, using the provided parameters, outlined in Table 2.1. The solubility of each material is not defined and the partition condition is neglected.

Table 2.1: Input parameters for the Kyranaki simulation.

Parameter	Value	Description
D_E	1.5×10^{-10} m^2/s	Diffusion coefficient of the encapsulant
D_{BS}	4.32×10^{-12} m^2/s	Diffusion coefficient of the backsheet
t_{EVA}	0.92 mm	Thickness of the EVA
t_{BS}	0.295 mm	Thickness of the backsheet
C_0	26.86 mol/m^3	Initial moisture concentration of the stacks
C_{amb-BS}	102.56 mol/m^3	Moisture concentration applied during moisture ingress
T_{amb}	323.88 K	Ambient temperature

Kyranaki reports the relative moisture content (RMC) (%) over time, which is defined as:

$$\mathsf{RMC}(\%) = \frac{C_{\mathsf{encap}}}{S_{\mathsf{encap}}}, \tag{2.7}$$

where C_{encap} is the moisture concentration in the encapsulant layer, and S_{encap} is the saturation concentration of the encapsulant. The author assumes that the digital humidity sensors used in their experiments also measure the relative moisture content of the EVA. They measure S_{encap} with Mocon moisture permeation measurement, which was conducted with PERMATRAN instrument, and find that the saturation moisture content of EVA is 2.2 kg/m^3 and T = 50° (323.15 K).

In Figure 2.3, it can be seen that the simulation results from the original moisture ingress model almost exactly matched those from Kyranaki's simulation, and it resembles the experimental results, with some deviation. Figure A.1 plots the experimental data and simulations on a semi-log graph to highlight the discrepancy in the two simulations in the first 3 hours. Additionally, the moisture concentration profiles shown in Figure 2.4 at 1h, 13h, and 88h closely resemble those reported by Kyranaki. These provide a visual representation of moisture ingress through the backsheet and encapsulant.

All preceding work has been conducted by other researchers; the work in the rest of the thesis was carried out by the author.

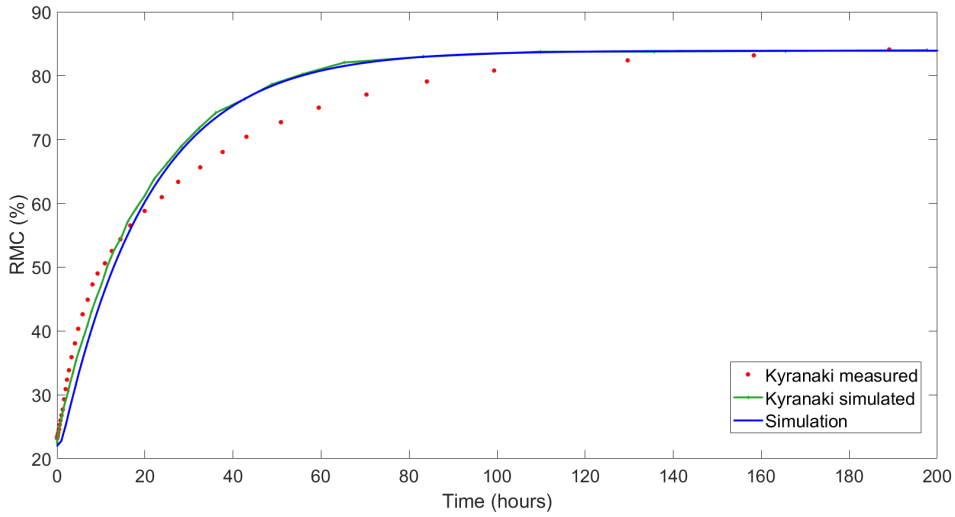

Figure 2.3: Comparison of experimental and simulated results from Kyranaki and the simulation results from the adapted model. The plot shows that the simulation results from the original moisture ingress model almost exactly matches those from Kyranaki, and they resemble the experimental data with some deviation.

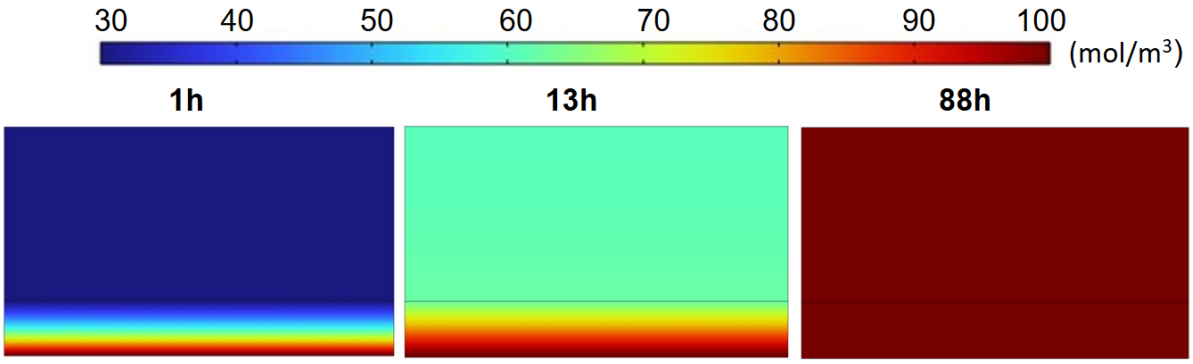

Figure 2.4: Moisture concentration profile for simulated Fickian diffusion moisture ingress at time 1 hour, 13 hours, 88 hours.

2.2.4. COMSOL mesh

COMSOL uses finite element methods to solve the partial differential equations describing moisture diffusion. This requires creating a mesh, such that the continuous problem is discretised into smaller, finite elements, and an approximate solution can be found for each element. The mesh configuration plays a critical role in the computation of the problem, how long it takes to solve it, the amount of memory required, and the accuracy of the solution. Depending on the number of solar cells involved in the model, it is extremely difficult to build an effective mesh for a photovoltaic module due to the extreme differences in dimensions [77]. Currently, the model uses a *normal* physics-controlled mesh, the default mesh, as seen in Figure 2.5. The mesh has several determining factors, such as: how the geometry is divided; with what shape or element type the geometry is divided; the size, density, and number of elements in the geometry; and the element quality [108]. A physics-controlled meshing sequence will only be based on the geometry, boundary conditions, and material properties, depending on the physics involved in the model. The approach does not incorporate numerical error estimates. The other sequence type is the user-controlled mesh, which is explored in subsection 2.3.2.

The domains in 2D meshes are represented by mesh components that are either *triangular* or *quadrilateral*. Mesh vertices are the corners of the triangle and quadrilateral elements, and mesh edges are their sides. The element size can be adjusted, ranging from *extremely coarse* to *extremely fine*.

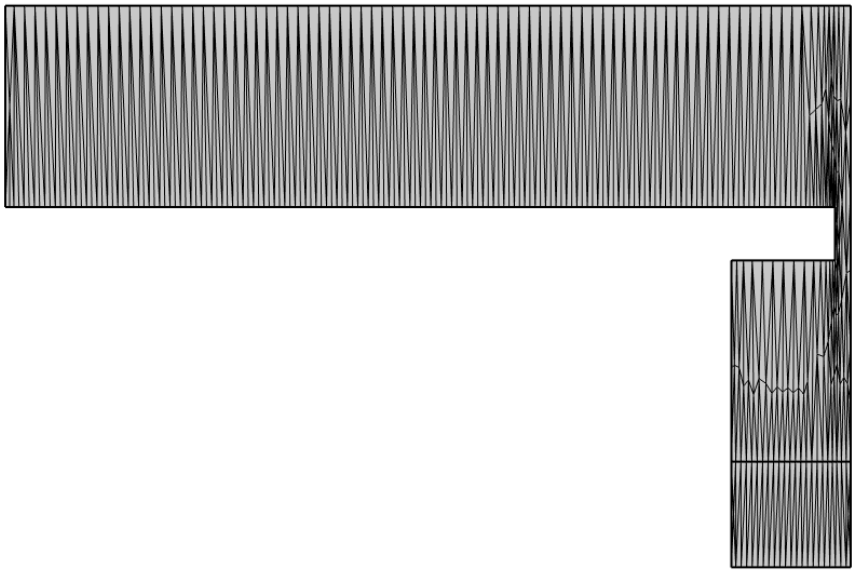

Figure 2.5: Physics-controlled mesh in the original moisture ingress model.

2.3. Model optimisation

The *normal* physics-controlled mesh has not been confirmed as the most appropriate mesh for this simulation. It is a good starting point from which a more efficient mesh can be found. A suitable mesh is found when the solution remains the same, despite using a mesh that is more coarse. Additionally, the model currently takes around 1.5-3 hours (5400-10800 seconds) to run, depending on the computational power, which can preferably be reduced by adapting the mesh. The mesh can be optimised by changing its meshing to be more dense in areas where the concentration gradient is less pronounced. This approach was used by Koehl et al. in their modelling of conditions for accelerated lifetime testing [77]. They adapted the density of the meshing to fit the non-uniformities of the components, resulting in a high mesh density in the gaps between the cells and a coarser mesh at the top of the encapsulant layer. The backsheet had a uniform mesh, except towards the module edge.

The model is run for physics-controlled meshes of various sizes in subsection 2.3.1 to confirm they deliver results in agreement. Then, in subsection 2.3.2, user-controlled meshes are explored, changing parameters to reduce the computational time of the simulation while delivering coherent results.

2.3.1. Physics-controlled mesh

First, the model was run with various physics-controlled mesh sizes: *extremely fine, finer, normal, coarser*, and *extremely coarse*. The objective was to identify for which meshes the results converge, signifying the meshes deliver suitable results. The concentration over time at the locations defined in Figure 2.2 was determined for the various meshes. The concentration profile at A and B are shown in Figure 2.6 and Figure 2.7, and the profiles at C, D, E, and F can be found in Appendix A.

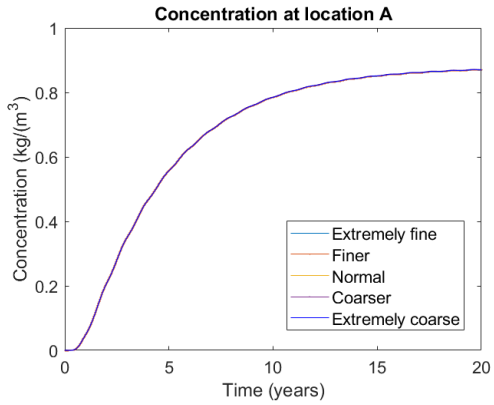

Figure 2.6: Concentration at location A for physics-controlled meshes. The simulations with each mesh deliver consistent results.

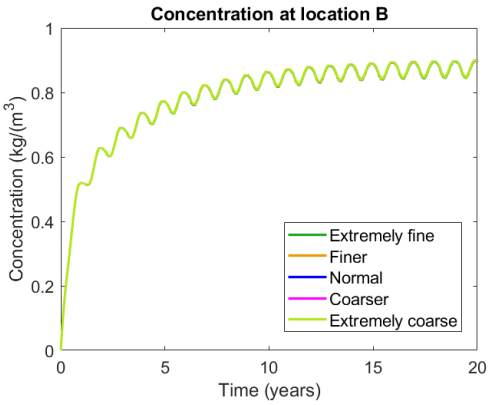

Figure 2.7: Concentration at location B for physics-controlled meshes. The simulations with each mesh deliver consistent results.

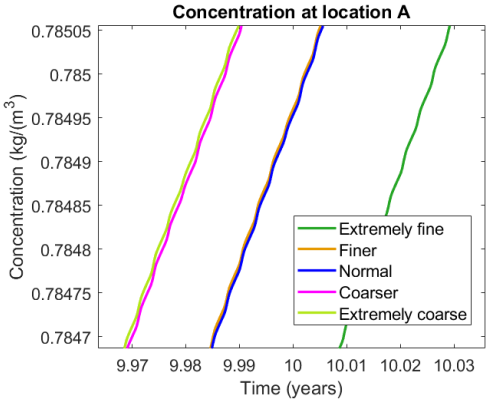

Figure 2.8: Magnified segment of concentration at location A for physics-controlled meshes. The *extremely coarse* and *coarse* simulations deliver very similar results, as do the *normal* and *finer*. The *extremely fine* simulation deviates somewhat, but is still satisfactory.

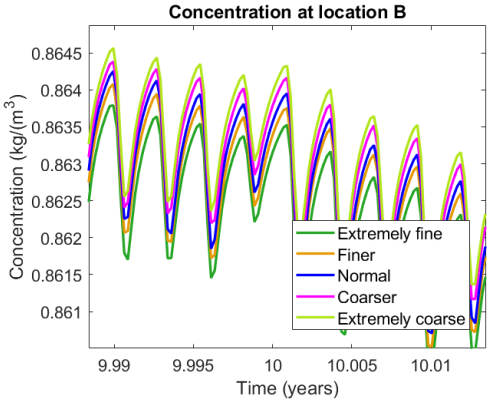

Figure 2.9: Magnified segment of concentration at location B for physics-controlled meshes. The simulation using the *extremely coarse* mesh predicts the highest moisture ingress, and the prediction decreases as the mesh becomes finer. All results are within 0.001 kg/m^3 of each other.

It can be seen that all meshes give results that follow the same trend, with similar concentration values at each time step. Figure 2.8 and Figure 2.9 zoom in on the concentration profiles at around 5000 seconds, and it can be seen that the results from the various meshes identical to three decimal places. In Figure 2.8, the *extremely coarse* and *coarser* simulations deliver very similar results, as do the *normal* and *finer*. The *extremely fine* simulation deviates somewhat, but is still satisfactory. Figure 2.9 shows that the simulation using the *extremely coarse* mesh predicts the highest moisture ingress, and the predicted concentration decreases as the mesh becomes finer. All results are within 0.001 kg/m^3 of each other.

Table 2.2 gives the approximate computational time of the simulation for each of the physics-controlled meshes. It should be noted that the values in the table can vary as they depend on the computational power of the computer on which the simulations are run and if the computation is running any other programmes. However, they indicate the relationship between the size of the mesh and the computational time, i.e. decreasing the mesh size usually increases the computational time.

Table 2.2: Computational time of various physics-controlled meshes.

Physics-controlled mesh	Computational time (s)
Extremely Fine	6235
Finer	5840
Normal	5444
Coarser	5130
Extremely Coarse	5064

From these profiles and comparing the computational run time for each mesh, it can be concluded that *normal* mesh delivers acceptable results, and the mesh can be adapted to obtain complimentary results with a shorter computational time.

2.3.2. User-controlled mesh

To further reduce the computational time, user-controlled meshes were explored. Various parameters can be adapted to control the mesh. The mesh can be set such that the problem is solved for general physics, fluid dynamics, and others; the general physics option is chosen here because the fluid dynamics option delivers an *extremely fine* mesh that would significantly increase the computational time.

- The *calibration* allows the mesh to be specified for a particular type of physics.
- The *maximum* and *minimum element size* limit the allowed element size.
- The maximum rate at which the element size can increase from a region with small elements to a region with larger elements is determined by the *maximum element growth rate*. The value needs to be either one or more than one.
- The ratio of the curvature radius to the size of the boundary elements is determined by the *curvature factor*, which also establishes the size of the boundary elements in relation to the curvature of the geometric boundary.
- The number of element layers generated in narrow regions is controlled by the *resolution of narrow regions*; a greater value results in a *finer* mesh in narrow parts.
- The shape of the domains can be set as *Free triangular* or *Free quad* to compliment the geometry of the model.
- The mesh can be modified by incorporating a *refine* node to further refine a mesh by splitting elements.

In their simulation of moisture diffusion in PV modules, Koehl et al. adapted the mesh to account for the non-uniformities of the constituent parts, resulting in a high density in the spaces between the cells [77]. A denser mesh is required around the spacing between solar cells, and a less dense mesh is needed at the top of the upper encapsulant layer. Additionally, due to the slow diffusion through the backsheet layer and the moisture egress that occurs, a coarser mesh can be used.

Through numerous iterations, an optimised mesh is proposed, which can be seen in Figure 2.10, created using the parameters outlined in Table 2.3. It was found that making the mesh too coarse can give inaccurate results, and can even increase the computational time. The increased computational time might be due to the complex geometry of the mesh (it may take more iterations to find a solution since not all the information may be captured) or due to solver convergence issues (the solver might require more iterations or fail to converge within the default number of iterations).

The quadrilateral meshes are typically more appropriate for rectangular geometries, so it could be expected that they would be more appropriate here. However, the quadrilateral meshes were found to significantly increase the computational time compared to the triangular counterpart. Furthermore, it was found that parameters sometimes limit others, e.g. the value of the minimum element size would limit the size of the maximum element size. Distributions were used in some iterations, but were later found to have limited effect as other parameters were optimised.

The final optimised mesh had a computational time of 4186 seconds, saving 23% on the computational time compared to the *normal* physics-controlled mesh that was previously used. The concentration graphs at A and B for the *normal* and *optimised* meshes are shown in Figure 2.11 and Figure 2.12. These graphs show the *optimised* mesh delivers results consistent with the results from the *normal* mesh. Zooming in, it is found that the deviation between the results at location A is approximately 0.0005 kg/m^3, and the results at location B show minimal deviation.

Table 2.3: Optimised mesh parameters.

Parameter	Value
Calibration	General physics
Maximum element size	0.3
Minimum element size	0.01
Maximum element growth rate	3
Curvature factor	0.6
Resolution of narrow regions	1
Free Triangular	-
Refine	Selection 2 and 11

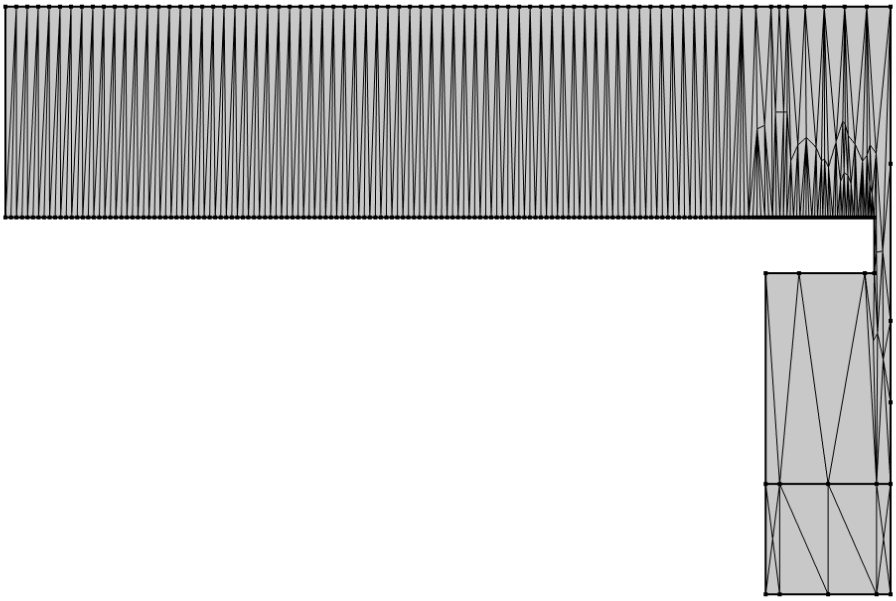

Figure 2.10: The *optimised* user-controlled mesh implemented in the moisture ingress model.

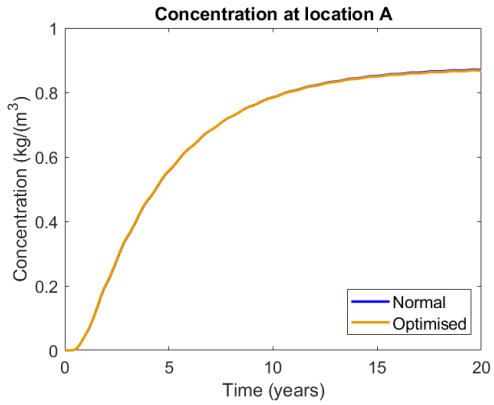

Figure 2.11: Concentration at location A for the Normal and optimised meshes. The *optimised* mesh results shows coherence with the *normal* mesh results.

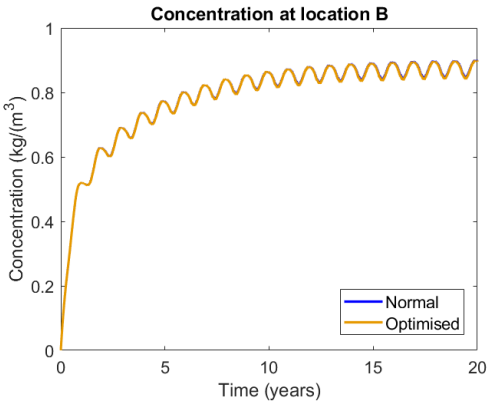

Figure 2.12: Concentration at location B for the Normal and optimised meshes. The *optimised* mesh results shows coherence with the *normal* mesh results.

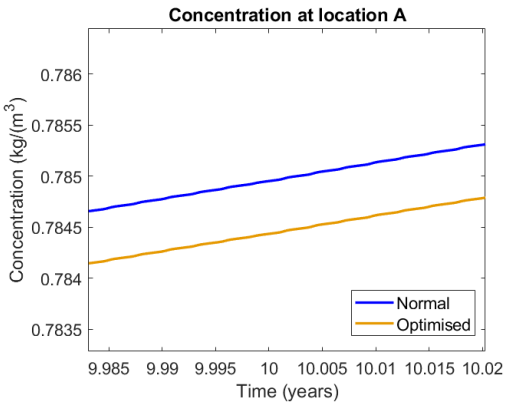

Figure 2.13: Magnified segment of concentration at location A for the Normal and optimised meshes. The deviation between the results is approximately 0.0005 kg/m^3.

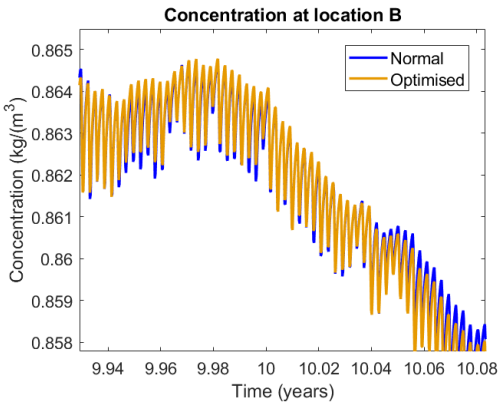

Figure 2.14: Magnified segment of concentration at location B for the Normal and optimised meshes. There is minimal deviation between the results of the simulations.

2.4. Discussion

The following discussion reflects on the soundness of the moisture ingress model and the optimisation process.

2.4.1. Limitations of the model

The moisture ingress model created by Daniel Jimenez Pelarda is based on strong assumptions and simulates moisture diffusion through PV materials well. However, some assumptions limit how well the model can reflect reality. For example, the PV material degrade over time, which is not incorporated in the model, and diffusion through the polymers may not obey Fick's law. These are explored in chapter 3.

Additionally, Equation 2.1 is an integral equation in the model, but it has some limitations. E_a is typically determined graphically and assumed to be constant; it is used to evaluate material properties at varying temperatures [12]. Linearising Equation 2.1 gives

$$\ln D = \ln D_0 - \frac{E_a}{R} \cdot \frac{1}{T}, \tag{2.8}$$

and thus D_0 and E_a can be extracted from a fitted graph of $(\ln D)$ against $(1/T)$. However, the equation assumes that temperature does not influence the activation energy of the water diffusion process, but E_a can be affected by unexpected chemical interactions due to temperature variations. Therefore, a perfectly linear relation between $(\ln D)$ against $(1/T)$, in these cases, becomes largely unrealistic [97].

This means that the determined diffusion coefficient, D, may be inaccurate and in fact change over time. A proposed alternative means of determining E_a could be using the difference in the diffusivity (D_1 and D_2) at two different temperatures (T_1 and T_2) as

$$\ln\frac{D_1}{D_2} = \frac{E_a}{R}\Big(\frac{1}{T_2} - \frac{1}{T_1}\Big), \tag{2.9}$$

but this approach relies on experimental methods and has its limitations. Moreover, the approach still finds E_a to be constant, but the theory proposes it changes as a function of temperature.

The model includes the key components of a PV module and successfully uses boundary conditions to simplify the problem, but it is not suitable for more complex simulations and investigations. For example, commercial PV modules typically use multi-layer backsheets to better protect the module from climatic stressors. This is not considered in the model, so the model may over-predict the rate of moisture ingress when applied to commercial models. Moreover, modules use adhesives to improve mechanical strength, which are also subject to degradation. Köntges reports that the adhesion promote in the EVA encapsulant is the least stable additive and limits the useful lifetime of the material [109]. Tracy et al. explored molecular mechanisms of adhesive degradation, which could be interesting to research further and incorporate in the moisture ingress model.

2.4.2. Optimisation

The mesh used to solve the COMSOL simulation was created to reduce computational time. First, a convergence test was performed, solving the problem using physics-controlled meshes of various sizes. This confirmed that the *normal* physics-controlled mesh delivered suitable results, which could be used to compare results from optimised meshes. This was a key step as different meshes deliver different results, and in the optimising stage it was essential that the results of the new mesh aligned delivered accurate results.

Optimising the mesh required consideration of moisture diffusion through the model, identifying areas where the diffusion process is more intricate, and where it is less so. The cell gap and the surrounding area was identified as a section that needed finer meshing, while the backsheet and top of the encapsulant sufficed with coarser meshing. The processes started with the default parameters for the *normal* physics-controlled mesh, which were then adapted and examined to understand the effect on the mesh and computational time.

Examining the statistics for the *normal* mesh and the *optimised* mesh, the average element quality (a parameter determined by COMSOL) for each is 0.69 and 0.58, respectively. Quality of 1 is the best, so the quality of the mesh has decreased, but it still delivers sufficient results. Favourable values of the other domain element statistics depends on the study, so a mesh refinement study should be performed to gain full confidence in the mesh.

The final mesh reduced the computational time by over half an hour; while this may not seem significant, it should be stressed that the run times reported in this thesis are from simulations run in optimal conditions (high processing power and no additional programmes on the computer). The time saved increases if the simulations are performed on computers with less memory and with other programmes running.

2.5. Conclusion

This chapter outlined the existing moisture ingress model developed by Daniel Jimenez Pelarda, and the mesh of the model was optimised further to reduce the computational time. First, it was verified that the physics-controlled meshes give cohesive results, against which the user-controlled meshes could be compared to ensure they delivered accurate results. The user-controlled mesh had increased maximum and minimum element sizes, and the growth rate was increased. A coarser mesh was created for the majority of the geometry, with a finer mesh required in the narrower region, specifically in the cell gap. The optimised mesh saves at least 23% on the computational time, a value that increases if the computer is running additional simulations.

3

Model improvements

The preceding chapter discussed several ways of modifying the moisture ingress model to more accurately simulate reality. This chapter explores non-Fickian diffusion through EVA and PET, and material degradation of EVA and PET. It provides relevant theory and research before applying it to the model of Kyranaki (hereafter called the “adapted model”). Kyranaki’s simulation and experimental results were outlined in subsection 2.2.3, and this chapter compares the proposed improvements to those results.

3.1. Non-Fickian diffusion

The complexity of moisture ingress in polymer materials is due various factors, such as crystallinity, microvoids, and polymer network structure. The complexity increases when many polymer materials are used, like in PV modules, because the moisture diffusion across the interfaces differs from the bulk [110].

An initial assumption in the development of the model was that the diffusion of moisture into a PV module obeys Fick’s 2nd law. This assumption was made because water diffusion into polymers has been widely investigated and, for most cases, the rate of diffusion has been assumed to be constant, i.e. Fickian diffusion is obeyed [111]. However, the accuracy of Fickian diffusion may sometimes fall short in predicting the ingress of moisture in PV modules when the encapsulant material is assumed to be homogenous; in reality, polymer materials can be non-homogeneous, leading to regions with different transport properties. This is primarily due to the model’s limitation at predicting diffusion through microchannels in polymer materials [110]. Mitterhofer et al. found that the measured ingress curves for various PV encapsulant materials showed significant deviation from the simulations in which Fickian diffusion was considered [112]. It was found that varying the value of the diffusion coefficient only resulted in a translation of the curves, not in a better fitting.

Several theories have been proposed to explain non-Fickian diffusion in polymeric materials. Some theories are based on the heterogeneity of the polymer, having two different values of D, based on polarity [114] and density [115] (i.e. two states of water are presumed). Water is ingressing either as a single molecule or as molecule clusters [116]. Other theories describe two different types of interaction between water and polymer. Water can be bound with single or multiple hydrogen bonds in hydrophilic polymers [117]. Another theory describes the sorption of water either in the free volume or in hydrogen-bonded clusters in the structure [118]. One theory presumes the material relaxation after hygroscopic swelling drives a second, slower diffusion process [119]. Some suggest the behaviour is caused by water molecules forming hydrogen bonds with hydrophilic polymer chains [117, 120].

Bhattacharyya et al. found that Fickian diffusion behaviour represents the actual moisture absorption well for relative humidity below 85% RH; above this threshold, the deviation becomes significant after 500 hours [121]. Additionally, Wong and Rajoo found absorption to exhibit Fickian behaviour at 30 °C, and non-Fickian behaviour at 85 °C [122]. They postulate the mechanism of non-Fickian diffusion based on the following three physics of moisture diffusion:

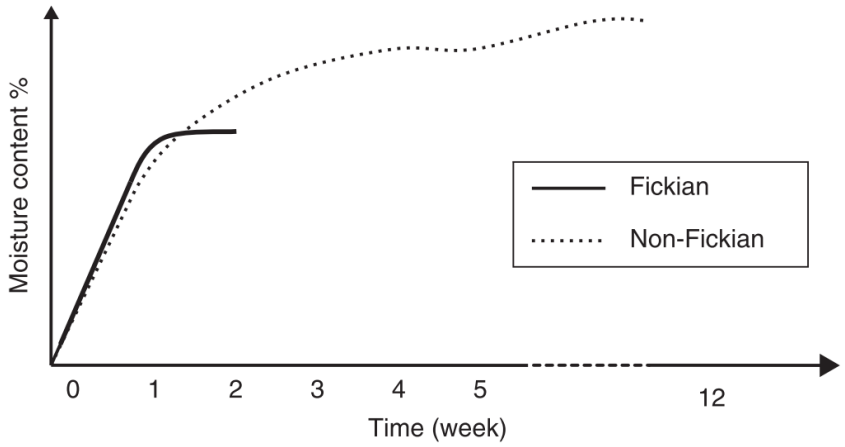

Figure 3.1: The typical trend for Fickian and non-Fickian moisture diffusion [113].

- Diffusion of moisture occurs along the packing materials' micropores.
- There are two ways that moisture could live in the micropores: at low moisture content in vapour form, and high moisture content in both water and vapour form.
- Vapour has a diffusivity that is at least one order of magnitude higher than that of water.

Based on this postulation, Wong and Rajoo deduced that the rate of moisture diffusion in the material is almost constant (Fickian behaviour) initially when the moisture in the micropores is in the vapour state and reduces gradually with increasing moisture content (non-Fickian behaviour) as condensation takes place. The one-dimensional diffusion equation given in Equation 1.1 can then be adjusted to describe non-Fickian diffusion by the following non-linear equation:

$$\frac{\partial C}{\partial t} = \frac{\partial}{\partial x}\left(D(C)\frac{\partial C}{\partial x}\right), \tag{3.1}$$

where $D(C)$ is the diffusion coefficient, dependent on moisture concentration. Wong et al. further proposed a means of characterising non-Fickian diffusivity in which Equation 3.1 is solved by using non-linear finite element method (FEM) [123]. The method defines diffusivity as a function of moisture content in the following way:

$$D(C) = a_0 + a_1\frac{C}{C_{\text{sat}}}, \tag{3.2}$$

where a_0 and a_1 are constant parameters and C_{sat} is the saturation concentration. This method requires experimental data to optimise a_0, a_1, and C_{sat}.

More recent simulation approaches considered a dual-stage model, with the notion that Fickian and non-Fickian diffusion occurs simultaneously [124]. This approach examines both absorption and desorption processes, described mathematically using a combination of Fickian terms for simplicity. This work provided a foundation for modelling anomalous moisture diffusion in FEM software. Other work has tried to combine molecular simulations and calculations of flow in nanochannels with macroscopic diffusion through membranes [125]. However, these approaches do not model diffusion for PV encapsulants.

Mitterhofer et al. attempted to bridge this gap and took a different approach to simulate moisture diffusion in PV encapsulants [112]. They use a dual-transport model, which assumes polymer sorption occurs in two stages [126]:

1. A rapid absorption into the surface sites.
2. Subsequent diffusion into the bulk materials.

This model is based on the inhomogeneity of encapsulant materials, simulating channels running through the bulk of the material, which drives the diffusion. Diffusion in both regions, as well as from one region to another, is simulated with Equation 1.1. The diffusion coefficients, D_B and D_C for the bulk and channels, respectively, are set such that diffusion is faster in the channels and slower in the bulk. The parameter D_B is varied and kept lower than D_C since the initial proposition was that bulk has a lower diffusion rate than the channels. A dimensionless parameter α is introduced as the ratio between D_B and D_C:

$$D_B = \alpha \cdot D_C,\ 0 \leq \alpha \leq 1. \tag{3.3}$$

If α = 1, Fickian behaviour is modelled. The simulations showed that setting α to a value greater than 0.1 gives Fickian ingress curves and, if α is reduced further, small amounts of moisture can pass via channels and reach the sensor without being absorbed in the bulk since the interaction with the bulk slows down significantly. The parameter is mathematical and not linked to the physical properties of materials. The saturation moisture contents in the bulk and channels are the same. Therefore, the key difference in this approach is that it implements a mesh with two diffusion coefficients, and the FreeFEM++ software is used. The study finds that the method can more accurately predict measured moisture ingress than the Fickian model.

Building on the work of Mitterhofer et al., Anagha et al. carried out dual-transport simulations in COMSOL [110]. They modelled moisture ingress for c-Si PV modules, taking EVA as the encapsulant, polyisobutylene (PIB) as the edge sealant, and considering an α value of 0.01. They confirm that moisture ingress is slower through PET-based backsheets than polyamide-based (PA) backsheets, leaving space to investigate additional backsheet and encapsulant materials.

This work takes a similar approach to model non-Fickian diffusion. Using the existing moisture ingress model in COMSOL, the geometry is adapted to create channels and the bulk. The geometry of the channels is shown in Figure 3.2 based on the work of Mitterhofer et al.

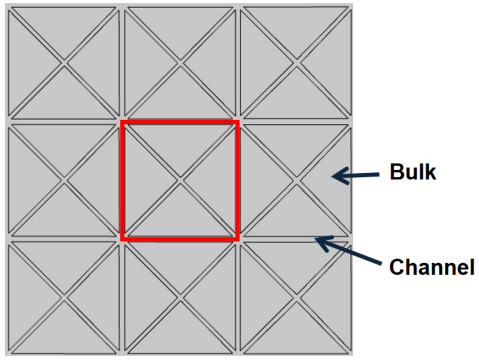

Figure 3.2: Dual-transport geometry, with the bulk and channels indicated, and a unit indicated with the red square.

Table 3.1: Optimised simulation parameters for EVA encapsulant [112].

Category	Parameter	Description	Reference value	Model value
Geometry	NF	Non-Fickian factor	15	Varying
	S_c (%)	Share of channels in the material	10	10
	$D_{B,EVA}$ (m^2/s)	Diffusion coefficient of the EVA bulk	1.4×10^{-15}	4.65×10^{-16}
	$D_{C,EVA}$ (m^2/s)	Diffusion coefficient of the EVA channels	4.5×10^{-10}	1.5×10^{-10}
	α_{EVA}	Ratio between $D_{B,EVA}$ and $D_{C,EVA}$	3.1×10^{-6}	3.1×10^{-6}

3.1.1. Non-Fickian diffusion through EVA

This section explores non-Fickian diffusion through the EVA encapsulant. The channels depicted in Figure 3.2 were applied to the adapted model. This model simulates a PET/EVA/EVA stack of width 2

mm, which is comparable to the model from Mitterhofer et al. [112]. The non-Fickian factor is defined as the number of units across the width of the sample. The moisture concentration profiles for non-Fickian factors 8, 16, 32, and 40 are shown below, denoted as NF: 8, 16, 32, 40, and can be compared to Fickian diffusion in Figure 2.4. The optimal value of α for EVA is used and the share of the channels is approximately 10% of the total encapsulant material. With the diffusion coefficient of the channels, D_C, determined by Kyranaki, the value of D_B could then be calculated. In the simulations, a coarser or extremely coarse mesh is used to obtain the concentration as a compromise between accuracy and computational time. As the non-Fickian factor increases, the mesh's coarseness must also increase.

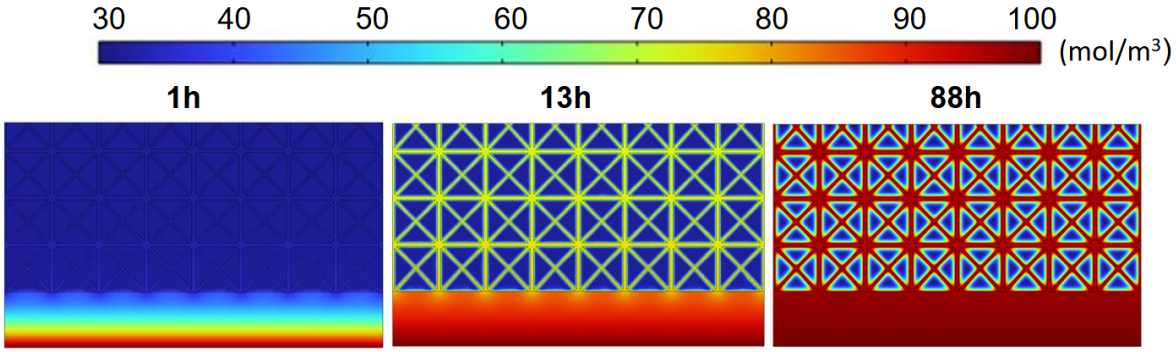

Figure 3.3: Moisture concentration profile for simulated non-Fickian diffusion through EVA with non-Fickian factor 8 (NF:8) at time 1 hour, 13 hours, 88 hours. The fast diffusion through the channels can be seen.

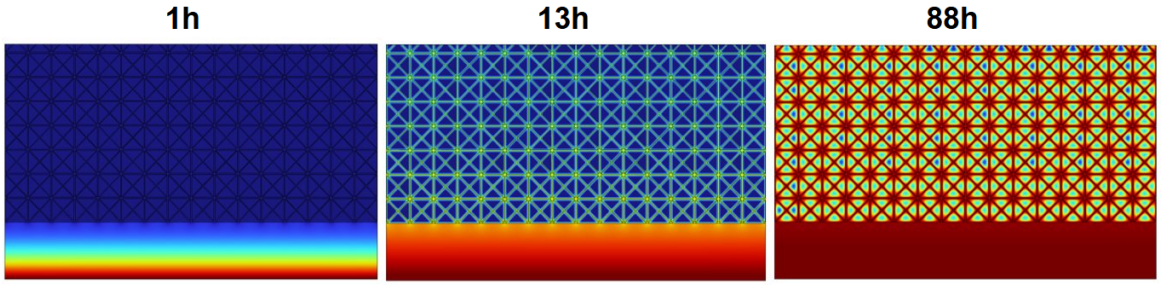

Figure 3.4: Moisture concentration profile for simulated non-Fickian diffusion through EVA with non-Fickian factor 16 (NF:16) at time 1 hour, 13 hours, 88 hours. The higher NF factor can be seen to drive diffusion in the bulk.

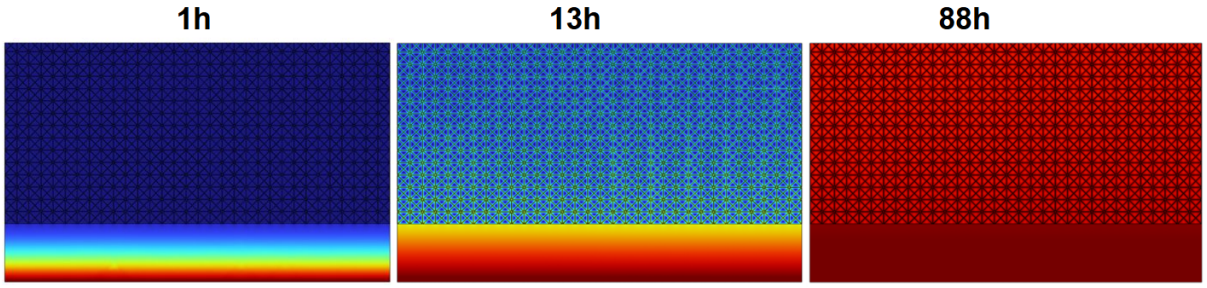

Figure 3.5: Moisture concentration profile for simulated non-Fickian diffusion through EVA with non-Fickian factor 32 (NF:32) at time 1 hour, 13 hours, 88 hours. The high NF factor has a greater influence on the rate of diffusion through the bulk.

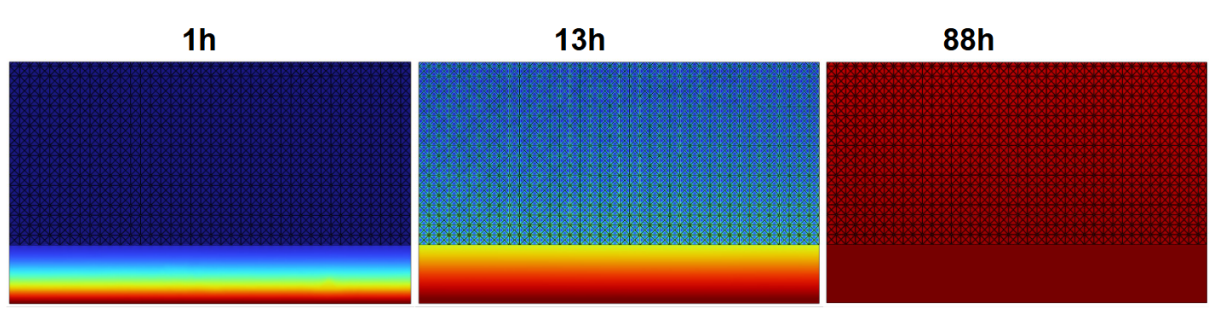

Figure 3.6: Moisture concentration profile for simulated non-Fickian diffusion through EVA with non-Fickian factor 40 (NF:40) at time 1 hour, 13 hours, 88 hours. The high NF factor has a greater influence on the rate of diffusion through the bulk.

To evaluate and compare the effect of the non-Fickian factor on moisture ingress, the surface average concentration of the EVA is found over 200 hours and compared to the experimental and simulated results from Kyranaki.

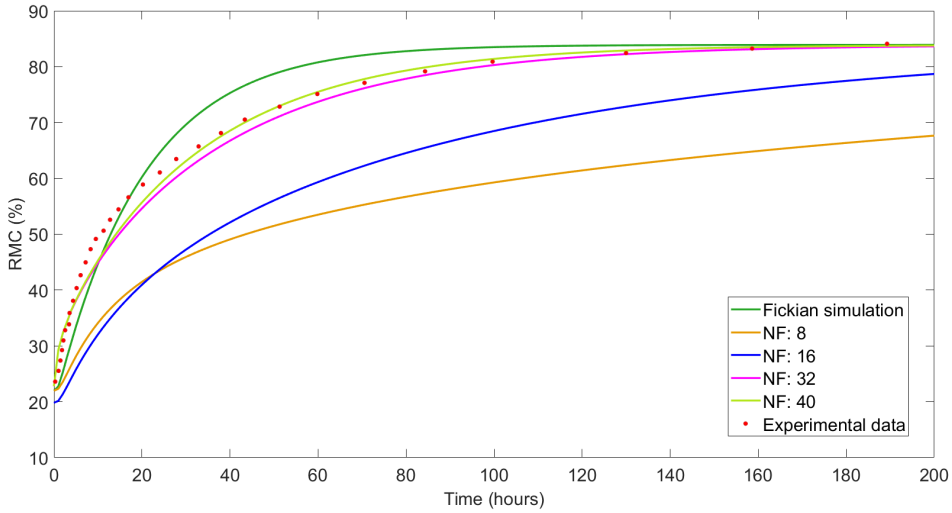

Figure 3.7: Comparison of the relative moisture content in the EVA encapsulant for Fickian and non-Fickian diffusion simulations through EVA and experimental data. NF:8 and NF: 16 show poor coherence with the experimental data, whereas NF: 32 and NF: 40 fit the experimental data well.

Figure 3.7 shows that NF: 8 and NF:16 strongly underperform, while NF: 32 and NF: 40 show good coherence with the experimental data. NF: 40 closely fits the experimental data from 40 hours and begins to exceed it, and NF: 32 takes longer to match the data. However, both NF: 32 and NF: 40 deviate from the experimental results at the start, particularly between 5 and 30 hours. The experimental RMC quickly increases at the start, indicating there is faster diffusion at the start through the backsheet. This is explored in subsection 3.1.2.

To quantify the fit of the Fickian and non-Fickian simulations with the experimental data, the following statistical formula is used:

$$\epsilon = \frac{\int (A - B)\mathrm{d}t}{(RMC_{\text{max}} - RMC_{\text{min}})(t_{\text{max}} - t_{\text{min}})}, \tag{3.4}$$

where A and B denote the two datasets being compared, one being the experimental data, the other a simulation, and ϵ is normalised. The results are summarised in Table 3.2. The analysis confirms that NF:32 and NF:40 perform the best, with NF:32 performing slightly better than NF:40.

Table 3.2: Statistical value ϵ for Fickian and non-Fickian simulations.

Non-Fickian factor	ϵ
Fickian	0.1066
NF: 8	0.2347
NF: 16	0.1138
NF: 32	0.0569
NF: 40	0.0719

The non-Fickian factors and corresponding dimensions of the units are summarised in Table 3.3 for analysis and application in other models. It should be noted that Mitterhofer et al. used units of dimension (1 $\times$ 1) $\times 10^{-4}$ m^2, which is close to NF: 16 and was found to be insufficient for this simulation.

Table 3.3: Non-Fickian factors for non-Fickian diffusion and corresponding dimensions.

Non-Fickian factor	Dimensions [m^2]
NF: 8	(2.5 $\times$ 2.5) $\times 10^{-4}$
NF: 16	(1.25 $\times$ 1.25) $\times 10^{-4}$
NF: 32	(0.625 $\times$ 0.625) $\times 10^{-4}$
NF: 40	(0.5 $\times$ 0.5) $\times 10^{-4}$

3.1.2. Non-Fickian diffusion through PET

Non-Fickian diffusion through backsheet materials is a largely unexplored area. Generally, for polymers in their rubbery state (above their glass-transition temperature, T_g), it is expected that the diffusion of small molecules might be Fickian [126, 127]. For PET, this temperature is in the range of 67 °C – 81 °C. PV modules are typically cooler than this temperature, so non-Fickian diffusion may occur. Sammon et al. investigated the non-Fickian diffusion of water and methanol through PET films [126]; they found that moisture ingress in PET appears to be Fickian, but the diffusion of methanol through PET does not follow Fick's law. Rather, they successfully used the dual-transport model to simulate methanol diffusion through PET. Nevertheless, the dual-transport model used in subsection 3.1.1 was applied to the PET to investigate the effect. Anagha et al. applied a dual-transport model and compared simulated moisture ingress for PA and PET-based backsheets [110]. They reported their simulation results for a coefficient α of 0.001; applying this to the adapted model gives values of $D_{C,BS}$ = 4.32$\times 10^{-12}$ m^2/s and $D_{B,BS}$ = 4.32$\times 10^{-15}$ m^2/s. The concentration profiles at hours 1, 13, and 88 are shown in Figure 3.8.

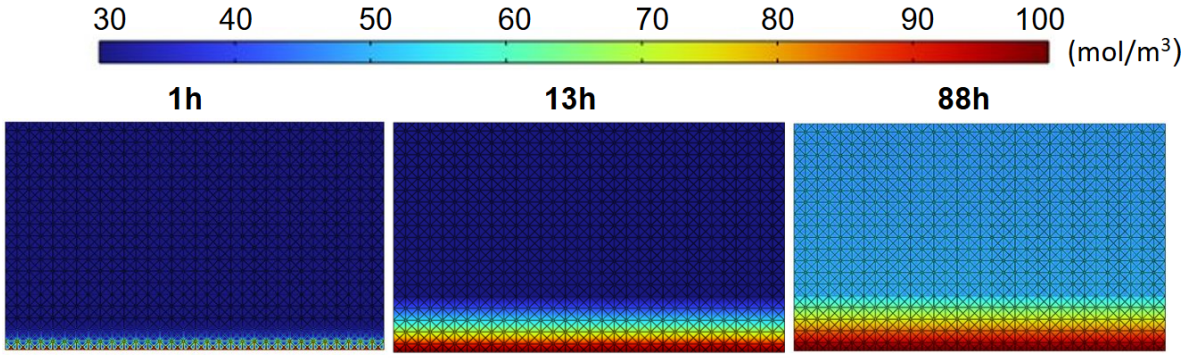

Figure 3.8: Moisture concentration profile for simulated non-Fickian diffusion through EVA/PET with non-Fickian factor 32 (NF:32) at time 1 hour, 13 hours, 88 hours. After 88 hours, there is minimal moisture ingress in the EVA because of slow diffusion through the PET.

It can be seen that diffusion through the backsheet is now much slower, and thus the concentration in the EVA is lower at a given time compared to simulations with Fickian diffusion in the backsheet.

Figure 3.9 compares the RMC of the non-Fickian simulation only in the EVA and the simulation with non-Fickian diffusion in both the EVA and the PET. The strong underperformance of the latter can be seen in yellow.

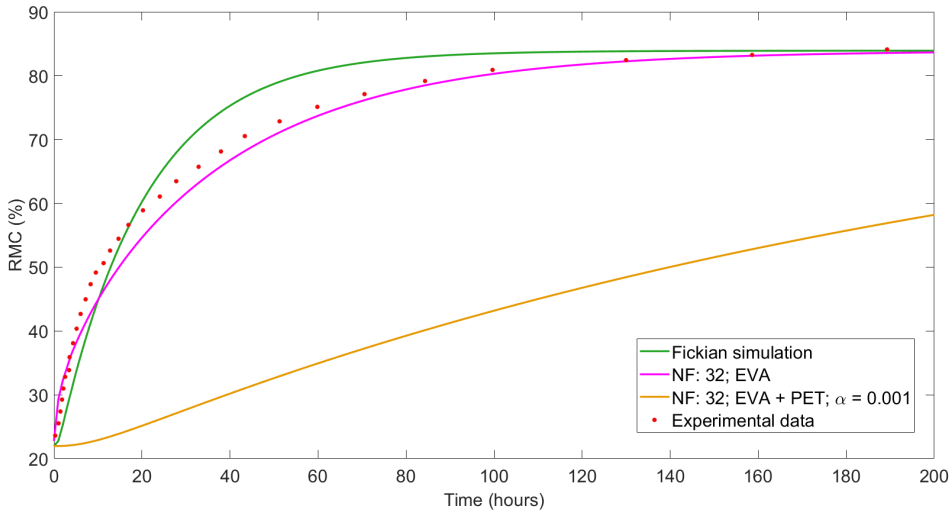

Figure 3.9: Non-Fickian diffusion through EVA and EVA/PET for NF: 32. Non-Fickian diffusion simulation through EVA/PET is limited by the diffusion through PET and deviates strongly from the experimental data.

Next, both the diffusion coefficients of the channel and bulk were increased to $D_{C,BS}$ = 4.32×10^{-9} m^2/s and $D_{B,BS}$ = 4.32×10^{-12} m^2/s, and $\alpha = 0.001$. This changes the proposal of Mitterhofer et al., assigning the determine diffusion coefficient of PET to the bulk instead of the channels. This simulation found that negligible moisture diffused from the backsheet into the encapsulant.

As it is only Anagha et al. that has investigated moisture diffusion via dual transport through PET, the value of α is explored in Figure 3.10. It can be seen that varying the value of α has insignificant effect on moisture diffusion through PET into the EVA. This indicates that the diffusion coefficient of the channels is the limiting factor, and that moisture diffusion through PET can best be approximated with Fickian diffusion.

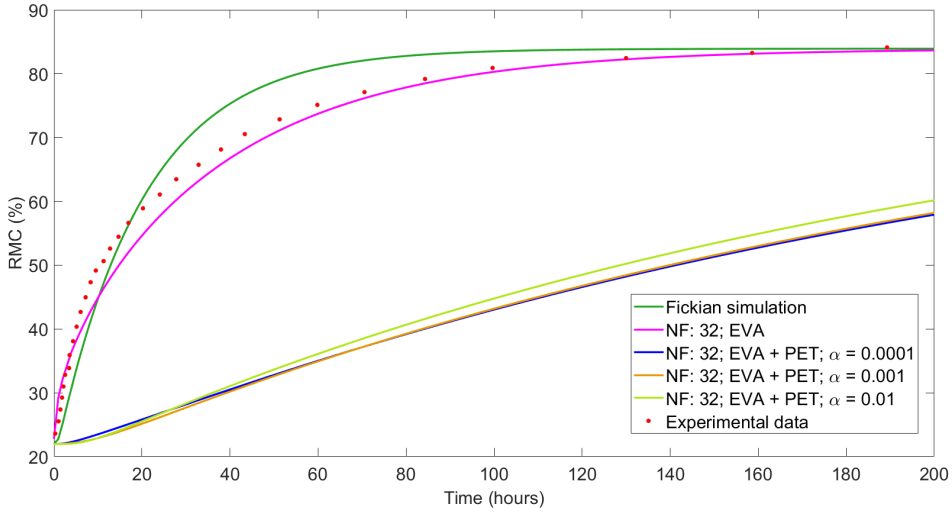

Figure 3.10: Non-Fickian diffusion through EVA/PET for NF: 32 with different values of α. Changing the value of α changes the simulated moisture ingress by a negligible amount.

3.1.3. Discussion of non-Fickian diffusion

A dual-transport model was used to simulate non-Fickian diffusion through EVA and PET; the results were fitted and compared to Fickian diffusion simulations and experimental data obtained by Nikoleta Kyranaki. The dual-transport model was found to more accurately simulate diffusion through the EVA, compared to Fickian diffusion, at higher non-Fickian factors, namely at NF:32 and NF:40, which corresponds to unit dimensions of (0.625 $\times$ 0.625) $\times$ 10^{-4} m^2 and (0.5 $\times$ 0.5) $\times$ 10^{-4} m^2, respectively. In their work, Mitterhofer et al. used units of dimension (1 $\times$ 1) $\times$ 10^{-4} m^2, which is closer to NF: 16 (1.25 $\times$ 1.25) $\times$ 10^{-4} m^2. NF: 16 was found to simulate non-Fickian diffusion through the sample poorly; the disparity in these results indicates there should further investigation into suitable channel dimensions in future work to find appropriate dimensions applicable to all moisture ingress models.

Furthermore, the geometry of the channels was assumed from the work of Mitterhofer et al.; alternative geometry may be more suitable in different materials and models. When the dual-transport model was applied to PET, it was found that the diffusion coefficient of the material severely limited diffusion. As moisture diffusion through PET using a dual-transport model has hardly been explored, the parameter α was varied, which was shown to have a negligible change on the diffusion. This indicates that this approach for simulating non-Fickian diffusion through PET is not suitable. Additionally, numerous authors have reported that moisture diffusion through PET is indeed Fickian. Numerous assumptions were made for the dual-transport model in PET, such as the share of the channels in the material and the geometry of the channels, could contribute to the incorrect approach. Further investigation can provide more insight into diffusion through PET.

3.2. Material ageing and degradation

Moisture in PV modules reacts with encapsulant and backsheet materials, causing them to change the material composition and produce degradation products. This change in the materials is not currently considered in the moisture ingress model, meaning the material composition is the same at the start of the simulation as it is at the end. To adapt the model to better simulate reality, this section considers the degradation reactions and means of integrating them into the model. This section focuses on EVA and PET due to their commercial use and previous research, and compares the findings to Kyranaki's experimental data.

In PV encapsulants, the EVA polymer is composed of ethylene (ET) and 28-33% in weight of vinyl acetate (VAc). The viscous EVA resin undergoes a cross-linking reaction during the lamination process, which thermally cures it and dramatically alters its chemical-physical properties [128].

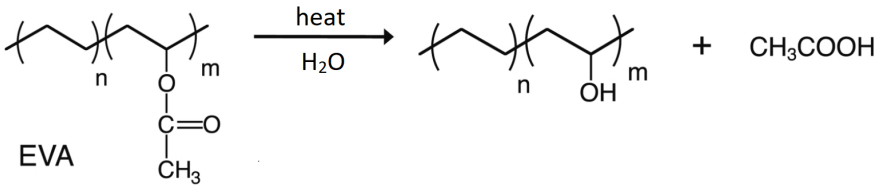

Figure 3.11: Hydrolysis of EVA. Adapted from [129].

The types of polymer degradation can be divided into three general categories: (i) without change in molecular weight, (ii) by undergoing chain scission, or (iii) by combining to form higher molecular weight compounds (i.e. cross-linking) [130]. When EVA undergoes hydrolysis, whereby it reacts with water and is broken into two molecules as seen in Figure 3.11, the molecular weight does not change significantly (case (i)). In general, the transformation can be written as:

$$P \xrightarrow{\text{k,EVA}} P^* + S, \tag{3.5}$$

where P is the (native polymer molecule), P^* is the degraded product, k is the rate of reaction, and (S denotes the small molecules produced in the reaction [131].

Due to its microstructure, PET typically degrades at temperatures above the glass transition temperature, T_g, in humid conditions [132, 133]. PET hydrolysis is a chain-scission reaction, meaning the number of molecules varies over time. The mechanism behind this hydrolysis reaction is not fully understood, but hydrolysis is thought to occur in the amorphous regions of the polymer. The reaction rate depends on the polymer's crystallinity, morphology, relative humidity and temperature [133].

The PET hydrolysis reaction scheme is depicted in Figure 3.12. The reaction scissions the polymer, producing terephthalic acid and ethylene glycol. PET polymers used for PV backsheets typically consist of chains of ∼100 repeating units. Sammon et al. found that hydrolysis degradation of PET occurs preferentially at the end of the polymer chain [133], meaning hydrolysis reactions reduce the number of units in a chain, changing the polymer's materials properties and decreasing its molar mass.

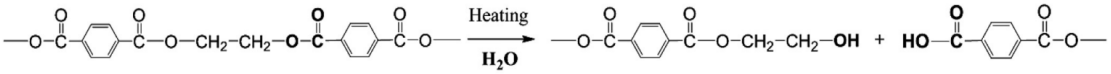

Figure 3.12: Hydrolysis of PET [134].

In this case, the most general reaction scheme is:

$$P \xrightarrow{\text{k,PET}} P^{'} + P^{''}, \tag{3.6}$$

where $P^{'}$ and $P^{''}$ are products of the reaction. This reaction splits the ester bonds in the polymer, leading to the formation of smaller molecules, like terephthalic acid and ethylene glycol.

Attempts at simulating material degradation in PV modules using COMSOL have not been reported. Recently, Brune et al. were able to connect material degradation and power loss of PV modules using advanced statistical methodology [135]. Other approaches quantify material degradation using mechanical and thermal characterization methods [136, 137].

Due to the complexity of these degradation mechanisms, a simplified approach is used to simulate material degradation in EVA and PET, which assumes the diffusion coefficient of each decreases approximately linearly over time at different rates for each material. The simulations are fitted and compared to the experimental results from Kyranaki. Equation 2.1 assumes that water diffusion does not influence the physical properties of polymers, so the equation is adapted to reflect the degradation caused by hydrolysis. Now, the pre-exponential factor would become time-dependent; under the assumptions, this is analogous to the factor being dependent on the concentration of the degraded product.

$$D_{\text{EVA, PET mat deg}} = D_0(t)\exp\left(\frac{-E_a}{R \cdot T}\right). \tag{3.7}$$

This equation is revised to apply it to Kyranaki's scenario. Returning to the experimental results, the hypothesis is that the diffusion coefficient decreases over time, due to the change in material composition and degradation products. As only the diffusion coefficient is given, Equation 3.7 becomes:

$$D_{\text{EVA, PET mat deg, Kyranaki}} = \frac{1.5 \times 10^{-10}}{\exp(\gamma \cdot t)}, \tag{3.8}$$

where γ is the degradation constant. The PV sample considered was subject to 200 hours of damp heat at 50 °C and 85% RH. Furthermore, the water vapour transmission ratio (WVTR), defined in Equation 1.3, is considered in the determination of γ, as it gives an indication as the to rate of diffusion through the materials. Jorgensen et al. found that the WVTR for EVA and PET at 37.8 °C and 85% RH is 33 g/(m^2 · day) and 2.3 g/(m^2 · day), respectively, for their typical thicknesses [138]. The WVTR of EVA is over 10 times greater than that of PET, indicating diffusion through the material is faster and suggesting the value of γ for EVA will be greater than for PET.

First, the degradation of EVA was considered. Several values of γ were tested, the most successful of which are plotted in Figure 3.13. It can be seen that when γ = 0.03, the diffusion coefficient

hardly changes over time, so negligible degradation is simulated, whereas when γ = 0.09, $D_{\text{EVA, mat deg}}$ changes more significantly. To assess the most suitable value of γ, Equation 3.4 is used. The calculated values for ϵ are summarised in Table 3.4. It can be inferred that the optimal value of γ_{EVA} lies in the range of 0.04 - 0.06.

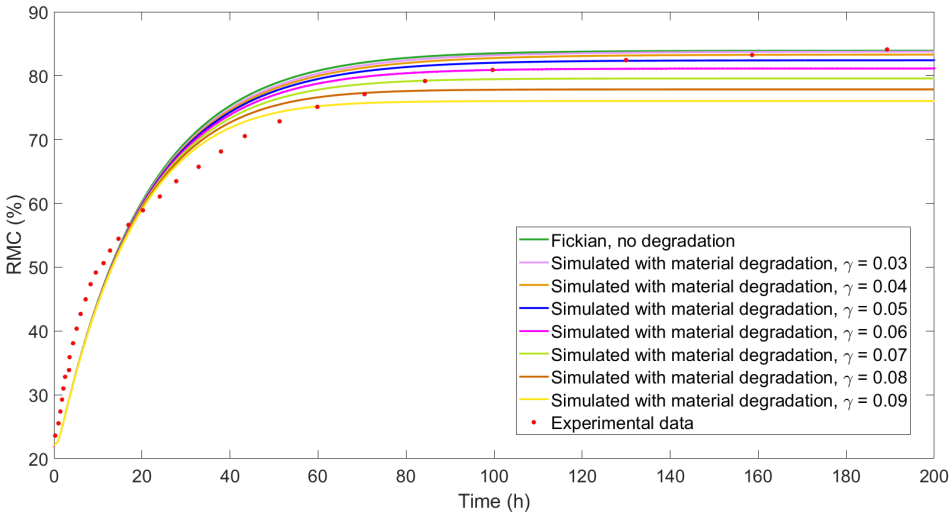

Figure 3.13: Comparison of γ factors for EVA. Increasing γ finds the simulation saturates at a lower RMC.

Table 3.4: Statistical value ϵ for different values of γ for EVA.

Value of γ_{EVA}	0.03	0.04	0.05	0.06	0.07	0.08	0.09
ϵ	0.0412	0.0370	0.0349	0.0368	0.0439	0.0549	0.0691

A value of γ_{EVA} = 0.05 appears to give the best fit for EVA, but fitting a value for PET may alter this; therefore, values of γ_{EVA} = 0.04, 0.05, 0.06 were explored. As the WVTR of EVA is over 10 times greater than that of PET, an initial guess of γ_{PET} = 0.005 is made. γ_{PET} = 0.01 is simulated to compare the effect of changing γ_{PET}.

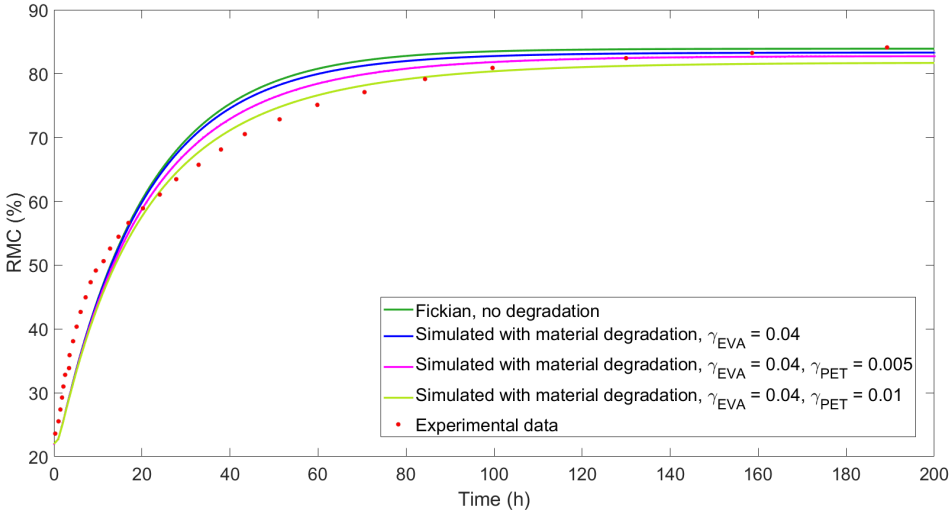

Figure 3.14: Comparison of γ factors for PET, γ_{EVA} = 0.04. The simulations that incorporate PET degradation better fit the experimental results.

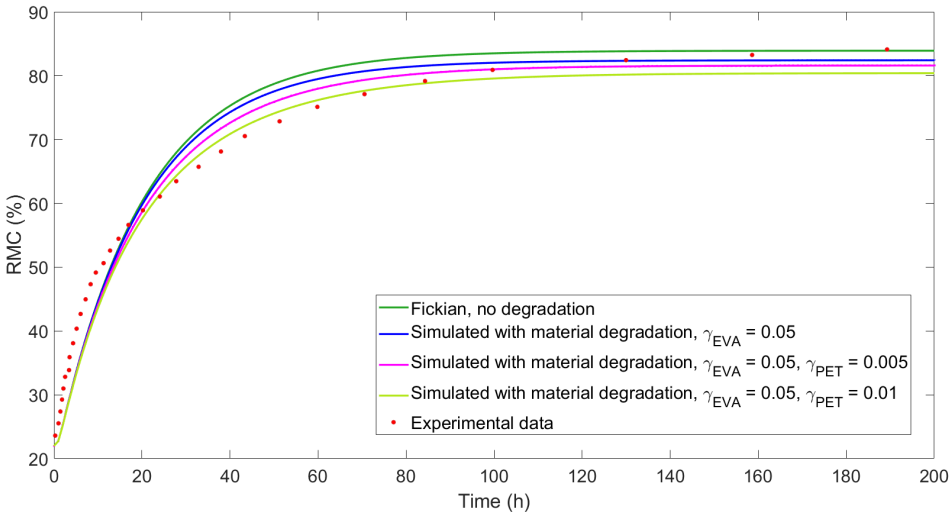

Figure 3.15: Comparison of γ factors for PET, γ_{EVA} = 0.05. The simulations that incorporate PET degradation better fit the experimental results.

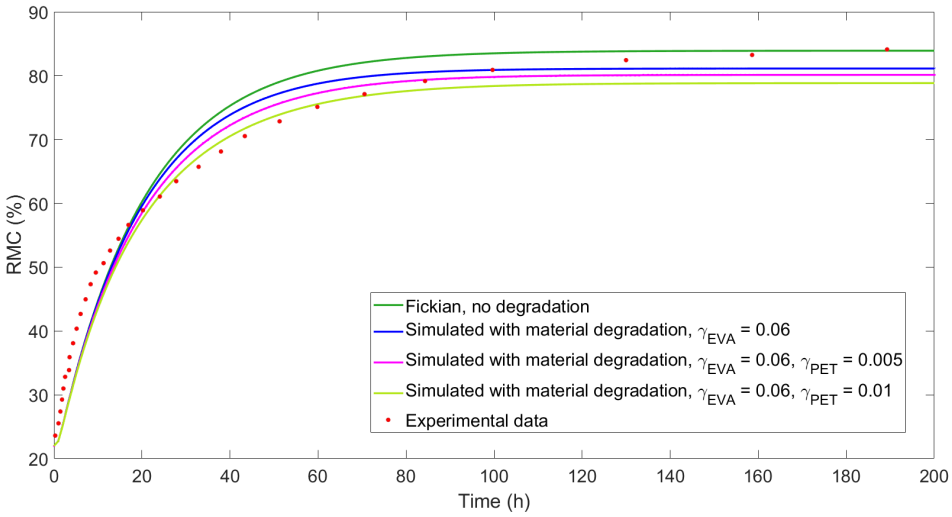

Figure 3.16: Comparison of γ factors for PET, γ_{EVA} = 0.06. The simulations that incorporate PET degradation underestimate the experimental results.

It can be seen that the curve fits better in the region of 20 to 70 hours for γ_{PET} = 0.01 for all values of γ_{EVA}. To distinguish between Figure 3.14, Figure 3.15, and Figure 3.16, the statistical value ϵ is calculated and summarised in Table 3.5.

Table 3.5: Statistical value ϵ for different values of γ for EVA and PET.

	γ_{PET} = 0.005	γ_{PET} = 0.01
γ_{EVA} = 0.04	0.0280	0.0255
γ_{EVA} = 0.05	0.0303	0.0325
γ_{EVA} = 0.06	0.0372	0.0432

The combination of γ_{EVA} = 0.04 and γ_{PET} = 0.01 appears to deliver the best fit to the experimental results. However, they are not necessarily the optimal results; this is discussed in subsection 3.2.1. As γ_{PET} = 0.004 is more consistent with the material properties of PET, it is in the next chapter.

3.2.1. Discussion of material degradation and ageing

This section proposed a means of simulating material degradation in COMSOL: adapting the diffusion coefficient to decrease over time. This was proposed as a possible reason for the discrepancy between the experimental and simulated results. However, the hydrolysis reactions cause a change in the structure of the material and its porosity; the porosity is expected to increase, which would result in higher diffusion coefficients. Two possible reasons for decreasing the diffusion coefficient are offered. Firstly, it may not be material degradation that is being observed, but rather a different mechanism that lowers the diffusion coefficient, such as increased cross-linking and crystallinity. Secondly, the acids produced from the hydrolysis of EVA and PET may restrict moisture diffusion, reducing the effective diffusion coefficient of the material. It should also be noted that the short run-time of the accelerated tests means it is unlikely any significant material degradation would be observed.

The simplified approach found suitable parameters that appeared to simulate material degradation and better fit the experimental data. However, each simulation assumed Fickian diffusion, so the profiles saturated after 100 hours, and it was established in section 3.1 that the experimental data takes longer to saturate. Furthermore, it was assumed that the revised diffusion coefficient would degrade at an hourly rate under accelerated tests; this assumption was made to simplify the approach, but more experimental work and understanding behind the mechanisms is required to substantiate it, or to find an alternative approach.

The degradation reactions and products considered were the direct hydrolysis reactions and products. However, additional degradation products that have been documented in the literature include lactones, ketones, and acetaldehyde. Moreover, during oxidation processes, anhydrides, hydroperoxide, and a,b-unsaturated carbonyl groups are produced [35]. Interaction between these additional species and PV materials could affect the diffusion process and requires more research.

3.3. Conclusion

This chapter explored means of simulating non-Fickian diffusion and material degradation through EVA encapsulants and PET backsheets. To simulate non-Fickian diffusion through the materials, a dual-transport method was employed whereby channels in the material were defined, through which diffusion occured faster than in the bulk of the material. The simulation results were compared to experimental results from Kyranaki, and it was found that dual-transport through the EVA gave favourable results, but its applicability to PET is doubtful. Furthermore, the simulation of material degradation considered hydrolysis reactions and WVTR of materials, and it incorporated a time-dependent pre-factor in the diffusion coefficient equation. While these simulations better assimilated the experimental results, further investigation is needed to find the optimal pre-factors for EVA and PET.

4

Material and Climate Variability Analysis

To understand how different PV modules are affected by moisture ingress, and in different environments, the findings from chapter 3 are applied. The encapsulant materials explored are: TPO, ionomer, POE; the backsheet materials that are explored are: PA and TPT. Each material is explored under the same climate conditions, namely in Delft. Climates can be classified by the Köppen-Geiger climate classification; it is based on temperature and precipitation and has five basic climatic types: tropical, arid, temperate, continental, and polar. The chosen locations for each climate type are Gran Canaria (Spain), Almeria (Spain), Los Angeles (USA), Oslo (Norway), and Zugspitze (Germany). Each climate is explored with an EVA encapsulant and PET backsheet.

4.1. Materials and climate overview

This section provides an overview of the materials explored in this chapter, and the classification of climates.

4.1.1. Alternative PV materials

The limitations of using EVA and PET for PV modules were outlined in section 3.2. This section provides an overview of alternative PV materials, some of which are explored with regard to non-Fickian diffusion and material degradation later in the chapter. These materials were chosen for this investigation as their diffusion parameters were available in literature.

Thermoplastic polyolefin (TPO)

Thermoplastic polyolefin (TPO) is a non-crosslinking polymer material used as a PV module encapsulant [139]. The crosslinking step is not required as the material typically has a higher melting temperature, giving the module sufficient stability. Therefore, for non-crosslinking TPO encapsulants, the gel content or crosslinking density is always zero, avoiding the negative effects associated with peroxide-assisted crosslinking process [21]. The main advantage of TPO is that it does not produce acetic acid during degradation [140]. Fourier-transform infrared spectroscopy (FTIR) has demonstrated that TPO has a lower water absorption compared to EVA because of its nonpolar nature [139]; specifically, it was found that TPO has a water vapour transmission rate (WVTR) 7 times lower than that of EVA [141]. Additionally, TPO's low cost makes it an attractive candidate for encapsulant choice [20]. TPO's main drawback is that it has a low glass transition temperature, meaning there is a higher chance of embrittlements and delamination at lower temperatures. However, TPO's favourable properties mean it is forecasted to increase its market share in the coming decade [142].

Ionomer

Ionomers, specifically ethylene ionomers, are made of ethylene and unsaturated carboxylic acid comonomers and fall within the category of thermoplastic encapsulant materials. Despite their high production costs, ionomers are a desirable PV encapsulant material because to their exceptional optical

transmittance and exceptionally low permeability [143, 144]. Ionomer is the least permeable PV material considered, with a WVTR approximately 10 times lower than that of PET [144, 145]. Furthermore, ionomers do not form acetic acid as a reaction product, and they do not require a crosslinking step, shortening the lamination times [143]. Ionomers' long-term viability for terrestrial photovoltaic applications has not been well studied, and the field data that is currently available suggests that they may be susceptible to delamination. Tracy et al. find that the adhesion of ionomers to glass and solar cell is inferior to EVA, and it particularly susceptible to delamination [143].

Polyolefin Elastomer (POE)
POE has several properties in common with other encapsulant materials: it is a member of the polyolefin group, like TPO [142], and it is a crosslinked PV encapsulant, like EVA. The gel formation time for POE is substantially longer than that of EVA, although the curing time for both is around the same [142]. Similar to TPO, POE's advantage over EVA is that it does not produce acetic acid during degradation [140]. Due to its lower potential-induced degradation (PID) than EVA, hydrocarbon-based POEs have recently been investigated as a new polymeric encapsulating material for PV modules [146]. Unfortunately, the WVTR of POE is not low enough to make it an attractive alternative encapsulant material [147].

Polyamide (PA)
Polyamides (PAs) are thermoplastic polymers, popular due to their high mechanical strength and stability [29]. PAs can undergo hydrolysis, whereby water reacts with the amide group and induces chain scission [148]. The process can be catalysed by the presence of acids or heat. The WVTR of PA is approximately twice to that of PET [144].

TPT
Tedlar-Polyester-Tedlar (TPT) is a composite layer film used as a backsheet for PV modules, one of the few multi-layer backsheets that use minimal materials. TPT has excellent mechanical properties, with a larger Young's modulus than PET and PA backsheets [29]. The WVTR of TPT is found to be very similiar to that of PET, around 8.5 g/m^{2}d [149].

4.1.2. Climate classifications

The Köppen classification is based on the annual cycle of monthly air temperature and precipitation data; since then, the Köppen-Geiger classification (KGC) has been developed, based on Köppen's original approach. KGC describes the environment based on how it affects plant development, which is mostly dependent on temperature and aridity. KGC classifies climate into five main classes: tropical zone (A), arid zone (B), temperature zone (C), snow zone (D), and polar zone (E), the basic definitions of which are outlined in Table 4.1 [150]. P_{ann} and P_{th} denotes the annual precipiation and the threshold precipiation (cm), respectively, where $P_{\text{th}} = 2 \times T_{\text{ann}}$. T_{hot} is the air temperature of the hottest month, T_{cold} is the air temperature of the coldest month, and T_{ann} is the annual mean near-surface (2 m) temperature [151].

Table 4.1: Key definitions of major climate zones by the Köppen-Geiger classification, with temperature in °C and precipitation in cm [150, 151].

KGC		Definition
A	Tropical	$T_{\text{cold}} \geq 18$
B	Arid (dry)	$P_{\text{ann}} < 10\ P_{\text{th}}$
C	Temperate	(Original) $T_{\text{hot}} > 10$ and $-3 < T_{\text{cold}} < 18$ (Updated) $T_{\text{hot}} > 10$ and $0 < T_{\text{cold}} < 18$
D	Cold (snow/continental)	(Original) $T_{\text{hot}} > 10$ and $T_{\text{cold}} < -3$ (Updated) $T_{\text{hot}} > 10$ and $T_{\text{cold}} < 0$
E	Polar	$T_{\text{cold}} \leq 10$

In this chapter, the following locations are chosen: Gran Canaria (A), Almeria (B), Los Angeles (C), Oslo (D), and Zugspitze (E). It should be noted that the Delft, the location used for the material analyses, is classed as a temperate (C) climate.

4.2. Non-Fickian diffusion

This section explores non-Fickian diffusion through other PV materials that have an increasing presence in the market. Due to the drawbacks of EVA outlined in section 1.1, it is forecasted that the market share for EVA will decrease in the coming decade, with the share of polyoelefin encapsulant materials increasing [142]. Section 3.1.1 found NF: 32 and NF: 40 to be suitable for non-Fickian simulations, corresponding to units of size $(0.625 \times 0.625) \times 10^{-4}$ m^2 and $(0.5 \times 0.5) \times 10^{-4}$ m^2, respectively. Due to the sizing of the model and the limitations of the software, NF: 40 is applied. Due to computational limitations, NF: 40 could not successfully be applied to the original moisture ingress model, and thus this section focuses on the application to the adapted model.

4.2.1. Non-Fickian diffusion in different PV materials

A study has indicated that Fickian models for other PV encapsulants also show limited accuracy in modelling moisture ingress [152]. Consequently, Mitterhofer et al. simulated non-Fickian diffusion through four different encapsulant materials: EVA, TPO, POE, and ionomer. Table 3.1 outlines the optimised diffusion coefficient of the channels, the optimised coefficient of α, and the channels' share, S_c. These parameters were found by fitting measured ingress curves at 20% to 60% RH at 50 °C. The optimised share of channels is reported as $S_{c_{\text{Mitt.}}}$ to distinguish from the share of channels used in the COMSOL simulation; a higher share of channels had to be used for all encapsulant materials due to limitations in the software.

Table 4.2: Optimised parameters for non-Fickian diffusion through different encapsulant materials [112].

Parameter	EVA	TPO	POE	ionomer
D_c (10^{-10} m^2/s)	4.5	7.5	10	0.72
α ($\times 10^{-6}$)	3.1	4	1.5	14
$S_{c_{\text{Mitt.}}}$ (%)	10	2	2	4
S_c (%)	10	10	10	10

The parameters outlined in Table 4.2 were applied to the model of Kyranaki to gain initial insight into the behaviour of the materials. The varying diffusion coefficients and values of α between the materials does not indicate distinct behaviour pattern, so simulations are required to understand their nature. The coefficients were deduced at a temperature of 50 °C, and the sample begins with a concentration of 26.86 mol/m^3 and a concentration of 102.56 mol/m^3 is applied for 200 hours. The average concentration in the encapsulant at each time-step is found and compared for each material, plotted in Figure 4.1.

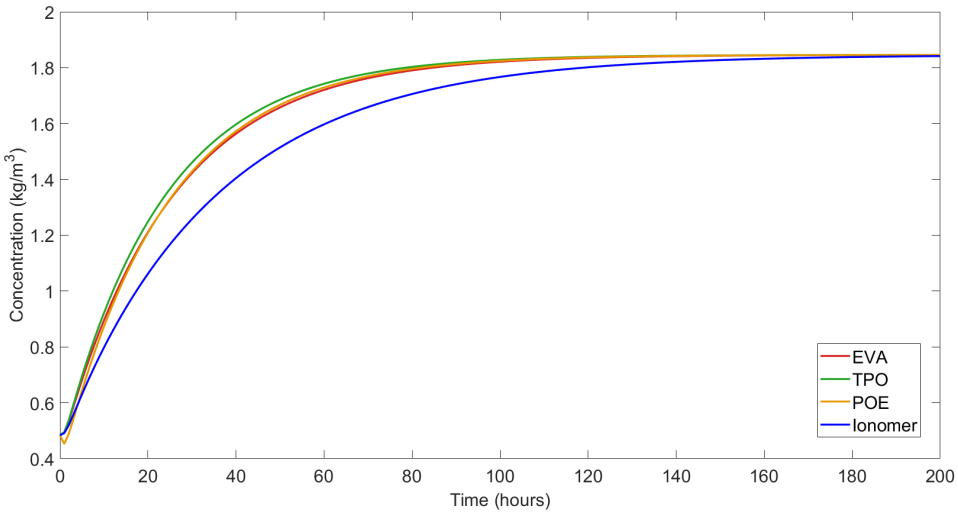

Figure 4.1: Concentration in different PV encapsulants for non-Fickian diffusion. Ionomer shows slower moisture ingress than EVA, TPO, and POE.

To understand how the non-Fickian behaviour for each material compares to simulated Fickian behaviour, the concentration is plotted and compared in Figures 4.2 to 4.5.

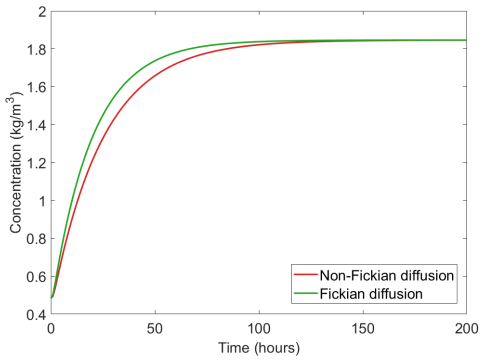

Figure 4.2: Concentration in EVA encapsulant for Fickian and non-Fickian diffusion. The non-Fickian simulation shows some deviation from the Fickian simulation until 120 hours.

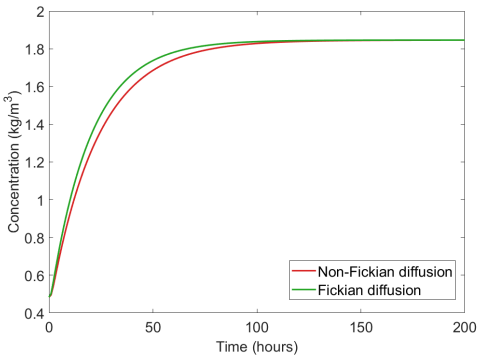

Figure 4.3: Concentration in TPO encapsulant for Fickian and non-Fickian diffusion. The non-Fickian simulation shows little deviation from the Fickian simulation until 100 hours.

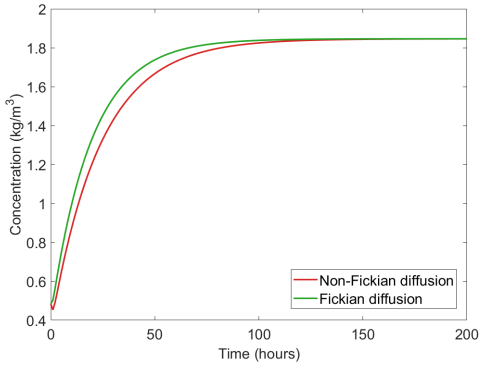

Figure 4.4: Concentration in POE encapsulant for Fickian and non-Fickian diffusion. The non-Fickian simulation shows some deviation from the Fickian simulation until 100 hours.

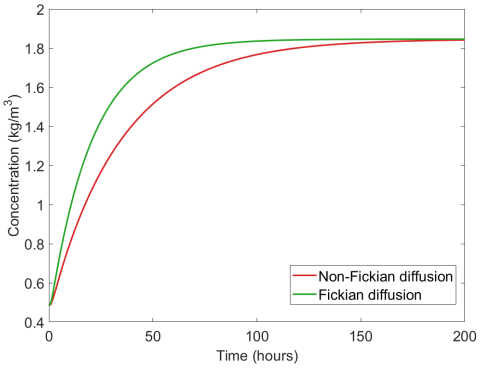

Figure 4.5: Concentration in ionomer encapsulant for Fickian and non-Fickian diffusion. The non-Fickian simulation deviates strongly from the Fickian simulation until 170 hours.

It can be seen that the non-Fickian diffusion simulation through TPO does not deviate from Fickian as strongly as through ionomer. EVA and POE sees some deviation, similar in behaviour. This indicates that assuming Fickian diffusion may be suitable for TPO encapsulants, but non-Fickian behvaiour is stronger in EVA and POE, and especially ionomer, encapsulants. A higher value of the parameter α corresponds to stronger non-Fickian behaviour.

In order to investigate how each material performs in realistic-operation conditions, non-Fickian diffusion through EVA, TPO, and ionomer was simulated for 1 month in Delft using the parameters given in Table 4.3. POE was not simulated as the moisture parameters were not available. Due to the large computational time required to run the simulations for a year or longer, the simulations are run for 1 month to observe initial moisture ingress. The optimal coefficient α for each material, given in Table 4.2, was used for the simulations.

Table 4.3: Moisture parameters for different encapsulant materials [153].

Parameter	EVA	TPO	Ionomer
D_0 (m^2/s)	2.31×10^{-4}	5.22×10^{-2}	1.5×10^{-3}
$E_{a,D}$ (kJ/mol/K)	38.1	52.9	55.6
S_0 (g/m^3)	1.81×10^{6}	1.56×10^{6}	1.78×10^{7}
$E_{a,S}$ (kJ/mol/K)	16.7	24.6	19.5

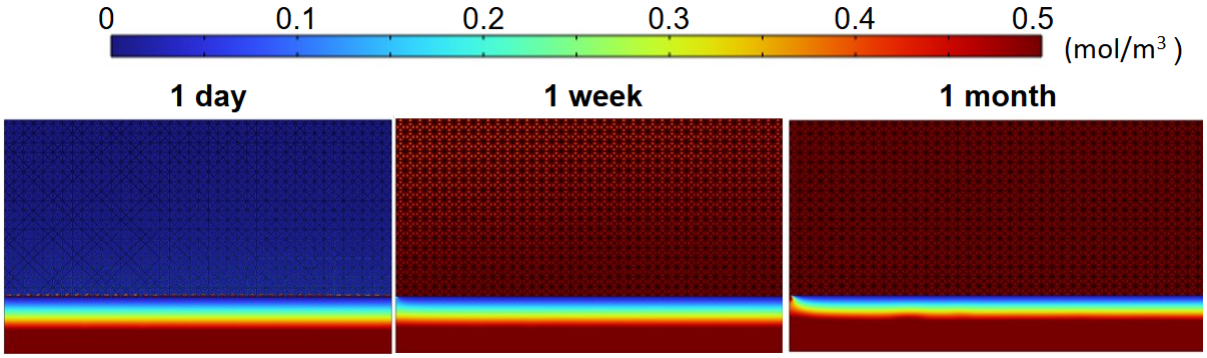

Figure 4.6: Moisture concentration profile for simulated non-Fickian diffusion through EVA with non-Fickian factor 40 (NF:40) in Delft at time 1 hour, 1 week, 1 month. Very fast diffusion through the channels is observed.

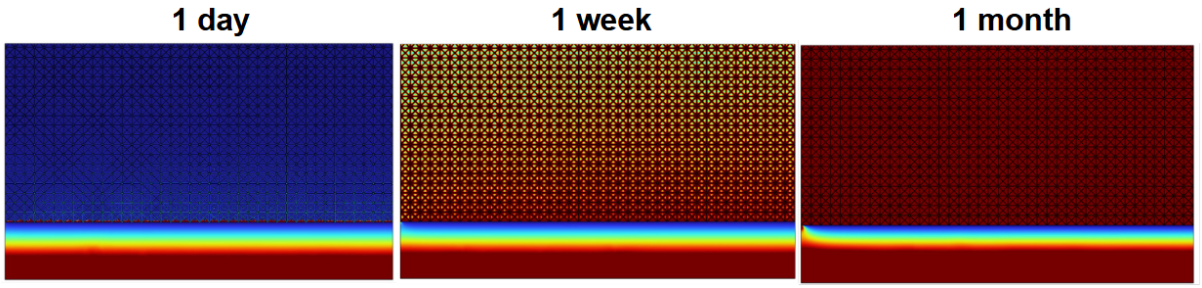

Figure 4.7: Moisture concentration profile for simulated non-Fickian diffusion through TPO with non-Fickian factor 40 (NF:40) in Delft at time 1 hour, 1 week, 1 month. Non-Fickian diffusion can be seen best in 1 week: moisture has diffused through the channels and is diffusing through the bulk.

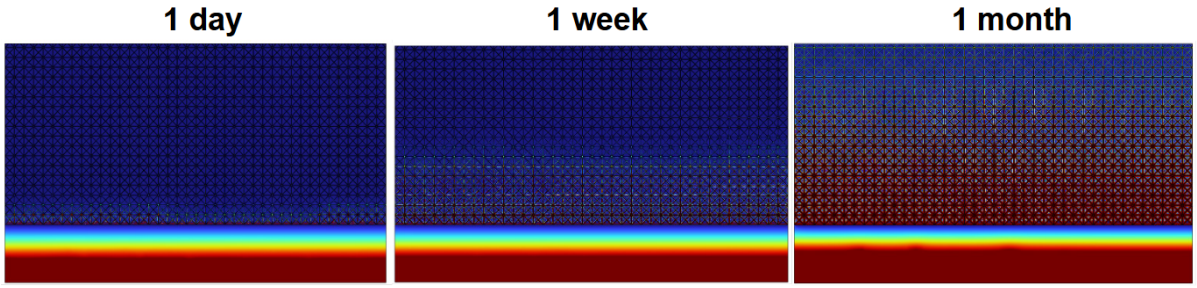

Figure 4.8: Moisture concentration profile for simulated non-Fickian diffusion through ionomer with non-Fickian factor 40 (NF:40) in Delft at time 1 hour, 1 week, 1 month. Very slow diffusion through the channels is observed. The higher concentration in the bottom encapsulant and low concentration in the top highlights the slow diffusion due to small diffusion coefficients and parameter α.

The diffusion through the channels can be seen most prominently in the middle figure of Figure 4.7. Given TPO has the highest value of D_0, it might have been expected that the fastest diffusion would be seen through this material, but Figure 4.6 shows that moisture diffuses fastest through EVA, and Figure 4.8 shows the slower diffusion of moisture through ionomer. The contrast between the high and low concentration in the bottom and top ionomer encapsulants, respectively, highlight how the channels can slow down diffusion.

4.2.2. Non-Fickian diffusion in different climates

To examine non-Fickian diffusion in different climates, the simulation is run with EVA and PET as the encapsulant and backsheet materials, using the parameters outlined in Table 3.1 and Table 4.4. For each climate, the Fickian and non-Fickian simulations are compared.

Table 4.4: Moisture parameters used for non-Fickian diffusion climate variability analysis [154].

Diffusion parameters	Value	Solubility parameters	Value
$D_{0,\text{EVA}}$	2.46×10^{-4} m^2/s	$S_{0,\text{EVA}}$	2.91×10^{5} g/m^2
$E_{a,D,\text{EVA}}$	38970 J/mol/K	$E_{a,S,\text{EVA}}$	12580 J/mol/K
$D_{0,\text{PET}}$	1.01×10^{-9} m^2/s	$S_{0,\text{PET}}$	1.01×10^{14} g/m^3
$E_{a,D,\text{PET}}$	17150 J/mol/K	$E_{a,S,\text{EVA}}$	69960 J/mol/K

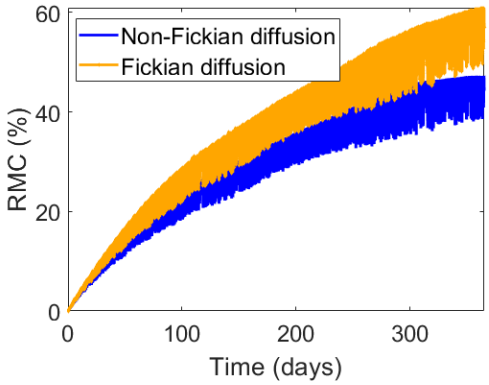

Figure 4.9: Average RMC in the EVA encapsulant in Gran Canaria after 1 year, simulating Fickian and non-Fickian diffusion through the EVA. A similar trend between the two simulations is observed, with slower ingress in the non-Fickian simulation.

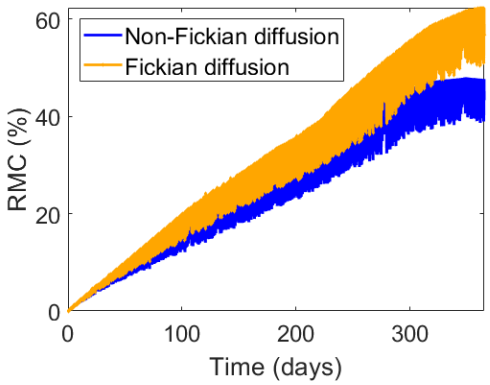

Figure 4.10: Average RMC in the EVA encapsulant in Almeria after 1 year, simulating Fickian and non-Fickian diffusion through the EVA. A similar trend between the two simulations is observed, with slower ingress in the non-Fickian simulation.

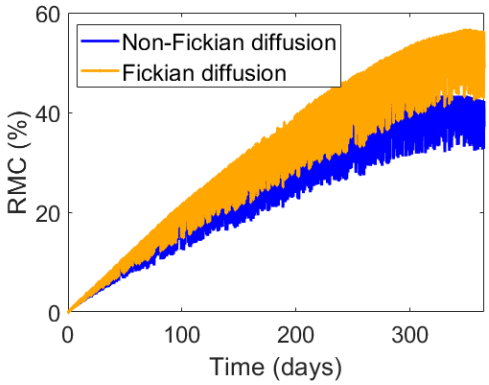

Figure 4.11: Average RMC in the EVA encapsulant in LA after 1 year, simulating Fickian and non-Fickian diffusion through the EVA. A similar trend between the two simulations is observed, with slower ingress in the non-Fickian simulation.

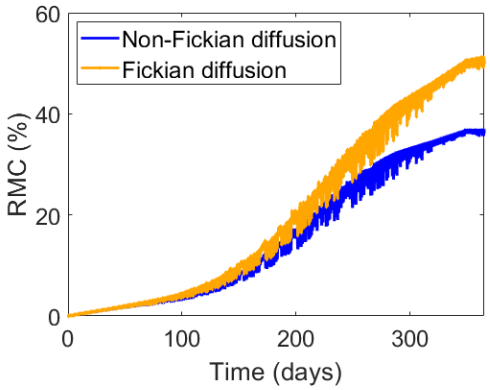

Figure 4.12: Average RMC in the EVA encapsulant in Oslo after 1 year, simulating Fickian and non-Fickian diffusion through the EVA. There is less daily variation, so the difference between the Fickian and non-Fickian simulations is more prominent.

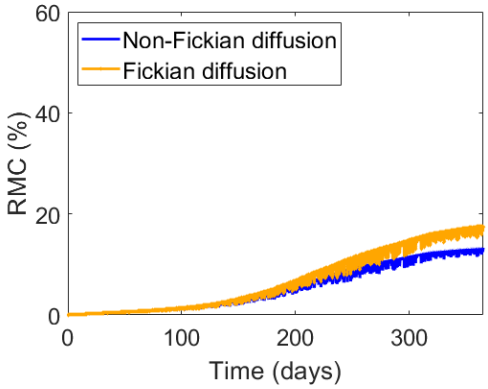

Figure 4.13: Average RMC in the EVA encapsulant in Zugspitze after 1 year, simulating Fickian and non-Fickian diffusion through the EVA. There is negligible deviation between the simulations until around 200 days, after which the deviation remains small.

The simulations exhibit similar trends: RMC increases approximately linearly for the diffusion processes, with non-Fickian diffusion simulating slower moisture ingress. To assess the deviation between the Fickian and non-Fickian simulations for each climate, the Mean Absolute Difference (MAD) is found for each climate. This statistical measure is chosen as it is a straightforward way to interpret the magnitude of the difference between the simulations. The MAD is calculated by dividing the sum of the absolute difference between the datasets by the number of points:

$$\text{MAD} = \frac{1}{n}\sum_{i=1}^{n}|y_i - \hat{y}_i|, \tag{4.1}$$

and the results are summarised in Table 4.5 and Figure 4.14 shows the relation between the mean annual temperature of the location and the MAD between the Fickian and non-Fickian simulations. It indicates that there is stronger deviation between Fickian and non-Fickian simulations in warmer climates, although more simulations in different locations are needed to confirm this postulation. Zugspitze, a very cold climate, finds much less deviation, and the simulations are similar until $\sim$200 days. This is likely due to the significantly slower diffusion rate in this climate. The line of best fit is shown in Figure 4.14 to highlight the general trend, but it is not to suggest that the relationship is linear. More data and simulations are required to suggest a mathematical relationship.

Table 4.5: Statistical value MAD for different climates. Note that the unit of the MAD is related to the RMC.

	Gran Canaria	Almeria	LA	Oslo	Zugspitze
MAD (%)	6.64	5.24	5.67	4.35	1.34
Mean annual temperature (K)	294.04	291.92	290.13	280.14	268.88

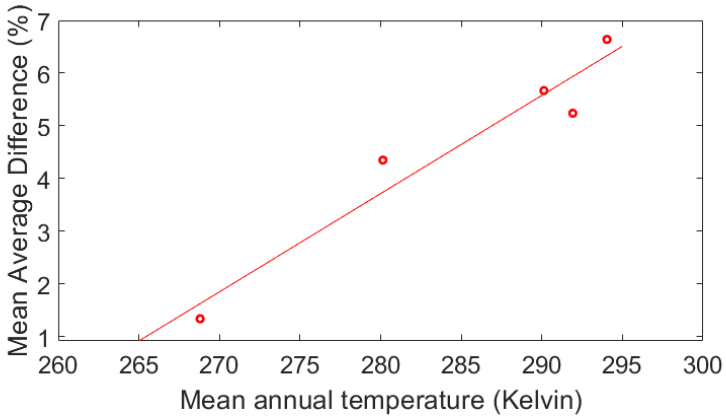

Figure 4.14: A plot of the mean annual temperature and the Mean Annual Difference (MAD) for (non-)Fickian diffusion simulations. The MAD between the Fickian and non-Fickian diffusion simulations increases with increasing mean annual temperature.

4.2.3. Discussion of non-Fickian diffusion in various materials and climates

Non-Fickian diffusion was simulated with different PV materials and climates using the alternative model, as computational limitations meant it could not successfully be applied to the moisture ingress model. The parameters given by Mitterhofer et al. were used to simulated non-Fickian diffusion through EVA, TPO, POE, and ionomer at 50 °C for 200 hours. The results found that TPO deviated the least from Fickian diffusion, whereas ionomer strongly deviated. However, a larger channel share, S_c, was used for TPO, POE, and ionomer than was found to be optimal in literature; this means that the bulk, which has a lower diffusion coefficient, should have a greater share of the material, resulting in slower diffusion overall. Therefore, stronger deviation from the Fickian simulation for TPO, POE, and ionomer is expected, demonstrating stronger non-Fickian diffusion.

These simulations gave a preliminary understanding of how the encapsulant materials behave. EVA, TPO, and ionomer were then simulated under realistic-operation conditions in Delft for 1 month. The time-frame was due to computational limitations, so these simulations gave an insight into initial moisture ingress in these materials. The concentrations profiles clearly show the diffusion through the channels, with diffusion occurring fastest through the EVA, and slowest through the ionomer. However, it should be noted that these simulations used the optimal value, α, found by Mitterhofer et al. This value was found at 50 °C in accelerated tests which may not be suitable for realistic-operation simulations. Longer simulations with realistic-operation experiments could validate this approach.

To simulate non-Fickian diffusion in different climates, an EVA encapsulant and PET backsheet were used. The simulations were run for 1 year due to computational limitations. The simulations show the RMC for both diffusions increasing in a similar trend, but the deviation between the RMC for both increases over the time period. To assess the deviation, the Mean Average Difference (MAD) was calculated; it indicated that moisture ingress simulated with non-Fickian diffusion is slower in warmer climates than in colder climates and that the deviation between Fickian and non-Fickian diffusion increases with increasing temperature. Given the diffusion's dependence on temperature (Equation 2.1), the result is unsurprising, but it highlights the importance of obtaining more field data and more investigation into non-Fickian diffusion.

Furthermore, as Gran Canaria is an example of a tropical climate, and LA a temperate one, it is expected that LA would see slower moisture ingress than Gran Canaria, as the higher temperature in Gran Canaria should drive the diffusion. Figure 4.9, Figure 4.10, and Figure 4.11 appear to have a very similar rates of moisture ingress, which could be attributed to more similar temperatures (the locations could sit on the low and high thresholds of the classifications), or it could be due to the simplicity of the simulated sample. Furthermore, the amplitude of the RMC for these locations is much greater than for Oslo and Zugspitze; this is likely due to larger daily temperature variations in the warmer locations.

4.3. Material ageing and degradation

Section 3.2 explored the degradation of EVA encapsulants and PET backsheets under accelerated tests. This section uses the findings to propose a means of simulating PV material ageing for various materials. The simulations are performed on the model that was optimised in section 2.3.

The relationship between accelerated tests to realistic-operation must first be understood to transform the degradation factor for accelerated tests, γ. The acceleration factor, A_f, is defined as the ratio between the degradation or failure rate during accelerated ageing to that of field use [155]:

$$A_f = \frac{t_{\text{field}}}{t_{\text{test}}}, \tag{4.2}$$

where t_{field} is the exposure time under normal conditions and t_{test} is the testing time during accelerated ageing [156]. The Arrhenius equation, described in Equation 1.4, relates the rate of a reaction to temperature; the acceleration factor is based on the Arrhenius equation to describe the degradation rate at two different temperatures (K) [157]:

$$A_f = \exp\left(\frac{E_a}{R}\left(\frac{1}{T_{\text{field}}} - \frac{1}{T_{\text{test}}}\right)\right). \tag{4.3}$$

Assuming the activation energy, E_a, of failure modes associated with moisture ingress is 0.7 eV and Boltzmann's constant, R, is 8.62$\times10^{-5}$ eV/K, the IEC 61215 damp heat test (85 °C, 85% RH for 1000 hours) corresponds to a field time of 17.4 years [31]. The relation finds that an accelerated test at a temperature of 50 °C for 200 hours, the conditions used by Kyranaki, an gives acceleration factor, A_f, of approximately 13, which then corresponds to approximately 109 days. The calculation can be found in section C.1. While this approach is limited in only considering temperature, it is used here to determine appropriate moisture parameters for the realistic-operation analysis. Figure C.1 shows the experimental data from Kyranaki and the Fickian simulation with no degradation under the accelerated test (50 °C for 200 hours), along with a realistic-operation simulation (20 °C for 100 days). The realistic-operation simulation uses the parameters outlined in Table 4.4, but with different PET backsheet coefficients ($D_{0,\text{PET}}$ = 5.1$\times10^{-7}$ m^2/s and $E_{a,D,\text{PET}}$ = 35200 J/mol/K [154]) as this better replicates the accelerated test. Scaling the saturation concentration determined by Kyranaki at 20 °C, the solubility of the encapsulant at 20 °C is calculated to be 2.13 kg/m^3.

In chapter 3, an approximate degradation factor γ was determined for EVA and PET under accelerated tests (γ_{EVA} = 0.04 and γ_{PET} = 0.004). Despite the limitations of the approach outlined in subsection 3.2.1, it is used in this section to explore the possible effect on moisture ingress. This degradation factor is unsuitable for realistic-operation modelling of material degradation, so a new degradation constant, β was identified. This constant was estimated by dividing the values of γ by the acceleration factor, A_f, which was found to be approximately 13 in this scenario, and accounting for the change in time:

$$\beta = \frac{\gamma}{A_f}. \tag{4.4}$$

This gives realistic-operation degradation constants of $\beta_{\text{EVA}} = 0.0015$ and $\beta_{\text{PET}} = 0.00015$. Applying this to the aforementioned parameters and conditions for the realistic-operation simulation, the pink line in Figure 4.15 is found. Unsurprisingly, there is hardly a change in RMC compared to the simulation without degradation. In 100 days, PV modules should not have any noticeable degradation. As there is insufficient experimental data to propose an alternative approach, the chapter will proceed with the realistic-operation degradation factors $\beta_{\text{EVA}} = 0.0015$ and $\beta_{\text{PET}} = 0.00015$ to explore the effect on moisture ingress.

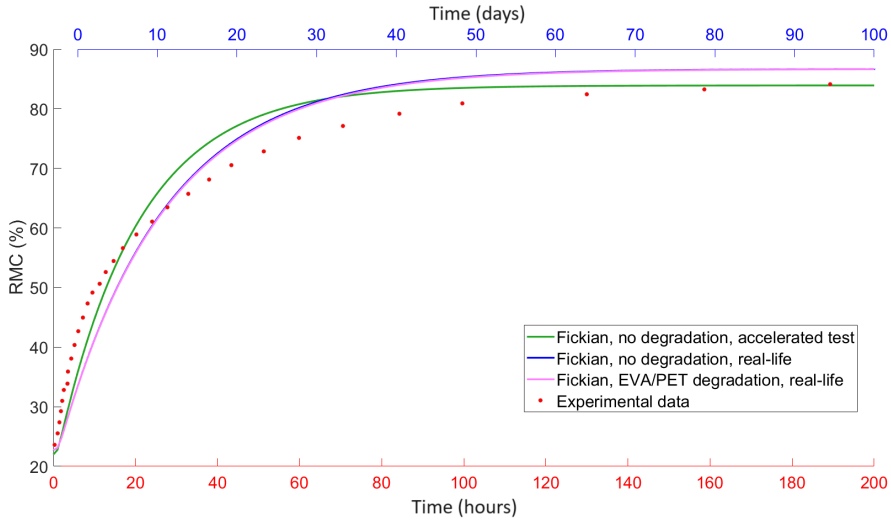

Figure 4.15: Realistic-operation comparison with degradation. The red x-axis corresponds to the experimental data and Fickian simulation under accelerated test (red points, green line), and the blue x-axis correspond to the realistic-operation degradation and no degradation simulations (pink and blue lines). The realistic-operation simulation with the degradation constant has negligible deviation from the simulation without degradation.

4.3.1. Material ageing and degradation in different PV materials

The degradation of several encapsulant and backsheet materials is explored, the moisture parameters of which are outlined in Table 4.3 and Table 4.6, respectively. When the encapsulant is varied, a PET backsheet is used, and when the backsheet is varied, an EVA encapsulant is used.

Table 4.6: Moisture parameters for different backsheet materials [101].

Parameter	PET	TPT	PA
D_0 (m^2/s)	6.02×10^{-6}	5.97×10^{-7}	2.27×10^{-3}
$E_{a,D}$ (kJ/mol/K)	39.16	33.11	53.94
S_0 (g/m^3)	7.08×10^{9}	3.03×10^{10}	2.98×10^{9}
$E_{a,S}$ (kJ/mol/K)	43.17	44.82	41.59

The realistic-operation degradation constant, β, for each material was estimated by considering the properties of each material, outlined in subsection 4.1.1, specifically their WVTR. This assumption was made as Peike et al. observed a clear correlation between the permeation properties of PV materials and the aging behaviour [149]. TPO was reported to have a WVTR 7 times lower than EVA, so the value for β was scaled accordingly. Similarly, based on the WVTRs reported by Li, the other materials were scaled. TPT was reported to have a very similar WTRV as PET, so they share the same degradation constant.

Table 4.7: realistic-operation degradation constants for different PV materials, assumed based on their WVTR and comparison with EVA and PET.

	EVA	TPO	Ionomer	PET	TPT	PA
β_i	0.0015	0.000214	0.000071	0.00015	0.00015	0.0003

Based on the work in chapter 3, Equation 3.7 is adapted to give the following:

$$D_i = D_0 \exp\left(-\frac{E_{a,i}}{R \cdot T} - \beta_i \cdot t \right), \tag{4.5}$$

where i denotes the material and t is the time. Each material was simulated in the original model, with and without the degradation constant, in Delft for 20 years.

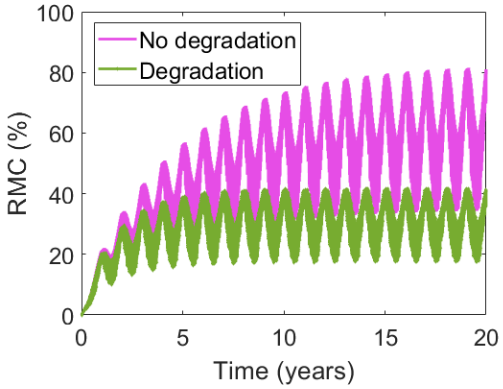

Figure 4.16: Average RMC in the EVA encapsulant in RMC after 20 years in Delft, simulating no material degradation and material degradation in the EVA encapsulant and the PET backsheet. The limiting constant makes the simulation unrealistic.

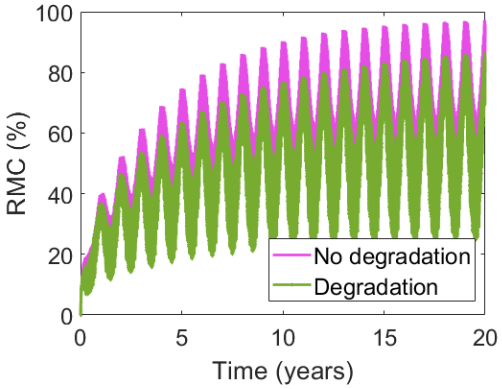

Figure 4.17: Average RMC in the TPO encapsulant in RMC after 20 years in Delft, simulating no material degradation and material degradation in the TPO encapsulant and the PET backsheet. Some degradation over the 20 years is observed.

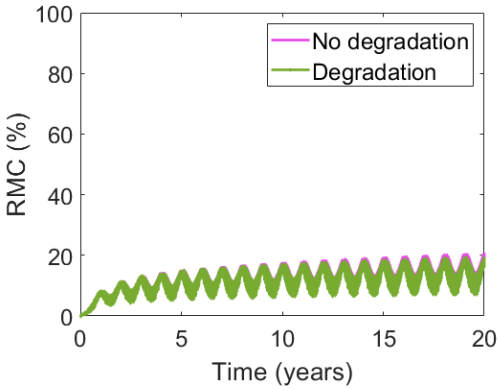

Figure 4.18: Average RMC in the ionomer encapsulant in RMC after 20 years in Delft, simulating no material degradation and material degradation in the ionomer encapsulant and the PET backsheet. Very little degradation over the 20 years is observed.

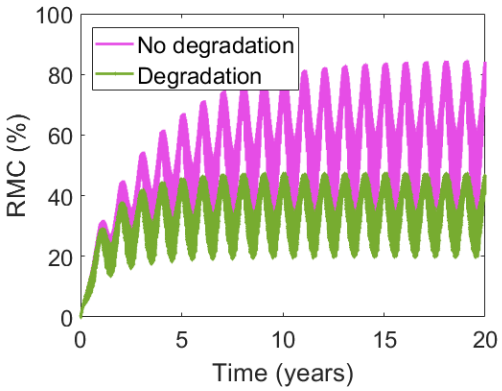

Figure 4.19: Average RMC in the EVA encapsulant in RMC after 20 years in Delft, simulating no material degradation and material degradation in the EVA encapsulant and the TPT backsheet. The limiting constant makes the simulation unrealistic.

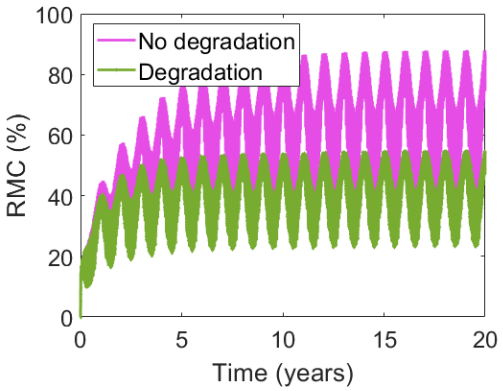

Figure 4.20: Average RMC in the EVA encapsulant in RMC after 20 years in Delft, simulating no material degradation and material degradation in the EVA encapsulant and the PA backsheet. The limiting constant makes the simulation unrealistic.

Figure 4.16 - Figure 4.20 show the results of the simulations. It can be seen that this approach strongly limits the diffusion coefficient in the case of EVA/PET, EVA/TPT, EVA/PA. As it is the common factor in each scenario, this indicates that β_{EVA} is insufficient. However, in the cases of TPO/PET shows some degradation, and the ionomer/PET shows very little degradation; this aligns with the material properties outlined in subsection 4.1.1.

Even without degradation, TPO reaches the highest RMC (94.5%) in the 20 year period without degradation, indicating its poor suitability in this climate. Conversely, ionomer peaks at only 19% RMC, highlighting its low permittivity and low diffusivity.

4.3.2. Material ageing and degradation in different climates

To investigate how simulated material degradation may vary in various climates, simulations of moisture ingress through an EVA encapsulant and a PET backsheet were performed in Gran Canaria, Almeria, LA, Oslo, and Zugspitze both with and without the proposed degradation constants, β. The results can be seen in section D.1. Each degradation simulation exhibits similar behaviour: the degradation constant limits the diffusion coefficient, which in turn limits the diffusion of moisture through the encapsulant. Consequently, the moisture content in the encapsulant saturates faster and at a lower concentration. This result is coherent with the findings in subsection 4.2.1, that the determined value for β_{EVA} limits the simulated diffusion. For all locations, the degradation simulation appears to saturate around an RMC value half that of the simulation without degradation.

Instead, simulations of moisture ingress through a TPO encapsulant and a PET backsheet in different locations were performed, as they showed more promising results in the previous section. The profiles over 20 years are shown, but the deviation is so small that it is not visible on the plots. Next to each figure is a zoomed-in snapshot at around 15.5 years to highlight the deviation in the simulations. Attempts were made to represent the data better, so the RMC over 20 years with a time-step of 12 hours is plotted in section D.2. In Gran Canaria, Almeria, and Oslo, it can be seen that the non-degradation simulation initially allows more moisture ingress, until around 10 years, after which the degradation simulation has a higher RMC in the winter months. However, in LA, the non-degradation simulation consistently allows more moisture ingress, except for a short period in winter. Zugspitze finds the degradation simulation to allow slightly more moisture ingress in winter, while the non-degradation simulation allows more in summer months.

The MAD is calculated to grasp the effect the degradation simulations have in different climates, summarised in Table 4.8. It appears that material degradation is stronger in colder climates, although more investigation into different locations is needed.

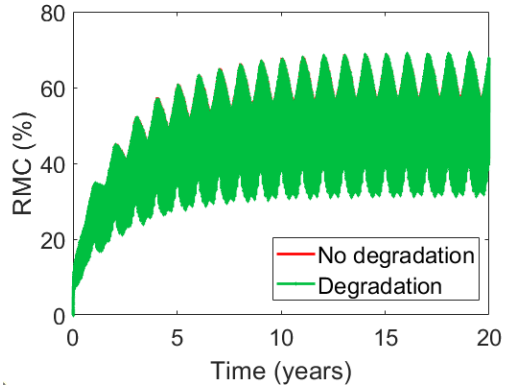

Figure 4.21: Average RMC in the TPO encapsulant in Gran Canaria after 20 years, simulating no material degradation and material degradation. Negligible degradation can be seen.

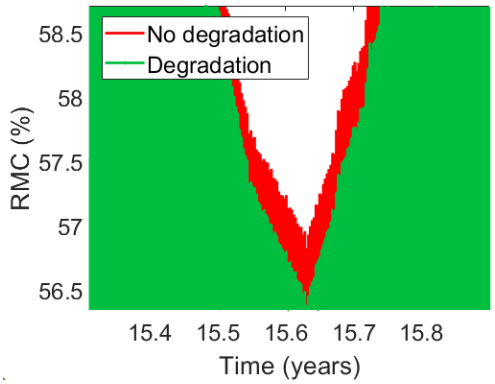

Figure 4.22: Average RMC in the TPO encapsulant in Gran Canaria around 15.5 years, simulating no material degradation and material degradation. The deviation between simulations can be seen.

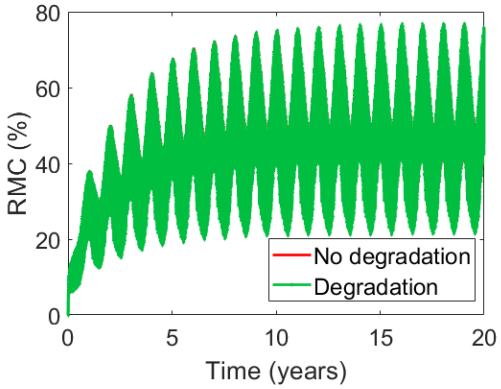

Figure 4.23: Average RMC in the TPO encapsulant in Almeria after 20 years, simulating no material degradation and material degradation. Negligible degradation can be seen.

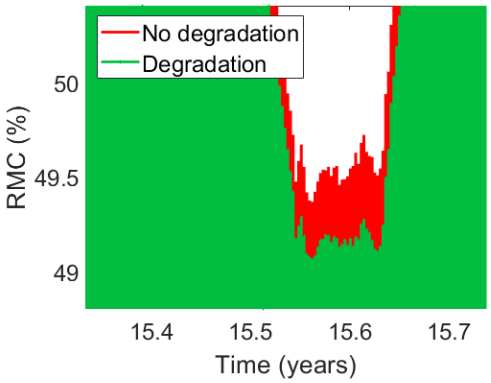

Figure 4.24: Average RMC in the TPO encapsulant in Almeria around 15.5 years, simulating no material degradation and material degradation. The deviation between simulations can be seen.

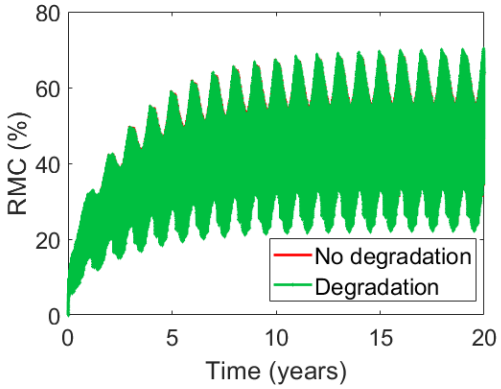

Figure 4.25: Average RMC in the TPO encapsulant in LA after 20 years, simulating no material degradation and material degradation. Negligible degradation can be seen.

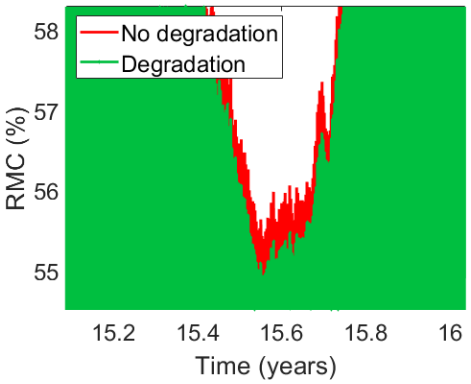

Figure 4.26: Average RMC in the TPO encapsulant in LA around 15.5 years, simulating no material degradation and material degradation. The deviation between simulations can be seen.

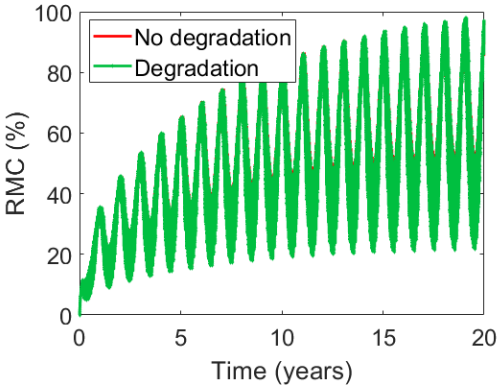

Figure 4.27: Average RMC in the TPO encapsulant in Oslo after 20 years, simulating no material degradation and material degradation. Negligible degradation can be seen. The deviation between simulations can be seen.

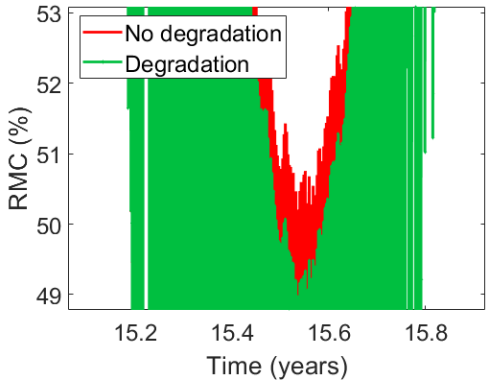

Figure 4.28: Average RMC in the TPO encapsulant in Oslo around 15.5 years, simulating no material degradation and material degradation. The deviation between simulations can be seen.

The zoomed-in profiles show the difference between the normal the degradation simulations at around 15.5 years; it is around halfway through the year that the highest difference can be observed. All chosen locations are in the northern hemisphere, so this is during the summer months.

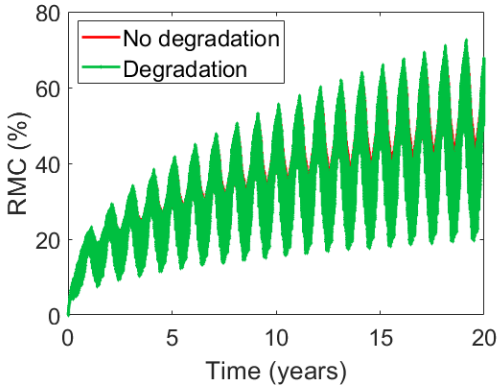

Figure 4.29: Average RMC in the TPO encapsulant in Zugspitze after 20 years, simulating no material degradation and material degradation. Negligible degradation can be seen.

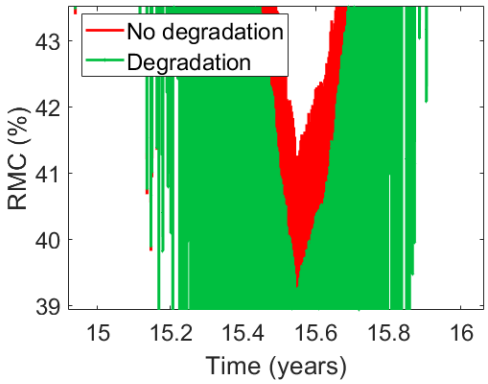

Figure 4.30: Average RMC in the TPO encapsulant in Zugspitze around 15.5 years, simulating no material degradation and material degradation. The deviation between simulations can be seen.

Table 4.8: Statistical value MAD for different climates. Note that the unit of the MAD is related to the RMC.

	Gran Canaria	Almeria	LA	Oslo	Zugspitze
MAD (%)	0.20	0.18	0.22	0.41	0.51

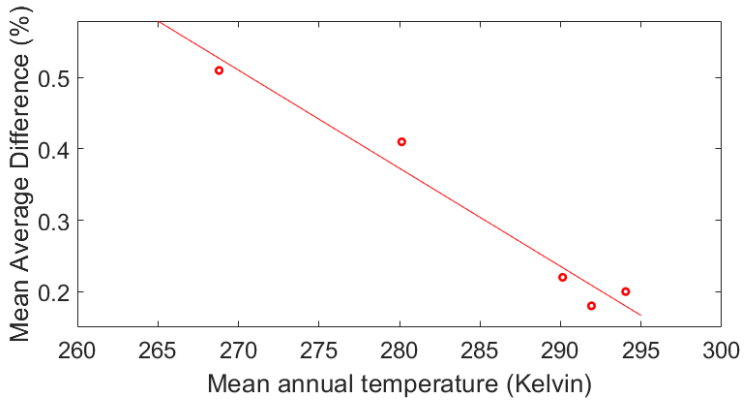

Figure 4.31: A plot of the mean annual temperature and the Mean Annual Difference (MAD) for material degradation simulations. The MAD between the degradation and non-degradation simulations decreases with increasing mean annual temperature.

4.3.3. Discussion of material ageing and degradation in various materials and climates

To explore material ageing and degradation, the findings from section 3.2 had to be converted from acceleration test to realistic-operation. This was done using a proposed acceleration factor, A_f, which related the temperature of the accelerated test and typical field temperature. While this conversion appeared to be suitable, given the conversion of the IEC 61215 damp heat test, it did not consider the relative humidity of the test and the field. Kempe et al. proposed a degradation rate formula for PET, based on temperature and relative humidity [98]; incorporating RH in Equation 4.3 using a similar approach could give a more accurate acceleration factor. It would increase A_f used in this study by a factor of 1.2 - 5, depending on the location. If the acceleration factor were to increase 5-fold, it would equal 65 using this approach. Finding a more accurate acceleration factor would improve the conversion of the degradation factor.

The degradation factors determined for EVA and PET under accelerated tests had limitations, as discussed in subsection 3.2.1. However, the approach was still used in this chapter as other experimental data was unavailable. After applying the acceleration factor and accounting for the change in time-step, realistic-operation degradation constants, β, were proposed for EVA, TPO, ionomer, PET, TPT, and PA, considering the water vapour transmission rates (WVTRs). The simulations of the EVA/PET, EVA/TPT, EVA/PA samples found that the approach limited moisture ingress, meaning the RMC for the simulations with degradation saturated quickly. These cases all use EVA in their simulations, thus it can be deduced that EVA and its degradation constant are the limiting factor. However, the TPO/PET and ionomer/PET simulations results that align with expectations: ionomer/PET hardly deviates from the simulation with no degradation, and TPO/PET deviates somewhat.

Similarly for the simulation of degradation in different climates, which initially used an EVA encapsulant and a PET backsheet, the diffusion of moisture was limited, so the RMC of each degradation simulation is about half that of the simulation without degradation. As this provided no insight into how material degradation varies in different climates, a TPO encapsulant and a PET backsheet were instead simulated. Negligible degradation was observed over the 20 year period, with the highest difference in RMC occurring in the summer months. The same data with a 12 hours time period was plotted, but no correlation between climatic features and degradation trends could be deduced. The MAD indicated that the difference between the material degradation and non-degradation simulations increases in colder climates. This is the opposite of PV module degradation: modules have been found to degrade more in warmer climates [46]. More investigation into how different materials behave in different climates could help consumer choices.

As mentioned in subsection 3.2.1, when a material degrades, the material composition changes and by-products may be produced. This process may increase diffusion, as the material becomes more porous, or may decrease diffusion, as the products pose as a barrier to the moisture. There is insufficient literature to conclude how each material degrades and what the effect on the moisture parameters is. The approach used in this and the preceding chapter was based on one set of experimental results; more research into the material science and experimental data is needed to assess the degradation approach used in this thesis. Additionally, a change in material composition would expect a change in the solubility of a material. This was not explored in this thesis, nor has any literature been found for PV materials, but it would be an interesting area of further research.

4.4. Conclusion

The goal of this chapter was to gain insight into how the dual-transport method, used to simulate non-Fickian diffusion, differed in different PV material and climates, how material ageing of different materials might be simulated and how degradation may change in different climates. It was found that non-Fickian diffusion through ionomer is slower than through EVA, TPO, and POE under accelerated tests, which was confirmed through simulations in Delft. The findings were in agreement with the theoretical background, but more experimental data is required to confirm that these materials exhibit non-Fickian diffusion in this way. An EVA/PET stack was used in non-Fickian simulations in different climates. For all climates, the Fickian and non-Fickian simulations showed similar trends, with the difference in moisture ingress increasing over the year. Statistical analysis indicates that non-Fickian diffusion is slower compared to Fickian diffusion in warmer climates.

An acceleration factor was determined, which relates accelerated and realistic-operation tests, to convert the accelerated test degradation constants, γ, found in section 3.2. Based on the realistic-operation degradation constants for EVA and PET, and some material properties, particularly the water vapour transmission rate (WVTR), realistic-operation degradation constants were found for TPO, ionomer, TPT, and PA. Simulations over 20 years in Delft concluded that the constant used for EVA limited the moisture diffusion in the cases that used EVA, but the TPO/PET and ionomer/PET simulations showed promising results. Consequently, simulations using TPO and PET were performed, although negligible degradation of the TPO was observed over the 20 years. Statistical analysis suggests that material degradation is stronger in colder climates, although field data is required to confirm this hypothesis.

5

Monitoring of Moisture Ingress in PV Modules

Monitoring moisture ingress in PV modules through experiments can verify the accuracy of a model. This chapter details the various methods of measuring moisture ingress and results from literature thus far in section 5.1, from which an experimental methodology is devised in section 5.2. Due to equipment and time constraints, the experiment could not be performed in the time-frame of this thesis, but is detailed for potential future use.

5.1. Measurement of moisture ingress in PV modules

Various experiments have been performed to measure moisture ingress in PV modules, in laboratories and the external environment. Detailed below are some relevant experiments.

Kempe et al. evaluated the performance of a typical edge-seal material (polyisobutylene (PIB) resin filled with desiccant) and encapsulant materials (EVA, ionomer, PDMS, TPU, PIB, PVB) by using an optical method that detected a reaction of calcium (Ca) film with water [153]. This method was proposed because Ca reacts quickly with water, compared to oxygen [158], and because oxygen is soluble in most polymers, it is thought that oxygen plays little role in the oxidation of Ca. Over time, the reaction turns the mirror-like layer into a transparent film that makes it simple to see where moisture intrusion has occurred. Additionally, they determined the diffusivity and solubility of the encapsulant materials using a water vapour transmission rate (WVTR) testing system. The test samples were exposed to different conditions in the accelerated tests (85°C, 85% RH and 45°C, 85% RH) for over 3000 hours. It was found that the desiccant-filled PIB materials were the best low-diffusivity encapsulants. A drawback of the Ca film technique is that only a visual evaluation can be made, and the amount of moisture ingress cannot be quantified.

Instead, Jankovec et al. used SHT25 digital humidity sensors to monitor moisture ingress in PV modules [159]. Three different EVA stacks (EVA/EVA, glass/EVA/backsheet, and glass/EVA/glass) were subject to damp heat conditions (85°C, 85% RH) for 100 hours. The sensors were mounted on a strip of printed circuit board (PCB) based on an FR-4 core material, which is an epoxy resin material reinforced by eight layers of glass fibre cloth, covered by 35 μm-thick copper foil on both sides. The lamination of the samples was successful, and the sensors performed well in the extreme conditions. The experiment finds the WVRT of the backsheet and the moisture diffusion coefficient of the EVA. Following this success, Jankovec et al. performed long-term (>6500 hours) monitoring tests using digital humidity sensors with different encapsulants (EVA, TPO, POE, and ionomer) [145]. Three EVA samples were tested, each from a different manufacturer. Samples were exposed to 50°C and preconditioned at 10% RH, then the ambient RH was varied stepwise, and the RH data was taken at each minute. Ionomer was found to have the lowest diffusion coefficient at 50°C, indicating it is the least permeable.

The new technique using digital humidity sensors proposed by Jankovec et al. has been adopted in numerous studies in the last 5 years. Slapšak et al. built on this technique, using wireless radio-frequency identification (RFID) technology to read measurements from the digital RH sensors [160]. They can be installed anywhere in the PV module, either in front or behind the solar cells, due to their ultra-small size and wireless design. The EVA minimodules were exposed to elevated conditions (40°C, 85% RH and 50°C, 70% RH) and the study found the acquired data was in agreement with 2D simulations. Additionally, Wisniewski et al. tested moisture ingress through a double-glass EVA module, first acquiring WVTR values, and verifying the parameters using humidity sensors (SHT25) [102].

While most approaches use climatic chambers to test modules against weather stressors and monitor moisture ingress, Mitterhofer et al. used sensors in five setups in different climatic regions around the world to obtain real-life data [161]. Because it is challenging to measure the moisture inside the modules in such conditions, experimental measurements in the field under continuously changing conditions is currently lacking. In each location, three PV minimodules are deployed: two with an EVA encapsulant, of which one has a PPE (PET-PET-EVA) backsheet, the other has a TPT (Tedlar-PET-Tedlar) backsheet, and a third with a TPO encapsulant. The TPO sample was disregarded as insufficient adhesion in the lamination stage made it more vulnerable to moisture ingress. Temperature and humidity sensors (SHTW2) were encapsulated in the modules and read a measurement every five minutes. The study finds that the typical approach to 2D moisture ingress simulation is flawed, and develops an technique that better simulates Fickian diffusion in the horizontal and vertical cross-section. Electroluminescence (EL) imaging before and after lamination revealed cell cracks, highlighting a drawback of using uncontrolled conditions: the additional stress factors can damage the samples, leading to more moisture diffusion pathways.

To describe how temperature affects moisture diffusion through EVA, an in-situ gravimetric method was used by Dadaniya and Datla [99]. They assumed one-dimensional Fickian moisture diffusion, and obtained the diffusion coefficient from the following equation [162]:

$$\frac{M_t}{M_\infty} = 1 - \frac{8}{\pi^2} \sum_{n=0}^{n=\infty} \frac{1}{(2n+1)^2} e^{-D(2n+1)^2 \pi^2 t / l^2}, \tag{5.1}$$

where M_t is the total mass uptake of water at time t, M_∞ is the saturated fractional mass uptake, l is the thickness of the dry sample. From Equation 5.1, D was determined through least square curve fitting with experimental data. A permeation instrument was used to measure the WVTR, which found values in agreement with those determined by the gravimetric method.

5.2. Methodology

This section proposes an experiment to be performed to measure moisture ingress in PV samples. The aim is to compare the measured moisture ingress to the COMSOL simulations to verify the findings in chapter 3 and 4.

5.2.1. Humidity sensors

Two different types of humidity sensors, based on different measuring principles, are proposed to compare and validate the measurements.

Sensirion SHT41 humidity sensor

The Sensirion SHT41 sensor is a capacitive humidity sensor. Previous experiments have typically used the SHT25 and SHTW2 sensors from Sensirion; however, the SHT41 sensor has better voltage compatibility. Capacitive humidity sensors dominate the market due to their low power consumption and high output signals. Moisture-induced changes in a hygroscopic layer's dielectric constant are detected to determine the relative humidity (RH) [78]. This displacement phenomenon is the essential difference from other sensors and results in its unique properties. The basic structure of a capacitive sensor always consists of a set of plates of surface A separated by a distance d. The following relation determines the value for the capacitance:

$$C_0 = \epsilon\left(\frac{A}{d}\right), \tag{5.2}$$

where ϵ is the dielectric constant (permittivity) of the medium between the plates (usually air) [163]. A general schematic can be seen in Figure 5.1.

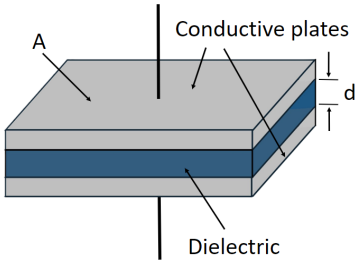

Figure 5.1: A schematic of a capacitor, consisting of two plates with area A, and a dielectric with thickness d.

The sensor element in humidity sensors is a capacitor with a polymer as its dielectric. Water is absorbed or released according to the relative humidity of the surrounding air. An electrical circuit can be used to measure the capacitance of the capacitor as a result of the change in the dielectric constant.

The Sensirion sensor can be seen in Figure 5.2, with the sensor element facing upward. The drawing that is used in to represent the sensor is shown in Figure 5.3, with the sensor element represented by the yellow circle, the pins the yellow rectangles, and the dimensions of the sensor package (LxWxH = 1.5×1.5×0.5 mm^3). The typical relative humidity measurement uncertainty is ±1.8% RH in an operating range of 30 - 70% RH and ±2% RH in the range 0 - 30% and 70 - 100%. The sensor shows best performance when operated within the temperature and humidity range of 5 - 60 °C and 20 - 80% RH, respectively.

Figure 5.2: Sensirion SHT41 humidity sensor [164].

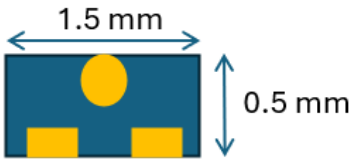

Figure 5.3: Drawing of the Sensirion humidity sensor.

The sensor uses 4 pins to function: (1) data line to send data; (2) clock line to time data transfer; (3) voltage supply; (4) grounding line. The respective pins are annotated in Figure 5.4. The dimensions of the pins with respect to the sensor package is shown in Figure 5.5.

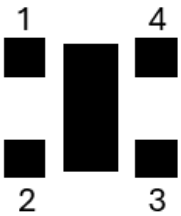

Figure 5.4: Location of the Sensirion pins.

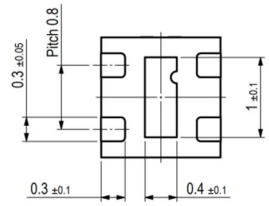

Figure 5.5: Dimensions of the Sensirion pins [164].

RS PRO humidity sensor

The RS Pro sensor is a 2-pin resistive humidity sensor; it measures changes in a material's electrical resistance in response to humidity changes. The electrical current flowing through the sensor increases as a result of the polymer film swelling, becoming more conductive when it collects water vapour from the air. The amount of water vapour changes is proportional to this change in resistance. The sensor has positive (anode) and negative (cathode) pins; the voltage is applied to the formed, while the latter is connected to the ground.

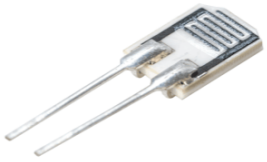

Figure 5.6: RS PRO humidity sensor [165].

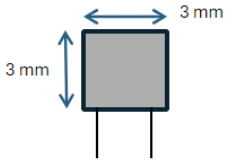

Figure 5.7: Drawing of the RS humidity sensor.

Figure 5.6 shows the actual sensor, and Figure 5.7 the drawing used to represent the sensor. The operating temperature range of this sensor, 0-50 °C limits the temperature used in the accelerated test. It can operate between 20 and 95% RH.

Both sensors can be calibrated by placing the sensors in the chamber at several different temperatures and RH (e.g. 40 °C, 60 °C, 85 °C and 40%, 60%, 85% RH) for 2 hours; the hour allows time for stabilisation, and during the second hour the measurement is taken. To test and evaluate the performance of the sensors in laminated samples, they would be laminated between two sheets of EVA and placed in the climate chamber to assess their suitability for measurements in the samples.

5.2.2. Sensor strips

For each sensor, a custom sensor strip was designed on a printed circuit board (PCB) to support 8 equally spaced sensors. Each strip is the same length, but the distance between the sensors varies due to the Sensirion and RS sensors being different sizes. The strip is centred such that the sensor element of each aligns; this allows the measurements to be compared.

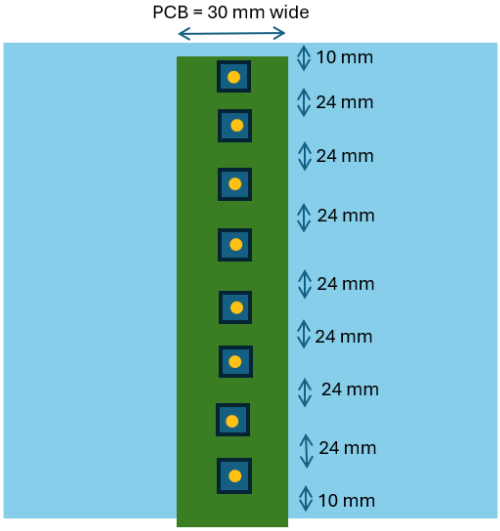

Figure 5.8: Top view of a PV sample with Sensirion humidity sensors on a sensor strip.

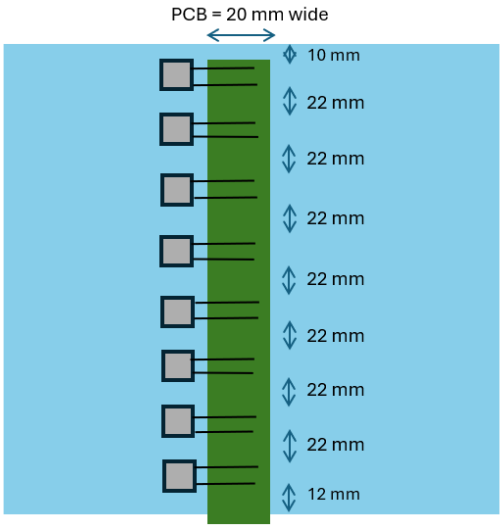

Figure 5.9: Top view of a PV sample with RS humidity sensors on a sensor strip.

The PCB design for the Sensirion sensor (Figure 5.10) must account for the sensors' 4 pins. Consequently, the PCB strip is wider, 30 mm. The yellow lines indicate the serial data (SDA) lines that transmits data from the sensor, while the dark blue lines illustrate the the serial clock (SCL) line, which synchronises the data transfer. All SDA lines come together and connect to the SDA pin of a microcontroller. Similarly, all SCL pins tie together and connect to the microcontroller's SCL pin. The light blue line and the red line highlight the supply voltage and the ground, respectively.

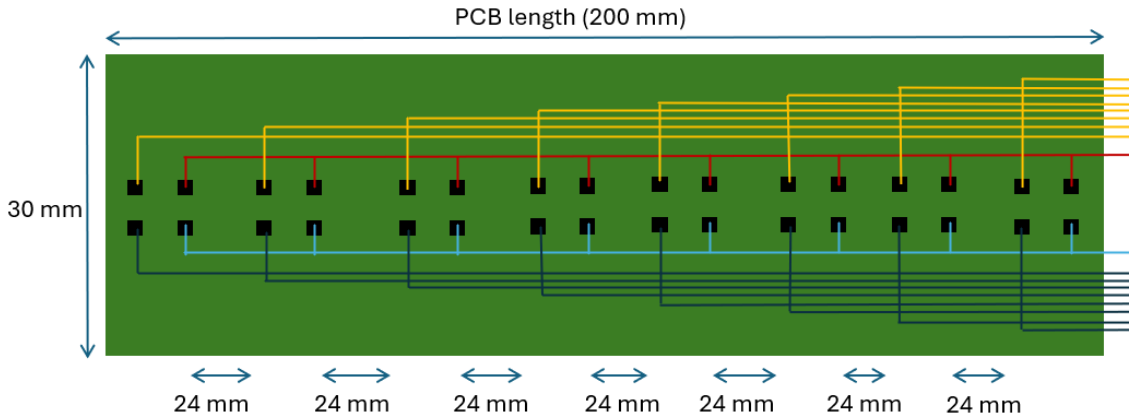

Figure 5.10: PCB design for the Sensirion humidity sensors. The lines indicate the wires: serial data (SDA), bidirection (yellow); serial clock (SCL), unidirectional (dark blue); supply voltage (light blue); ground (red).

The microcontroller communicates with each sensor using I2C protocol. The I2C bus allows the sensors to be addressed individually as each device has a unique address. More information on the data acquisition can be found in section E.1.

The RS sensor only has 2 pins, so fewer wires are required and the designed PCB (Figure 5.11) is smaller in width. Similar to the previous PCB, the ground line is shown in red, where the negative pin is connected. Each sensor has its own fixed resistor, which forms a voltage divider with the sensors. The fixed resistor should be of the same magnitude as the sensor; based on Figure E.2, a fixed resistor of 10 kΩ is recommended. A single 5 V power supply is connected to each fixed resistor, shown in light blue.

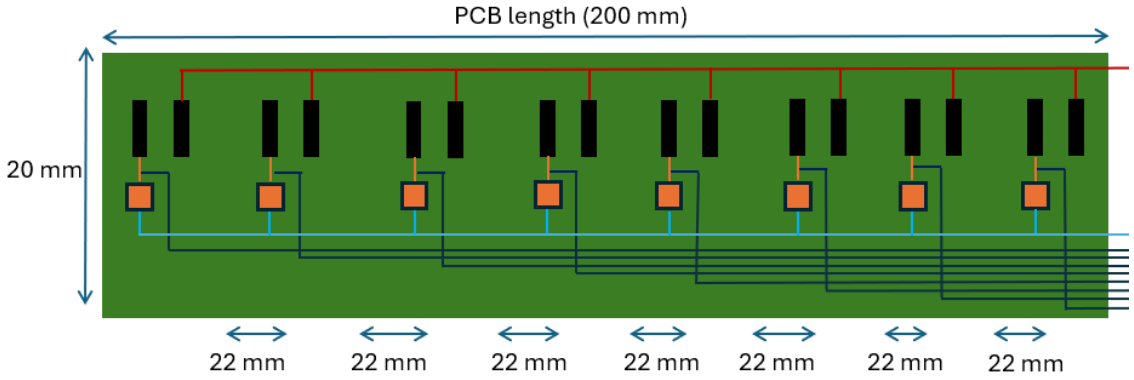

Figure 5.11: PCB design for the RS humidity sensors. The lines indicate the wires: supply voltage (light blue); ground (red); connection between voltage junction and the microcontroller (dark blue). Each sensor is connected to a fixed resistor, depict in orange.

Th voltage at the junction between each resistor and sensor is sent to separate analog-to-digital converter (ADC) inputs on a microcontroller, indicated by the dark blue lines. The microcontrollers reads each output voltage and converts it to digital values, from which each sensors' resistance can be calculates, which can then be converted to RH using a humidity curve, as demonstrated in Figure E.2.

5.2.3. PV Samples

The PV samples were designed such that they complimented the design of the model. The dimensions of all samples are 200 mm $\times$ 200 mm, each with a backsheet thickness of 0.38 mm and each encapsulant layer has a thickness of 0.725 mm. These thickness correspond to the dimensions of the original moisture ingress model and can be changed to correspond with the chosen materials. Between the encapsulant layers sits a layer of silicon to mimic PV module design. The sensor strips with the humidity sensors sit on the silicon layer and measure the moisture content in the top encapsulant layer. The laminated samples are framed in an aluminium frame on three sides, and the fourth is closed with aluminium so the sensor strip can exit the sample and be reachable by the readout electronics outside.

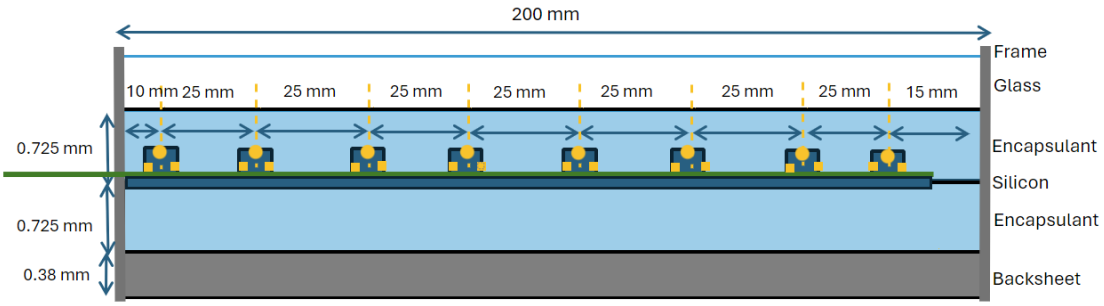

Figure 5.12: Side view of a PV sample with Sensirion humidity sensors.

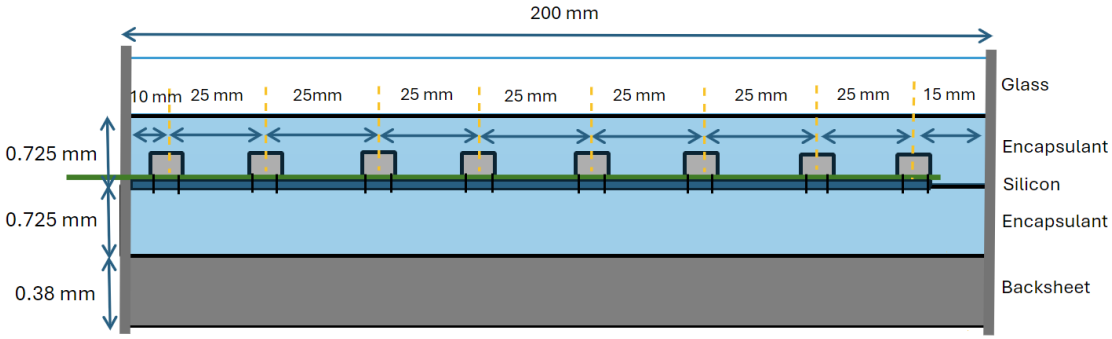

Figure 5.13: Side view of a PV sample with RS humidity sensors.

Various PV materials would be investigated: EVA, TPO, and ionomer encapsulants, and PET, TPT, and PA backsheets. Like the simulations in chapter 4, the following stacks would be made: EVA/PET, TPO/PET, ionomer/PET, EVA/TPT, and EVA/PA. As there are five material combinations to be tested, and each combination will be tested with both sensors, there are ten samples to be tested.

5.2.4. Experiment

The purpose of the experiment is to measure moisture ingress in PV samples of different PV materials. The results would provide more insight into how moisture diffuses through the materials; specifically, the data could provide support for the findings in chapter 3 and chapter 4, or show deviation.

After calibrating the sensors and laminating the samples, they would be put in a climate chamber at 85 °C, 85% RH for 2000 hours, the standard test outlined by the IEC. Measurements would be taken every hour to observe the general trend of the moisture ingress.

Experiments that are performed to determine moisture parameters typically do so by assuming diffusion is Fickian and fitting the parameters, or by using gravimetric methods. The latter can be very complicated and is out of the scope of this thesis. As one hypothesis in this thesis is that diffusion through encapsulant materials is non-Fickian, the former method is also not appropriate. Therefore,

the approach will use moisture parameters from literature and focus on corroborating the experimental results with the simulations.

5.3. Discussion

This section outlines some potential problems that could arise in the preparation of or during the experiment.

Firstly, there are concerns about deforming the top encapsulant layer. As the sensors are 0.5mm thick, the top encapsulant layer is not placed on a flat surface, rather a (rough) one. This may change the material structure of the top encapsulant, and hence its material properties. This could be overcome by cutting strips to the gaps between the sensors so that the top encapsulant is laminated on a flat surface. Alternatively, the sensor strip could sit upside down on top of the top encapsulant to measure the moisture at the top of the flat encapsulant layer.

Furthermore, there are concerns over the ability of TPO and ionomer to adhere to the sensor strips and glass. Mitterhofer et al. observed insufficient adhesion between the sensor strip and the TPO encapsulant, which results in delamination [161]. Furthermore, Tracy et al. found that ionomer's adhesion to the glass and cell interfaces is poor enough that there is potential delamination in short time-frames [143]. Their tests observed delamination between the ionomer and the glass within 6 months of field aging. Delamination makes the samples much more susceptible to moisture ingress.

5.4. Conclusion

This chapter details an experiment that measures moisture ingress in PV samples that could not take place due to equipment and time constraints. The experiment is design to measure moisture ingress through samples of different PV materials, the results of which can then be compared to the simulations performed in chapter 3 and chapter 4, to support or contradict the hypotheses. The experiment would use two sensors, capacitive and resistive, to measure humidity. Connected to PCBs, the measurements can be communicated via microcontrollers. The experiment would be carried out under conditions set out by the IEC (85 °C, 85% RH for 2000 hours) and literature values of the materials' moisture parameters would be used to compare the experimental data to simulations.

6

Conclusions and future work

This chapter concludes the thesis and identifies areas of potential future work.

6.1. Conclusion

This thesis explored moisture ingress in PV modules, specifically looking at more accurate means of simulating it. It was hypothesised that other mechanisms were involved in moisture diffusion in PV materials, and identifying them could better simulate moisture ingress.

Chapter 2 reviewed the moisture ingress model developed by Daniel Jimenez Pelarda, and then optimised the model. It was first confirmed that the Normal mesh used delivered sufficient results by simulating moisture ingress with various meshes and checking if the results converge. Then, the mesh was adapted to reduce the computational time while still giving accurate results.

The model was found to simulate moisture ingress well, but there was deviation between the simulation and the experimental results. Two possible reasons for the discrepancy were proposed and explored in the chapter: moisture diffusion through the materials is actually non-Fickian, and the material degrades over time. Using the dual-transport method to simulate non-Fickian diffusion, it was found to deliver excellent results when applied to EVA, but was found to drastically limit diffusion when applied to PET. It was concluded that the simulation was suitable for EVA but not for PET. Optimal non-Fickian factors of NF: 32 and NF: 40 are found, corresponding to units of dimension $(0.625 \times 0.625) \times 10^{-4}$ m^2 and $(0.5 \times 0.5) \times 10^{-4}$ m^2, respectively. To simulate material degradation, a means was proposed which involved finding a degradation constant for each material under accelerated conditions. Using a statistical analysis, the degradation constants γ_{EVA} = 0.04 and γ_{PET} = 0.005 were found.

Building on this work, chapter 4 investigated different materials and climates under non-Fickian diffusion and using the material degradation approach. Non-Fickian diffusion was simulated through EVA, TPO, POE, and ionomer, finding that the results for ionomer deviated the most from the Fickian simulation. Simulating non-Fickian diffusion through EVA, TPO, and ionomer in Delft confirmed that moisture diffusion through ionomer is slowest, followed by TPO, and EVA showed the fastest diffusion. The simulations of non-Fickian diffusion in different climates suggests that non-Fickian diffusion deviates more from Fickian diffusion in warmer climates than colder. To simulate material aging, an acceleration factor was determined to relate the accelerated test performed by Kyranaki and a typical field environment. Together with material properties, this factor was used to determine real-life degradation constants for EVA, TPO, ionomer, TPT, and PA. Simulating degradation in Delft for 20 years for the materials found that the degradation constant for EVA limited diffusion, delivering unrealistic results. However, the TPO and ionomer simulations gave expected results, with ionomer hardly degrading and TPO seeing some degradation. TPO and PET were used for the climate analysis; minimal degradation was observed over 20 years, but statistical analysis indicated that material degradation is higher in colder climates.

Finally, chapter 5 detailed an experiment that would moisture ingress in PV samples of different materials. The intention was to compare the experimental results to the simulations in chapter 3 and chapter 4 to either support the findings, or to undermine them and identify other mechanisms at play. However, due to broken equipment, these tests could no be conducted within the time-frame of this thesis.

6.2. Future work

Using a dual-transport model to simulate moisture diffusion through polymer materials, specifically PV materials, is currently the leading approach. However, alternative models have successfully been applied to non-PV materials. For example, Apeagyei. et al applied two non-Fickian models, a two-phase Langmuir-type model and a two-parameter time-variable model, to study moisture diffusion in asphalt mastics [166]. These models consider the equilibrium moisture uptake, M_{inf}, diffusion coefficients, and sample thickness. The Langmuir-type model modifies the Fickian model by adding two probability parameters related to the molecular phase of the absorbed water molecules; specifically, it assumes that the absorbed water molecules exist in two phases: free-phase and bound-phase. Diffusion of the free-phase water molecules follows Fick's law with a concentration-dependent diffusion coefficient. However, the free-phase water molecules can become bound with a probability, β, per unit time. The model further assumes that water molecules can leave the bound state with a probability, α, per unit time. The model was selected because it has successfully been used in moisture diffusion studies of glass epoxy and composite resins. The time-variable diffusion model is a function of three parameters: the equilibrium moisture content, an initial diffusion coefficient and a constant, λ, that describes the rate of change of diffusion with time. Both models were found to predict moisture diffusion extremely well and could be investigated in the context of PV materials.

To perform the material and climate variability analysis for non-Fickian diffusion, the intention was to apply the dual-transport method to the original moisture ingress model. The attempt was made, but computational limitations meant the implementation could not be completed and the simulations could not run. As the dual-transport method for simulating moisture ingress in PV encapsulants has only been applied to simple models thus far, both in this thesis and in literature, it is of particular interest to apply it to the original moisture ingress model and compare the simulations to experimental results to verify the approach. This would require high computational power and time.

Chapter 3 concluded that non-Fickian diffusion takes place in EVA encapsulants, and that EVA and PET degrade over time due to hydrolysis reactions. However, this investigation has only considered non-Fickian diffusion and material degradation separately, not to combining them. Once the approach for simulating material degradation is stronger, both phenomena should be studied together and implemented in the moisture ingress model. More experimental data would support the claims and findings.

The approach for simulating material degradation considered degradation reactions and the materials' structure, but focused on the water vapour transmission rate (WVTR) due to insufficient research into the material science of PV encapsulants and backsheets. More research on PV materials in particular, as, for example, EVA ranges in crystallinity depending on its purpose, would provide more insight into the materials' porosity, how and when it degrades, and how moisture diffusion changes with degradation. Furthermore, more research into the degradation of adhesive PV materials and incorporating them in the model can make it better reflect reality.

The motivation for this thesis was that moisture ingress in PV modules degrades the components, leading to reduced performance and operational lifetime. Consequently, PV modules have to be changed more regularly, increasing the LCOE for the technology, and requiring valuable resources to be replaced more frequently. Therefore, an economic and life-cycle analysis may be of interest. For example, ionomer has proved to be a very promising encapsulant material, but its high cost means EVA is typically favoured. Materials that better prevent moisture ingress may in fact reduce the LCOE and protect the valuable components for longer.

Bibliography

[1] E. Kabir, P. Kumar, S. Kumar, A. A. Adelodun, and K. H. Kim, "Solar energy: Potential and future prospects," *Renewable and Sustainable Energy Reviews*, vol. 82, pp. 894–900, 2018.

[2] S. Nabi Mughal, R. K. Jarial, S. Mughal, and Y. R. Sood, "A Review on Solar Photovoltaic Technology and Future Trends," in *National Conference on Recent Advances in Computer Science and IT (NCRACIT)*, vol. 1, no. 4, 2018, pp. 227–235.

[3] IRENA, "Renewable Power Generation Costs in 2022," Institution Renewable Energy Agency, Tech. Rep., 2023.

[4] B. Ehrler, E. Alarcón-Lladó, S. W. Tabernig, T. Veeken, E. C. Garnett, and A. Polman, "Photovoltaics reaching for the shockley-queisser limit," *ACS Energy Letters*, vol. 5, no. 9, pp. 3029–3033, 2020.

[5] M. A. Green, E. D. Dunlop, M. Yoshita, N. Kopidakis, K. Bothe, G. Siefer, and X. Hao, "Solar cell efficiency tables (version 62)," *Progress in Photovoltaics: Research and Applications*, vol. 31, no. 7, pp. 651–663, 2023.

[6] H. Xiong, C. Gan, X. Yang, Z. Hu, H. Niu, J. Li, J. Si, P. Xing, and X. Luo, "Corrosion behavior of crystalline silicon solar cells," *Microelectronics Reliability*, vol. 70, pp. 49–58, 2017.

[7] A. Blakers, N. Zin, K. R. McIntosh, and K. Fong, "High efficiency silicon solar cells," in *Energy Procedia*, vol. 33. Elsevier Ltd, 2013, pp. 1–10.

[8] M. S. Chowdhury, K. S. Rahman, T. Chowdhury, N. Nuthammachot, K. Techato, M. Akhtaruzzaman, S. K. Tiong, K. Sopian, and N. Amin, "An overview of solar photovoltaic panels' end-of-life material recycling," *Energy Strategy Reviews*, vol. 27, 2020.

[9] M. Santhakumari and N. Sagar, "A review of the environmental factors degrading the performance of silicon wafer-based photovoltaic modules: Failure detection methods and essential mitigation techniques," *Renewable and Sustainable Energy Reviews*, vol. 110, pp. 83–100, 2019.

[10] M. Aghaei, A. Fairbrother, A. Gok, S. Ahmad, S. Kazim, K. Lobato, G. Oreski, A. Reinders, J. Schmitz, M. Theelen, P. Yilmaz, and J. Kettle, "Review of degradation and failure phenomena in photovoltaic modules," *Renewable and Sustainable Energy Reviews*, vol. 159, 2022.

[11] Y. Lyu, A. Fairbrother, M. Gong, J. H. Kim, X. Gu, M. Kempe, S. Julien, K. T. Wan, S. Napoli, A. Hauser, G. O'Brien, Y. Wang, R. French, L. Bruckman, L. Ji, and K. Boyce, "Impact of environmental variables on the degradation of photovoltaic components and perspectives for the reliability assessment methodology," *Solar Energy*, vol. 199, pp. 425–436, 2020.

[12] O. K. Segbefia, A. G. Imenes, and T. O. Sætre, "Moisture ingress in photovoltaic modules: A review," *Solar Energy*, vol. 224, pp. 889–906, 2021.

[13] P. Hülsmann and G. M. Wallner, "Permeation of water vapour through polyethylene terephthalate (PET) films for back-sheets of photovoltaic modules," *Polymer Testing*, vol. 58, pp. 153–158, 2017.

[14] L. C. Andreani, A. Bozzola, P. Kowalczewski, M. Liscidini, and L. Redorici, "Silicon solar cells: Toward the efficiency limits," *Advances in Physics: X*, vol. 4, no. 1, 2019.

[15] M. Kumar and A. Kumar, "Performance assessment and degradation analysis of solar photovoltaic technologies: A review," *Renewable and Sustainable Energy Reviews*, vol. 78, pp. 554–587, 2017.

[16] A. Sinha, O. S. Sastry, and R. Gupta, “Nondestructive characterization of encapsulant discoloration effects in crystalline-silicon PV modules,” *Solar Energy Materials and Solar Cells*, vol. 155, pp. 234–242, 2016.

[17] M. A. Green, “Silicon photovoltaic modules: A brief history of the first 50 years,” *Progress in Photovoltaics: Research and Applications*, vol. 13, no. 5, pp. 447–455, 2005.

[18] A. W. Czanderna and F. J. Pern, “Encapsulation of PV modules using ethylene vinyl acetate copolymer as a pottant: A critical review,” *Solar Energy Materials and Solar Cells*, vol. 43, pp. 101–181, 1996.

[19] M. Kempe, “Overview of Scientific Issues Involved in Selection of Polymers for PV Applications,” in *37th IEEE Photovoltaic Specialists Conference*. IEEE, 2011.

[20] C. Peike, I. Haedrich, K.-A. Weiss, and I. Durr, “Overview of PV module encapsulation materials,” *Photovoltaics International*, vol. 19, pp. 85–92, 2013.

[21] B. Adothu, P. Bhatt, S. Chattopadhyay, S. Zele, J. Oderkerk, H. P. Sagar, F. R. Costa, and S. Mallick, “Newly developed thermoplastic polyolefin encapsulant – A potential candidate for crystalline silicon photovoltaic modules encapsulation,” *Solar Energy*, vol. 194, pp. 581–588, 2019.

[22] G. Oreski and G. M. Wallner, “Evaluation of the aging behavior of ethylene copolymer films for solar applications under accelerated weathering conditions,” *Solar Energy*, vol. 83, no. 7, pp. 1040–1047, 2009.

[23] M. D. Kempe, G. J. Jorgensen, K. M. Terwilliger, T. J. McMahon, C. E. Kennedy, and T. T. Borek, “Acetic acid production and glass transition concerns with ethylene-vinyl acetate used in photovoltaic devices,” *Solar Energy Materials and Solar Cells*, vol. 91, no. 4, pp. 315–329, 2007.

[24] M. C. C. d. Oliveira, A. S. A. Diniz Cardoso, M. M. Viana, and V. d. F. C. Lins, “The causes and effects of degradation of encapsulant ethylene vinyl acetate copolymer (EVA) in crystalline silicon photovoltaic modules: A review,” *Renewable and Sustainable Energy Reviews*, vol. 81, pp. 2299–2317, 2018.

[25] O. Hasan and A. F. Arif, “Performance and life prediction model for photovoltaic modules: Effect of encapsulant constitutive behavior,” *Solar Energy Materials and Solar Cells*, vol. 122, pp. 75–87, 2014.

[26] B. Lin, C. Zheng, Q. Zhu, and F. Xie, “A polyolefin encapsulant material designed for photovoltaic modules: from perspectives of peel strength and transmittance,” *Journal of Thermal Analysis and Calorimetry*, vol. 140, no. 5, pp. 2259–2265, 2020.

[27] G. Oreski, A. Omazic, G. C. Eder, Y. Voronko, L. Neumaier, W. Mühleisen, C. Hirschl, G. Ujvari, R. Ebner, and M. Edler, “Properties and degradation behaviour of polyolefin encapsulants for photovoltaic modules,” *Progress in Photovoltaics: Research and Applications*, vol. 28, no. 12, pp. 1277–1288, 2020.

[28] J. Kim, M. Rabelo, S. P. Padi, H. Yousuf, E. C. Cho, and J. Yi, “A review of the degradation of photovoltaic modules for life expectancy,” *Energies*, vol. 14, no. 14, 2021.

[29] K. J. Geretschläger, G. M. Wallner, and J. Fischer, “Structure and basic properties of photovoltaic module backsheet films,” *Solar Energy Materials and Solar Cells*, vol. 144, pp. 451–456, 2016.

[30] M. M. Kusato Hirota and T. Amioka, “Durability test of Poly-Ethylene-Terephthalate (PET) film for backsheet,” 2011.

[31] P. Hülsmann and K. A. Weiss, “Simulation of water ingress into PV-modules: IEC-testing versus outdoor exposure,” *Solar Energy*, vol. 115, pp. 347–353, 2015.

[32] J. Schlothauer, S. Jungwirth, M. Köhl, and B. Röder, “Degradation of the encapsulant polymer in outdoor weathered photovoltaic modules: Spatially resolved inspection of EVA ageing by fluorescence and correlation to electroluminescence,” *Solar Energy Materials and Solar Cells*, vol. 102, pp. 75–85, 2012.

[33] O. K. Segbefia, N. Akhtar, and T. O. Sætre, “Moisture induced degradation in field-aged multicrystalline silicon photovoltaic modules,” *Solar Energy Materials and Solar Cells*, vol. 258, 2023.

[34] A. Omazic, G. Oreski, M. Halwachs, G. C. Eder, C. Hirschl, L. Neumaier, G. Pinter, and M. Erceg, “Relation between degradation of polymeric components in crystalline silicon PV module and climatic conditions: A literature review,” *Solar Energy Materials and Solar Cells*, vol. 192, pp. 123–133, 2019.

[35] G. Oreski, A. Mihaljevic, Y. Voronko, and G. C. Eder, “Acetic acid permeation through photovoltaic backsheets: Influence of the composition on the permeation rate,” *Polymer Testing*, vol. 60, pp. 374–380, 2017.

[36] T. H. Kim, N. C. Park, and D. H. Kim, “The effect of moisture on the degradation mechanism of multi-crystalline silicon photovoltaic module,” *Microelectronics Reliability*, vol. 53, pp. 1823–1827, 2013.

[37] M. D. Kempe, “Control of Moisture Ingress into Photovoltaic Modules,” in *31st IEEE Photovoltaics Specialists Conference and Exhibition*, National Renewable Energy Laboratory. National Renewable Energy Laboratory, 2005.

[38] A. Badiee, R. Wildman, and I. Ashcroft, “Effect of UV aging on degradation of Ethylene-vinyl Acetate (EVA) as encapsulant in photovoltaic (PV) modules,” in *Proceedings of SPIE - The International Society for Optical Engineering*, vol. 9179. SPIE, 2014.

[39] C. Peike, S. Hoffmann, P. Hülsmann, B. Thaidigsmann, K. A. Weiß, M. Koehl, and P. Bentz, “Origin of damp-heat induced cell degradation,” *Solar Energy Materials and Solar Cells*, vol. 116, pp. 49–54, 2013.

[40] A. Sinha, H. Gopalakrishna, A. Bala Subramaniyan, D. Jain, J. Oh, D. Jordan, and G. S. Tamizhmani, “Prediction of Climate-Specific Degradation Rate for Photovoltaic Encapsulant Discoloration,” *IEEE Journal of Photovoltaics*, vol. 10, no. 4, pp. 1093–1101, 2020.

[41] M. Peleg, M. D. Normand, and M. G. Corradini, “The Arrhenius Equation Revisited,” *Critical reviews in food science and nutrition*, vol. 52, no. 9, pp. 830–851, 2012.

[42] L. A. Escobar and W. Q. Meeker, “A review of accelerated test models,” *Statistical Science*, vol. 21, no. 4, pp. 552–577, 2006.

[43] W. Luo, Y. S. Khoo, P. Hacke, V. Naumann, D. Lausch, S. P. Harvey, J. P. Singh, J. Chai, Y. Wang, A. G. Aberle, and S. Ramakrishna, “Potential-induced degradation in photovoltaic modules: A critical review,” *Energy and Environmental Science*, vol. 10, pp. 43–68, 2017.

[44] V. Sharma and S. S. Chandel, “A novel study for determining early life degradation of multicrystalline-silicon photovoltaic modules observed in western Himalayan Indian climatic conditions,” *Solar Energy*, vol. 134, pp. 32–44, 2016.

[45] D. C. Jordan and S. R. Kurtz, “Photovoltaic degradation rates - An Analytical Review,” *Progress in Photovoltaics: Research and Applications*, vol. 21, pp. 12–29, 2013.

[46] D. C. Jordan, T. J. Silverman, J. H. Wohlgemuth, S. R. Kurtz, and K. T. VanSant, “Photovoltaic failure and degradation modes,” *Progress in Photovoltaics: Research and Applications*, vol. 25, no. 4, pp. 318–326, 2017.

[47] S. Chattopadhyay, R. Dubey, V. Kuthanazhi, J. J. John, C. S. Solanki, A. Kottantharayil, B. M. Arora, K. L. Narasimhan, V. Kuber, J. Vasi, A. Kumar, and O. S. Sastry, “Visual degradation in field-aged crystalline silicon PV modules in India and correlation with electrical degradation,” *IEEE Journal of Photovoltaics*, vol. 4, no. 6, pp. 1470–1476, 2014.

[48] A. Gok, D. A. Gordon, M. Wang, R. H. French, and L. S. Bruckman, “Degradation Science and Pathways in PV Systems,” in *Durability and Reliability of Polymers and Other Materials in Photovoltaic Modules*. William Andrew Publishing, 2019, pp. 47–93.

[49] M. Köntges, U. Jahn, K. A. Berger, S. Altmann, T. Heimberg, and K. A. Berger, “Mean Degradation Rates In PV Systems For Various Kinds Of PV Module Failures,” in *32nd European Photovoltaic Solar Energy Conference and Exhibition*, 2018, pp. 1435–1443.

[50] T. J. Peshek, J. S. Fada, and I. T. Martin, “Degradation processes in photovoltaic cells,” in *Durability and Reliability of Polymers and Other Materials in Photovoltaic Modules*. Elsevier, 2019, pp. 97–118.

[51] A. Ndiaye, A. Charki, A. Kobi, C. M. Kébé, P. A. Ndiaye, and V. Sambou, “Degradations of silicon photovoltaic modules: A literature review,” *Solar Energy*, vol. 96, pp. 140–151, 2013.

[52] L. M. Shaker, A. Alamiery, W. N. R. W. Isahak, and W. K. Al-Azzawi, “Corrosion in solar cells: challenges and solutions for enhanced performance and durability,” *Journal of Optics*, 2023.

[53] C. Cui, Q. Ding, S. Yu, C. Yu, D. Jiang, C. Hu, Z. Gu, and J. Zhu, “Strategies to break the trade-off between infrared transparency and conductivity,” *Progress in Materials Science*, vol. 136, 2023.

[54] J. H. Wohlgemuth and S. Kurtz, “Reliability Testing beyond Qualification as a Key Component in Photovoltaic’s Progress toward Grid Parity,” in *2011 International Reliability Physics Symposium*, 2011.

[55] M. A. Quintana, D. L. King, T. J. McMahon, and C. R. Osterwald, “Commonly observed degradation in field-aged photovoltaic modules,” in *Conference Record of the Twenty-Ninth IEEE Photovoltaic Specialists Conference*, 2002, pp. 1436–1439.

[56] F. J. Pern and S. H. Glick, “Thermal processing of EVA encapsulants and effects of formulation additives [for solar cells],” in *Conference Record of the Twenty Fifth IEEE Photovoltaic Specialists Conference*. IEEE, 1996, pp. 1251–1254.

[57] G. Oreski and G. M. Wallner, “Aging mechanisms of polymeric films for PV encapsulation,” *Solar Energy*, vol. 79, no. 6, pp. 612–617, 2005.

[58] M. Knausz, G. Oreski, M. Schmidt, P. Guttmann, K. Berger, Y. Voronko, G. Eder, T. Koch, and G. Pinter, “Thermal expansion behavior of solar cell encapsulation materials,” *Polymer Testing*, vol. 44, pp. 160–167, 2015.

[59] M. A. Munoz, M. C. Alonso-García, N. Vela, and F. Chenlo, “Early degradation of silicon PV modules and guaranty conditions,” *Solar Energy*, vol. 85, no. 9, pp. 2264–2274, 2011.

[60] E. Molenbroek, D. W. Waddington, and K. A. Emery, “Hot spot susceptibility and testing of PV modules,” in *Conference Record of the 22th IEEE*. National Renewable Energy Laboratory, 1991, pp. 547–552.

[61] K. A. Kim, G. S. Seo, B. H. Cho, and P. T. Krein, “Photovoltaic Hot-Spot Detection for Solar Panel Substrings Using AC Parameter Characterization,” *IEEE Transactions on Power Electronics*, vol. 31, no. 2, pp. 1121–1130, 2016.

[62] S. M. Det, H. Fechner, T. Krametz, and W. Jahna, “Quality testing for PV-modules according to standards and performance control for supporting manufacturing,” in *19 th EUPVSEC*, 2004, pp. 7–11.

[63] B. M. Habersberger, P. Hacke, and L. Madenjian, “Evaluation of the PID-s susceptibility of modules encapsulated in materials of varying resistivity,” in *2018 IEEE 7th World Conference on Photovoltaic Energy Conversion (WCPEC)*, 2018, pp. 3807–3809.

[64] M. A. Islam, M. Hasanuzzaman, and N. A. Rahim, “A comparative investigation on in-situ and laboratory standard test of the potential induced degradation of crystalline silicon photovoltaic modules,” *Renewable Energy*, vol. 127, pp. 102–113, 2018.

[65] S. L. Moffitt, B. H. Hamadani, and X. Gu, “Characterizing Solar Panel Encapsulants during Potential Induced Degradation,” in *Conference Record of the IEEE Photovoltaic Specialists Conference*. Institute of Electrical and Electronics Engineers Inc., 2021, pp. 1556–1559.

[66] A. A. Hasan, A. A. Alkahtani, S. A. Shahahmadi, M. N. E. Alam, M. A. Islam, and N. Amin, “Delamination-and Electromigration-Related Failures in Solar Panels - A Review,” *Sustainability*, vol. 13, no. 12, 2021.

[67] R. Singh, C. Schmidt, and C. Libby, “Literature Study and Risk Analysis for Potential Induced Degradation,” Electric Power Research Institute (EPRI), Tech. Rep., 2014.

[68] H. Hashigami, Y. Itakura, and T. Saitoh, “Effect of illumination conditions on Czochralski-grown silicon solar cell degradation,” *Journal of Applied Physics*, vol. 93, no. 7, pp. 4240–4245, 2003.

[69] K. Bothe, R. Hezel, and J. Schmidt, “Recombination-enhanced formation of the metastable boron-oxygen complex in crystalline silicon,” *Applied Physics Letters*, vol. 83, no. 6, pp. 1125–1127, 2003.

[70] J. Lindroos and H. Savin, “Review of light-induced degradation in crystalline silicon solar cells,” *Solar Energy Materials and Solar Cells*, vol. 147, pp. 115–126, 2016.

[71] B. Sopori, P. Basnyat, S. Devayajanam, S. Shet, V. Mehta, J. Binns, and J. Appel, “Understanding Light-Induced Degradation of c-Si Solar Cells,” in *38th IEEE Photovoltaic Specialists Conference*, 2012, pp. 1115–11 220.

[72] S. Lindig, I. Kaaya, K. A. Weis, D. Moser, and M. Topic, “Review of statistical and analytical degradation models for photovoltaic modules and systems as well as related improvements,” *IEEE Journal of Photovoltaics*, vol. 8, no. 6, pp. 1773–1786, 2018.

[73] M. Kendall, *Time Series*, 2nd ed. Charles Griffin, 1976.

[74] K. H. Zou, K. Tuncali, and S. G. Silverman, “Correlation and simple linear regression,” *Radiology*, vol. 227, no. 3, pp. 617–622, 2003.

[75] S. I. Bangdiwala, “Regression: simple linear,” *International Journal of Injury Control and Safety Promotion*, vol. 25, no. 1, pp. 113–115, 2018.

[76] R. B. Cleveland, W. S. Cleveland, J. E. McRae, and I. Terpenning, “STL: A Seasonal-Trend Decomposition Procedure Based on Loess,” *Journal of Official Statistics*, vol. 6, no. 1, pp. 3–33, 1990.

[77] M. Koehl, M. Heck, and S. Wiesmeier, “Modelling of conditions for accelerated lifetime testing of Humidity impact on PV-modules based on monitoring of climatic data,” *Solar Energy Materials and Solar Cells*, vol. 99, pp. 282–291, 2012.

[78] C. Y. Lee and G. B. Lee, “Humidity sensors: A review,” *Sensor Letters*, vol. 3, no. 1, pp. 1–15, 2005.

[79] I. Kaaya, M. Koehl, A. P. Mehilli, S. De Cardona Mariano, and K. A. Weiss, “Modeling Outdoor Service Lifetime Prediction of PV Modules: Effects of Combined Climatic Stressors on PV Module Power Degradation,” *IEEE Journal of Photovoltaics*, vol. 9, no. 4, pp. 1105–1112, 2019.

[80] B. Braisaz, C. Duchayne, M. V. Iseghem, and K. Radouane, “PV aging model applied to several meteorological conditions,” in *EU PVSEC*, 2014.

[81] A. B. Subramaniyan, R. Pan, J. Kuitche, and G. TamizhMani, “Quantification of Environmental Effects on PV Module Degradation: A Physics-Based Data-Driven Modeling Method,” *IEEE Journal of Photovoltaics*, vol. 8, no. 5, pp. 1289–1296, 2018.

[82] E. Annigoni, M. Jankovec, F. Galliano, H. Y. Li, L.-E. Perret-Aebi, M. Topič, F. Sculati-Meillaud, A. Virtuani, and C. Ballif, “Modeling potential-induced degradation (PID) in crystalline silicon solar cells: From accelerated-aging laboratory testing to outdoor prediction,” in *32nd European Photovoltaic Solar Energy Conference and Exhibition*, 2016, pp. 1558–1563.

[83] P. Hacke, S. Spataru, K. Terwilliger, G. Perrin, S. Glick, S. Kurtz, and J. Wohlgemuth, "Accelerated Testing and Modeling of Potential-Induced Degradation as a Function of Temperature and Relative Humidity," *IEEE Journal of Photovoltaics*, vol. 5, no. 6, pp. 1549–1553, 2015.

[84] K. C. Norris and A. H. Landzberg, "Reliability of Controlled Collapse Interconnections," *IBM Journal of Research and Development*, vol. 13, no. 3, pp. 266–271, 1969.

[85] T. Rahman, A. A. Mansur, M. S. Hossain Lipu, M. S. Rahman, R. H. Ashique, M. A. Houran, R. M. Elavarasan, and E. Hossain, "Investigation of Degradation of Solar Photovoltaics: A Review of Aging Factors, Impacts, and Future Directions toward Sustainable Energy Management," *Energies*, vol. 16, no. 9, 2023.

[86] M. Theristis, A. Livera, C. B. Jones, G. Makrides, G. E. Georghiou, and J. S. Stein, "Nonlinear Photovoltaic Degradation Rates: Modeling and Comparison against Conventional Methods," *IEEE Journal of Photovoltaics*, vol. 10, no. 4, pp. 1112–1118, 2020.

[87] D. C. Jordan, T. J. Silverman, B. Sekulic, and S. R. Kurtz, "PV degradation curves: non-linearities and failure modes," *Progress in Photovoltaics: Research and Applications*, vol. 25, no. 7, pp. 583–591, 2017.

[88] M. Halwachs, L. Neumaier, N. Vollert, L. Maul, S. Dimitriadis, Y. Voronko, G. C. Eder, A. Omazic, W. Mühleisen, C. Hirschl, M. Schwark, K. A. Berger, and R. Ebner, "Statistical evaluation of PV system performance and failure data among different climate zones," *Renewable Energy*, vol. 139, pp. 1040–1060, 2019.

[89] J. Wachsmuth, A. Distler, D. Deribew, M. Salvador, C. J. Brabec, and H. J. Egelhaaf, "Overcoming Moisture-Induced Degradation in Organic Solar Cells," *Advanced Engineering Materials*, vol. 25, no. 16, 2023.

[90] T. Sidawi, R. E. Kumar, I. Slauch, R. Meier, M. I. Bertoni, and D. P. Fenning, "Moisture Ingress and Distribution in Bifacial Silicon Photovoltaics," *IEEE Journal of Photovoltaics*, vol. 13, no. 3, pp. 365–372, 2023.

[91] S. Villa, R. Aninat, P. Yilmaz, A. Kingma, M. Dziechciarz, J. van den Berg, K. Bakker, and M. Theelen, "Insights into the moisture-induced degradation mechanisms on field-deployed CIGS modules," *Progress in Photovoltaics: Research and Applications*, vol. 31, no. 8, pp. 824–839, 2023.

[92] K. J. Xu, R. T. Wang, A. F. Xu, J. Y. Chen, and G. Xu, "Hysteresis and Instability Predicted in Moisture Degradation of Perovskite Solar Cells," *ACS Applied Materials and Interfaces*, vol. 12, no. 43, pp. 48 882–48 889, 2020.

[93] P. Toloueinia, H. Khassaf, A. Shirazi Amin, Z. M. Tobin, S. P. Alpay, and S. L. Suib, "Moisture-Induced Structural Degradation in Methylammonium Lead Iodide Perovskite Thin Films," *ACS Applied Energy Materials*, vol. 3, no. 9, pp. 8240–8248, 2020.

[94] D. Jimenez Pelarda, "Modelling moisture ingress and impact on PV module degradation," Ph.D. dissertation, Delft University of Technology, 2023.

[95] N. Kim and C. Han, "Experimental characterization and simulation of water vapor diffusion through various encapsulants used in PV modules," *Solar Energy Materials and Solar Cells*, vol. 116, pp. 68–75, 2013.

[96] M. Hanika, H. C. Langowski, U. Moosheimer, and W. Peukert, "Inorganic layers on polymer films - Influence of defects and morphology on barrier properties," *Chemical Engineering and Technology*, vol. 26, no. 5, pp. 605–614, 2003.

[97] C. Yang, X. Xing, Z. Li, and S. Zhang, "A Comprehensive Review on Water Diffusion in Polymers Focusing on the Polymer–Metal Interface Combination," *Polymers*, vol. 12, no. 1, 2020.

[98] M. D. Kempe and J. H. Wohlgemuth, "Evaluation of Temperature and Humidity on PV Module Component Degradation," National Renewable Energy Laboratory, Tech. Rep., 2013.

[99] A. Dadaniya and N. V. Datla, “Water diffusion simulation in photovoltaic module based on the characterization of encapsulant material using in-situ gravimetric technique,” *Solar Energy Materials and Solar Cells*, vol. 201, 2019.

[100] G. J. Jorgensen, K. M. Terwilliger, J. A. DelCueto, S. H. Glick, M. D. Kempe, J. W. Pankow, F. J. Pern, and T. J. McMahon, “Moisture transport, adhesion, and corrosion protection of PV module packaging materials,” *Solar Energy Materials and Solar Cells*, vol. 90, no. 16, pp. 2739–2775, 2006.

[101] P. Hülsmann, K. A. Weiß, and M. Köhl, “Temperature-dependent water vapour and oxygen permeation through different polymeric materials used in photovoltaic-modules,” *Progress in Photovoltaics: Research and Applications*, vol. 22, no. 4, pp. 415–421, 2014.

[102] D. Wisniewski, R. Lv, S. V. Nair, J. N. Jaubert, T. Xu, and H. E. Ruda, “Measurement and modelling of water ingress into double-glass photovoltaic modules,” *Progress in Photovoltaics: Research and Applications*, vol. 27, no. 2, pp. 144–151, 2019.

[103] E. Barykina and A. Hammer, “Modeling of photovoltaic module temperature using Faiman model: Sensitivity analysis for different climates,” *Solar Energy*, vol. 146, pp. 401–416, 2017.

[104] C. Correa-Betanzo, H. Calleja, and S. De León-Aldaco, “Module temperature models assessment of photovoltaic seasonal energy yield,” *Sustainable Energy Technologies and Assessments*, vol. 27, pp. 9–16, 2018.

[105] R. C. Rodgers and G. E. Hill, “Equations for vapour pressure versus temperature: Derivation and use of the Antoine equation on a hand-held programmable calculator,” *British Journal of Anaesthesia*, vol. 50, no. 5, pp. 415–424, 1978.

[106] M. Gagliardi and M. Paggi, “Long-term EVA degradation simulation: Climatic zones comparison and possible revision of accelerated tests,” *Solar Energy*, vol. 159, pp. 882–897, 2018.

[107] N. Kyranaki, “Corrosion in crystalline silicon photovoltaic modules and the influence on performance,” Ph.D. dissertation, Loughborough University, 2020.

[108] COMSOL, “Building the mesh for a model geometry in COMSOL Multiphysics.”

[109] M. Kontges, A. Morlier, G. Eder, E. Fleis, B. Kubicek, and J. Lin, “Review: Ultraviolet Fluorescence as Assessment Tool for Photovoltaic Modules,” *IEEE Journal of Photovoltaics*, vol. 10, no. 2, pp. 616–633, 2020.

[110] E. R. Anagha, S. V. Kulkarni, and N. Shiradkar, “Moisture Ingress Modeling in c-Si PV Modules using Finite Element Simulations Based on Dual Transport Diffusion,” in *Conference Record of the IEEE Photovoltaic Specialists Conference*, 2021, pp. 2470–2474.

[111] H. Shirangi, J. Auersperg, M. Koyuncu, H. Walter, W. H. Muller, and B. Michel, “Characterization of Dual-Stage Moisture Diffusion, Residual Moisture Content and Hygroscopic Swelling of Epoxy Molding Compounds,” in *EuroSimE 2008 - International Conference on Thermal, Mechanical and Multi-Physics Simulation and Experiments in Microelectronics and Micro-Systems*, 2008, pp. 1–8.

[112] S. Mitterhofer, C. Barretta, L. F. Castillon, G. Oreski, M. Topic, and M. Jankovec, “A Dual-Transport Model of Moisture Diffusion in PV Encapsulants for Finite-Element Simulations,” *IEEE Journal of Photovoltaics*, vol. 10, no. 1, pp. 94–102, 2020.

[113] H. Ardebili, J. Zhang, and M. G. Pecht, “Characterization of encapsulant properties,” in *Encapsulation Technologies for Electronic Applications*. Elsevier, 2018, pp. 221–258.

[114] C. Maggana and P. Pissis, “Water sorption and diffusion studies in an epoxy resin system,” *Journal of Polymer Science, Part B: Polymer Physics*, vol. 37, no. 11, pp. 1165–1182, 1999.

[115] P. M. Jacobs and F. R. Jones, “Diffusion of moisture into two-phase polymers,” *Journal of Materials Science*, vol. 24, no. 7, pp. 2331–2336, 1989.

[116] S. Popineau, C. Rondeau-Mouro, C. Sulpice-Gaillet, and M. E. Shanahan, “Free/bound water absorption in an epoxy adhesive,” *Polymer*, vol. 46, no. 24, pp. 10 733–10 740, 2005.

[117] J. Zhou and J. P. Lucas, “Hygrothermal effects of epoxy resin. Part I: the nature of water in epoxy,” *Polymer*, vol. 40, pp. 5505–5512, 1999.

[118] M. Y. Chiang and M. Fernandez-Garcia, “Relation of swelling and Tg depression to the apparent free volume of a particle-filled, epoxy-based adhesive,” *Journal of Applied Polymer Science*, vol. 87, no. 9, pp. 1436–1444, 2003.

[119] J. S. Vrentas, J. L. Duda, and A. □. Hou, “Anomalous sorption in poly(ethyl methacrylate),” *Journal of Applied Polymer Science*, vol. 29, no. 1, pp. 399–406, 1984.

[120] H. Ardebili, E. H. Wong, and M. Pecht, “Hygroscopic swelling and sorption characteristics of epoxy molding compounds used in electronic packaging,” *IEEE Transactions on Components and Packaging Technologies*, vol. 26, no. 1, pp. 206–214, 2003.

[121] B. K. Bhattacharyya, W. A. Huffman, W. E. Jahsman, and B. Natarajan, “Moisture absorption and mechanical performance of surface mountable plastic packages,” in *38th Electronics Components Conference 1988*, 1988, pp. 49–58.

[122] E. H. Wong and R. Rajoo, “Moisture absorption and diffusion characterisation of packaging materials - Advanced treatment,” *Microelectronics Reliability*, vol. 43, no. 12, pp. 2087–2096, 2003.

[123] E. H. Wong, K. C. Chan, T. B. Lim, and T. F. Lam, “Non-Fickian moisture properties characterisation and diffusion modeling for electronic packages,” in *Proceedings - Electronic Components and Technology Conference*, 1999, pp. 302–306.

[124] M. D. Placette, X. Fan, J.-H. Zhao, and D. Edwards, “A Dual Stage Model of Anomalous Moisture Diffusion and Desorption in Epoxy Mold Compounds,” in *12th Intl. Conf. on Thermal, Mechanical & Multi-Physics Simulation and Experiments in Microelectronics and Microsystems*, 2011, pp. 1–8.

[125] W. Lei, M. K. Rigozzi, and D. R. McKenzie, “The physics of confined flow and its application to water leaks, water permeation and water nanoflows: A review,” *Reports on Progress in Physics*, vol. 79, no. 2, 2016.

[126] C. Sammon, J. Yarwood, and N. Everall, “A FTIR-ATR study of liquid diffusion processes in PET films: comparison of water with simple alcohols,” *Polymer*, vol. 41, pp. 2521–2534, 2000.

[127] S. Sicardi, L. Manna, and M. Banchero, “Comparison of dye diffusion in poly(ethylene terephthalate) films in the presence of a supercritical or aqueous solvent,” in *Industrial and Engineering Chemistry Research*, vol. 39, no. 12. ACS, 2000, pp. 4707–4713.

[128] C. Hirschl, L. Neumaier, S. Puchberger, W. Mühleisen, G. Oreski, G. C. Eder, R. Frank, M. Tranitz, M. Schoppa, M. Wendt, N. Bogdanski, A. Plösch, and M. Kraft, “Determination of the degree of ethylene vinyl acetate crosslinking via Soxhlet extraction: Gold standard or pitfall?” *Solar Energy Materials and Solar Cells*, vol. 143, pp. 494–502, 2015.

[129] K. Hara and Y. Chiba, “Spectroscopic investigation of long-term outdoor-exposed crystalline silicon photovoltaic modules,” *Journal of Photochemistry and Photobiology A: Chemistry*, vol. 404, 2021.

[130] V. Kholodovych and W. J. Welsh, “Thermal-Oxidative Stability and Degradation of Polymers,” in *Physical Properties of Polymers Handbook*, 2nd ed. Springer, 2007, ch. 54, pp. 927–938.

[131] M. Gagliardi, P. Lenarda, and M. Paggi, “A reaction-diffusion formulation to simulate EVA polymer degradation in environmental and accelerated ageing conditions,” *Solar Energy Materials and Solar Cells*, vol. 164, pp. 93–106, 2017.

[132] S. S. Hosseini, S. Taheri, A. Zadhoush, and A. Mehrabani-Zeinabad, “Hydrolytic degradation of poly(ethylene terephthalate),” *Journal of Applied Polymer Science*, vol. 103, no. 4, pp. 2304–2309, 2007.

[133] C. Sammon, J. Yarwood, and N. Everall, “An FT±IR study of the effect of hydrolytic degradation on the structure of thin PET films,” *Polymer Degradation and Stability*, vol. 67, pp. 149–158, 2000.

[134] F. Dubelley, E. Planes, C. Bas, E. Pons, B. Yrieix, and L. Flandin, “Predictive durability of polyethylene terephthalate toward hydrolysis over large temperature and relative humidity ranges,” *Polymer*, vol. 142, pp. 285–292, 2018.

[135] B. Brune, I. Ortner, G. C. Eder, Y. Voronko, A. Gassner, K. A. Berger, G. Oreski, K. Knöbl, L. Neumaier, and M. Feichtner, “Connecting material degradation and power loss of PV modules using advanced statistical methodology,” *Solar Energy Materials and Solar Cells*, vol. 260, 2023.

[136] N. Kim, H. Kang, K.-J. Hwang, C. Han, W. S. Hong, D. Kim, E. Lyu, and H. Kim, “Study on the degradation of different types of backsheets used in PV module under accelerated conditions,” *Solar Energy Materials & Solar Cells*, vol. 120, pp. 543–548, 2014.

[137] G. Oreski, B. Ottersböck, C. Barretta, P. Christöfl, S. Radl, and G. Pinter, “Degradation of PET – Quantitative estimation of changes in molar mass using mechanical and thermal characterization methods,” *Polymer Testing*, vol. 125, 2023.

[138] G. Jorgensen, K. Terwilliger, S. Glick, J. Pern, and T. Mcmahon, “Materials Testing for PV Module Encapsulation,” in *National Center for Photovoltaics and Solar Program Review Meeting*. NREL, 2003. [Online]. Available: http://www.osti.gov/bridge

[139] B. Adothu, F. R. Costa, and S. Mallick, “Damp heat resilient thermoplastic polyolefin encapsulant for photovoltaic module encapsulation,” *Solar Energy Materials and Solar Cells*, vol. 224, 2021.

[140] C. Barretta, G. Oreski, S. Feldbacher, K. Resch-Fauster, and R. Pantani, “Comparison of degradation behavior of newly developed encapsulation materials for photovoltaic applications under different artificial ageing tests,” *Polymers*, vol. 13, no. 2, pp. 1–21, 2021.

[141] Y. Bai, Y. Zhao, J. Li, H. Chen, A. Lambertz, Q. Qiu, C. Qian, J. Shi, W. Liu, T. Chen, J. Yu, K. Ding, and J. Yu, “Lower Levelized Cost of Energy Achievement of Silicon Heterojunction Solar Modules with Low Water Vapor Transmission Rate Encapsulants,” *Energy Technology*, vol. 11, no. 7, 2023.

[142] A. K. Schnatmann, F. Schoden, and E. Schwenzfeier-Hellkamp, “Sustainable PV Module Design—Review of State-of-the-Art Encapsulation Methods,” *Sustainability*, vol. 14, no. 16, 2022.

[143] J. Tracy, N. Bosco, C. Delgado, and R. Dauskardt, “Durability of ionomer encapsulants in photovoltaic modules,” *Solar Energy Materials and Solar Cells*, vol. 208, 2020.

[144] H.-Y. Li, “Assessment of Photovoltaic Module Failures in the Field,” IEA, Tech. Rep., 2017. [Online]. Available: https://www.researchgate.net/publication/319490563

[145] M. Jankovec, E. Annigoni, C. Ballif, and M. Topic, “In-situ Determination of Moisture Diffusion Properties of PV Module Encapsulants Using Digital Humidity Sensors,” in *IEEE 7th World Conference on Photovoltaic Energy Conversion (WCPEC)*, 2018, pp. 415–417.

[146] J. H. Park and S.-H. Hwang, “A Polyolefin Elastomer Encapsulant Modified by an Ethylene–Propylene–Diene Terpolymer for Photovoltaic Applications,” *ACS Omega*, 1 2024. [Online]. Available: https://pubs.acs.org/doi/10.1021/acsomega.3c07969

[147] M. Yang, R. Schäffler, T. Repmann, and K. Orgassa, “Moisture Absorption and Desorption in an Ionomer-Based Encapsulant: A Type of Self-Breathing Encapsulant for CIGS Thin-Film PV Modules,” *Engineering*, vol. 6, no. 12, pp. 1403–1407, 2020.

[148] M. M. Brette, A. H. Holm, A. D. Drozdov, and J. d. C. Christiansen, “Pure Hydrolysis of Polyamides: A Comparative Study,” *Chemistry (Switzerland)*, vol. 6, no. 1, pp. 13–50, 2024.

[149] C. Peike, P. Hülsmann, M. Blüml, P. Schmid, K.-A. Weiß, and M. Köhl, “Impact of Permeation Properties and Backsheet-Encapsulant Interactions on the Reliability of PV Modules,” *ISRN Renewable Energy*, vol. 2012, pp. 1–5, 2012.

[150] D. Cui, S. Liang, and D. Wang, “Observed and projected changes in global climate zones based on Köppen climate classification,” *Wiley Interdisciplinary Reviews: Climate Change*, vol. 12, no. 3, 2021.

[151] M. Kottek, J. Grieser, C. Beck, B. Rudolf, and F. Rubel, “World map of the Köppen-Geiger climate classification updated,” *Meteorologische Zeitschrift*, vol. 15, no. 3, pp. 259–263, 2006.

[152] S. Mitterhofer, M. Jankovec, M. Topic, and M. Topič, “One-and two-dimensional finite element analysis of humidity ingress in polymeric materials,” in *54th International Conference on Microelectronic Devices and Technologies*, 2018, pp. 93–98. [Online]. Available: https://www.researchgate.net/publication/328048106

[153] M. D. Kempe, A. A. Dameron, and M. O. Reese, “Evaluation of moisture ingress from the perimeter of photovoltaic modules,” *Progress in Photovoltaics: Research and Applications*, vol. 22, no. 11, pp. 1159–1171, 2014.

[154] S. Mitterhofer, “Modelling and monitoring of moisture transport phenomena in polymeric materials and photovoltaic modules,” Ph.D. dissertation, University of Ljubljana, 2021.

[155] P. Hacke, M. Owen-Bellini, M. D. Kempe, D. B. Sulas-Kern, D. C. Miller, M. Jankovec, S. Mitterhofer, M. Topič, S. Spataru, W. Gambogi, and T. Tanahashi, “Acceleration Factors for Combined-Accelerated Stress Testing of Photovoltaic Modules,” *Solar RRL*, vol. 7, no. 12, 2023.

[156] K. A. Weiß, E. Klimm, and I. Kaaya, “Accelerated aging tests vs field performance of PV modules,” *Progress in Energy*, vol. 4, no. 4, 2022.

[157] C. South, “Acceleration Factors and Life Predictions,” in *53rd International Symposium on Microelectronics*. IMAPS, 2020. [Online]. Available: http://meridian.allenpress.com/ism/article-pdf/2020/1/000100/2708258/i2380-4505-2020-1-000100.pdf

[158] D. A. Nissen, “The Low-Temperature Water Vapor Oxidation of Calcium by Water Vapour,” *Oxidation of Metals*, vol. 11, no. 5, pp. 241–261, 1977.

[159] M. Jankovec, F. Galliano, E. Annigoni, H. Y. Li, F. Sculati-Meillaud, L. E. Perret-Aebi, C. Ballif, and M. Topic, “In-Situ Monitoring of Moisture Ingress in PV Modules Using Digital Humidity Sensors,” *IEEE Journal of Photovoltaics*, vol. 6, no. 5, pp. 1152–1159, 2016.

[160] J. Slapšak, S. Mitterhofer, M. Topic, and M. Jankovec, “Wireless System for In Situ Monitoring of Moisture Ingress in PV Modules,” *IEEE Journal of Photovoltaics*, vol. 9, no. 5, pp. 1316–1323, 2019.

[161] S. Mitterhofer, J. Slapsak, A. Astigarraga, D. Moser, G. O. Hernandez, P. V. Chiantore, W. Luo, Y. S. Khoo, J. Rabanal-Arabach, E. Fuentealba, P. Ferrada, M. Trigo Gonzalez, J. Ascencio-Vasquez, M. Topic, and M. Jankovec, “Measurement and Simulation of Moisture Ingress in PV Modules in Various Climates,” *IEEE Journal of Photovoltaics*, 2023.

[162] J. Crank, *The mathematics of diffusion*. Clarendon Press, 1979.

[163] R. Puers, “Capacitive sensors: when and how to use them,” *Sensors and Actuators A: Physical*, vol. 37, pp. 93–105, 1993.

[164] Sensirion, “Datasheet-SHT4x,” 2024. [Online]. Available: www.sensirion.com/D1

[165] RS PRO, “Sensors RS PRO Datasheet.” [Online]. Available: https://uk.rs-online.com/

[166] A. K. Apeagyei, J. R. Grenfell, and G. D. Airey, “Application of Fickian and non-Fickian diffusion models to study moisture diffusion in asphalt mastics,” *Materials and Structures/Materiaux et Constructions*, vol. 48, no. 5, pp. 1461–1474, 2015.

A

Current moisture ingress model

A.1. Kyranaki model

Figure A.1 shows the comparison between between the experimental and simulated results from Kyranaki, and the COMSOL simulation on a semi-log graph to highlight the deviation between Kyranaki's simulation and that given by the COMSOL model in the first 10 hours.

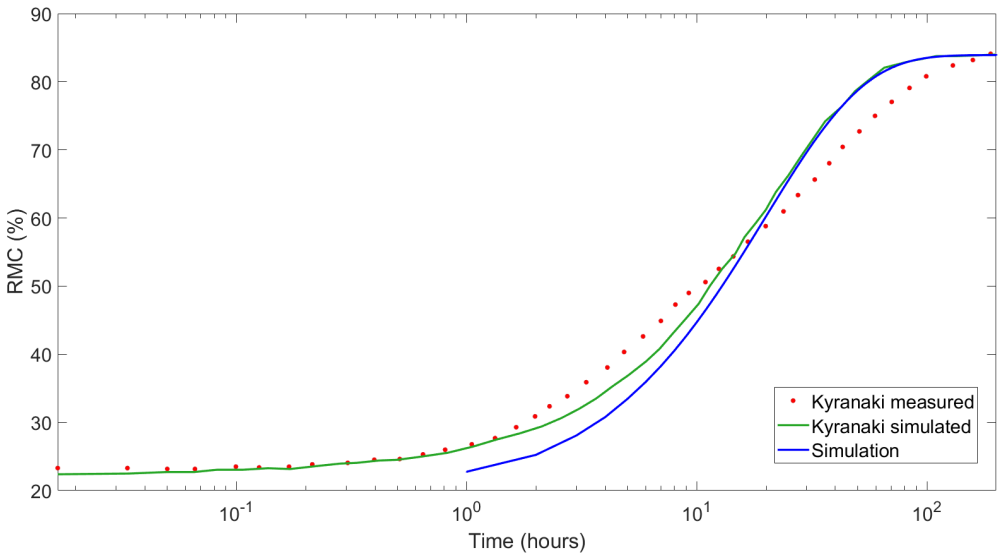

Figure A.1: Comparison between the experimental and simulated results from Kyranaki, and the COMSOL simulation on a semi-log graph.

A.2. Concentration profiles for convergence

This section provides the concentration profiles at locations C-F, over 20 years and a zoomed-in profile for each.

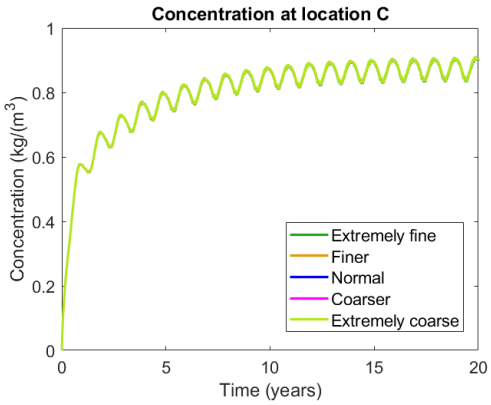

Figure A.2: Concentration at location C for physics-controlled meshes.

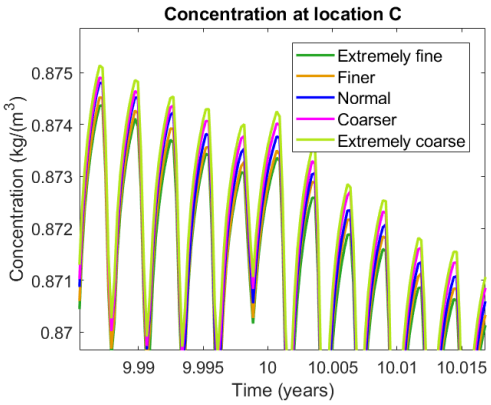

Figure A.3: Magnified segment of concentration at location C for physics-controlled meshes.

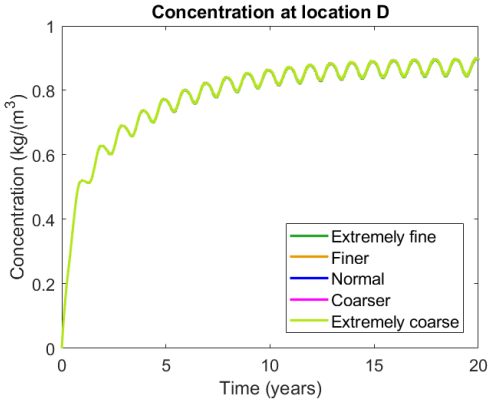

Figure A.4: Concentration at location D for physics-controlled meshes.

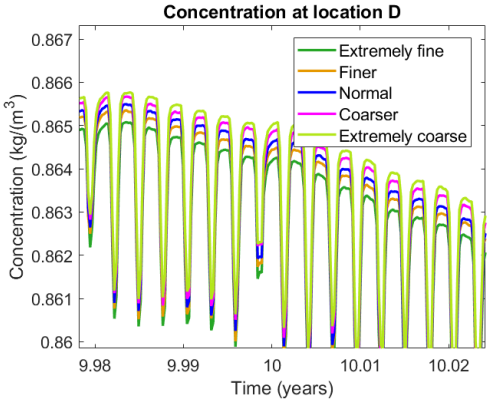

Figure A.5: Magnified segment of concentration at location D for physics-controlled meshes.

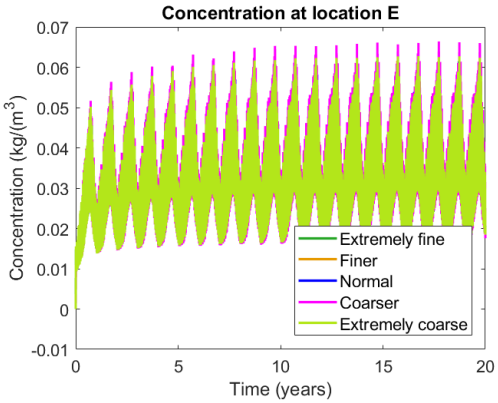

Figure A.6: Concentration at location E for physics-controlledmeshes.

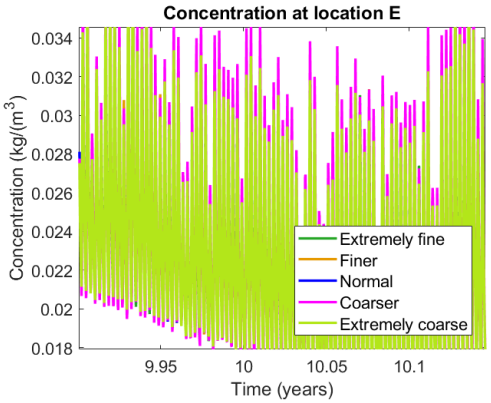

Figure A.7: Magnified segment of concentration at location E for physics-controlled meshes.

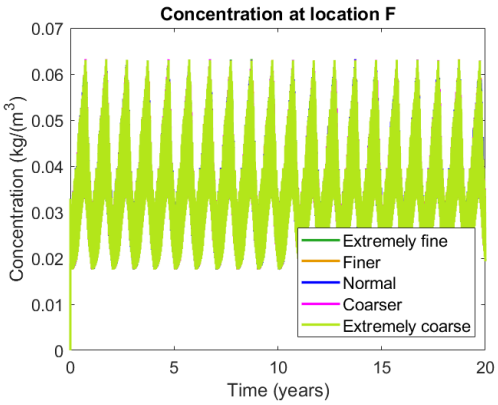

Figure A.8: Concentration at location F for physics-controlled meshes.

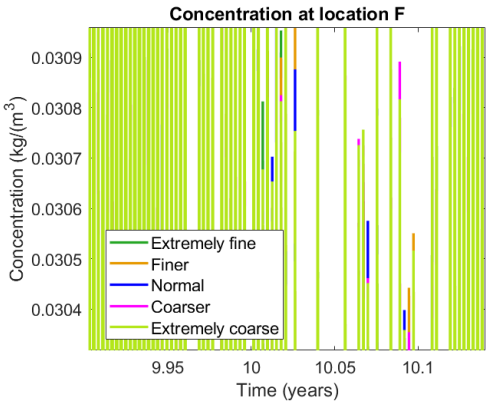

Figure A.9: Magnified segment of concentration at location F for physics-controlled meshes.

A.3. Concentration profiles for optimisation

This section provides the concentration profiles, comparing the results from the *normal* and *optimised* meshes at locations C-F.

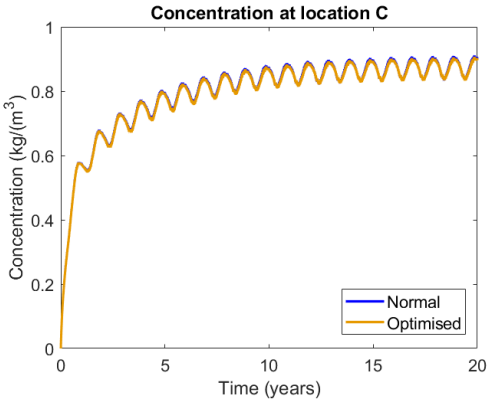

Figure A.10: Concentration at location C for the Normal and optimised meshes.

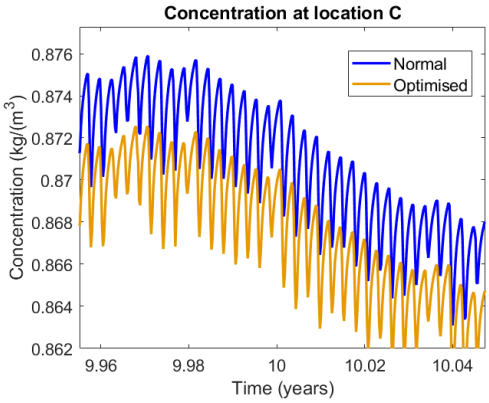

Figure A.11: Magnified segment of concentration at location C for the Normal and optimised meshes.

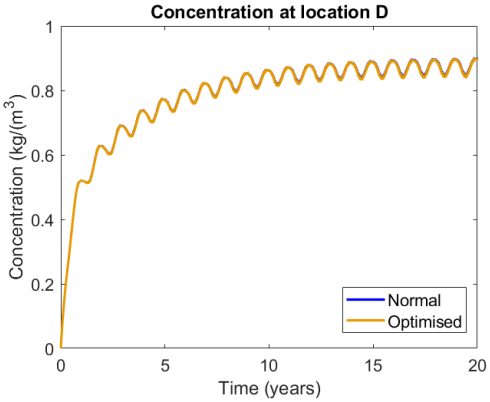

Figure A.12: Concentration at location D for the Normal and optimised meshes.

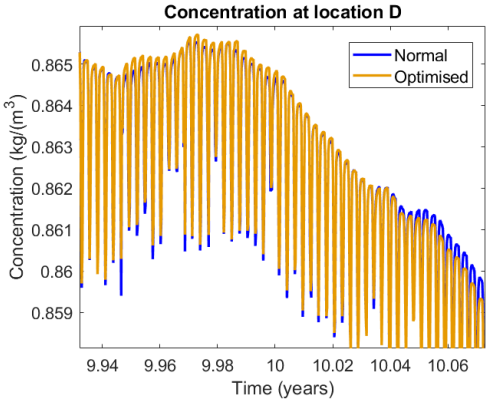

Figure A.13: Magnified segment of concentration at location D for the Normal and optimised meshes.

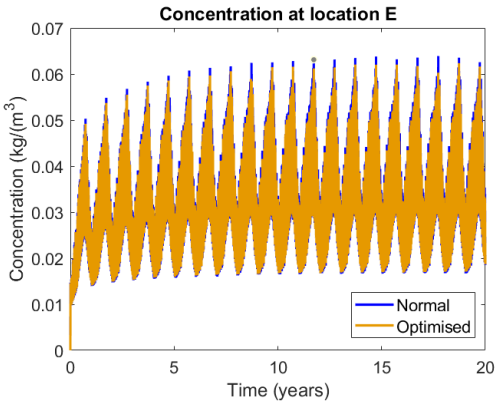

Figure A.14: Concentration at location E for the Normal and optimised meshes.

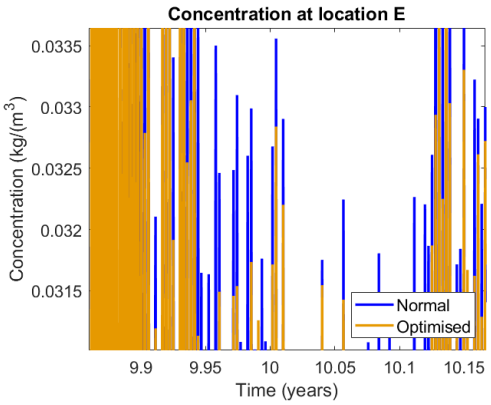

Figure A.15: Magnified segment of concentration at location E for the Normal and optimised meshes.

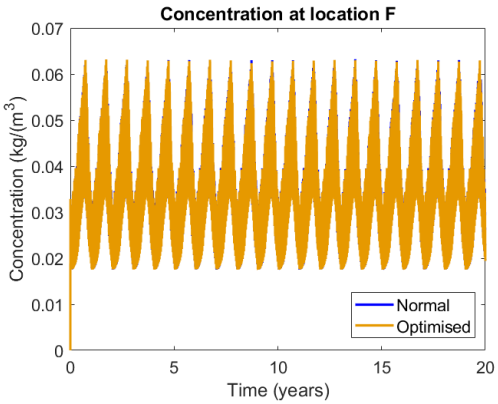

Figure A.16: Concentration at location F for the Normal and optimised meshes.

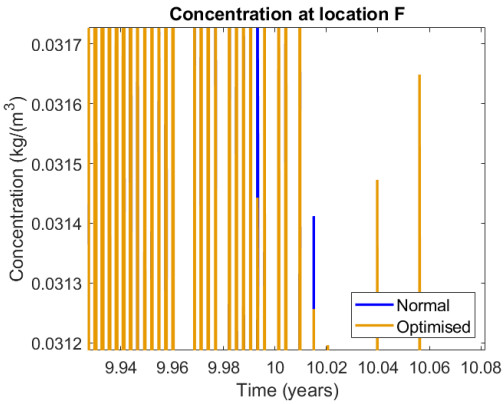

Figure A.17: Magnified segment of concentration at location F for the Normal and optimised meshes.

B

Polymer hydrolysis

B.1. EVA hydrolysis

Moisture in PV modules reacts with encapsulant and backsheet materials, causing them to change the material composition and produce degradation products. This change in the materials is not currently considered in the moisture ingress model, meaning the material composition is the same at the start of the simulation as it is at the end. To adapt the model to better simulate reality, this section considers the degradation reactions and means of integrating them into the model. The focus of this section is on EVA and PET due to their commercial use and previous research, and to compare the findings to Kyranaki's experimental data.

In PV encapsulants, the EVA polymer that is used is composed of ethylene (ET) and 28-33% in weight of vinyl acetate (VAc). The viscous EVA resin undergoes a cross-linking reaction during the lamination process, which thermally cures it and dramatically alters its chemical-physical properties. [128].

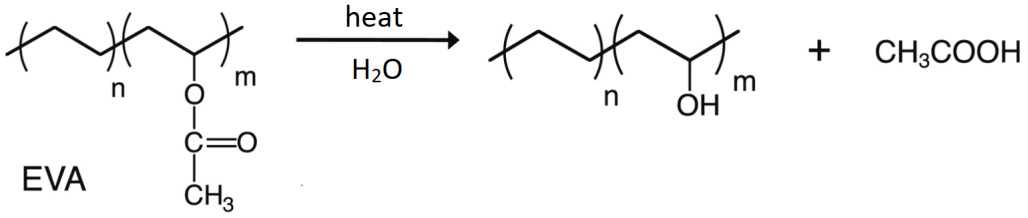

Figure B.1: Hydrolysis of EVA. Adapted from [129].

The types of polymer degradation can be divided into three general categories: (i) without change in molecular weight, (ii) by undergoing chain scission, or (iii) by combining to form higher molecular weight compounds (i.e. cross-linking) [130]. When EVA undergoes hydrolysis, whereby it reacts with water and is broken into two molecules as seen in Figure 3.11, the molecular weight does not change significantly (case (i)). In general, the transformation can be written as:

$$P \xrightarrow{\text{k,EVA}} P^* + S, \tag{B.1}$$

where P is the (native polymer molecule), P^* is the degraded product, k is the rate of reaction, and (S denotes the small molecules produced in the reaction [131]. The rate of change of the chemical species P and P^* is then defined as:

$$-\frac{\mathrm{d}[P]}{\mathrm{d}t} = \frac{\mathrm{d}[P^*]}{\mathrm{d}t} = k[P]. \tag{B.2}$$

The rate of reaction, k, is a function of temperature, according to the Arrhenius law:

$$k = k_0 \text{exp}\left(- \frac{E_a}{RT} \right), \tag{B.3}$$

where $R = 9.314$ [J K^{-1} mol^{-1}] is the ideal gas constant, k_0 [s^{-1}] is a pre-exponential factor, E_a [J mol^{-1}] is the activation energy of the corresponding chemical reaction.

In the case of EVA hydrolysis, Equation 3.5 can be written as

$$\text{EVA} \rightarrow \text{EVOH} + \text{AcOH}, \tag{B.4}$$

where EVOH is ethylene vinyl alcohol and AcOH denotes acetic acid. This equation can be written as a chemical formula as:

$$(\text{C}_2\text{H}_4)_\text{n}(\text{C}_4\text{H}_6\text{O}_2)_\text{m} \rightarrow (\text{C}_2\text{H}_4\text{O} - \text{C}_2\text{H}_4)_\text{x} + \text{CH}_3\text{COOH}, \tag{B.5}$$

where n and m indicate the two repeating units. Diffusive phenomena arise when small molecules are formed together with chemical processes. In this case, a reaction-diffusion model for the species can describe the concentration profile of the small molecules produced, S, as:

$$\frac{\partial [S]}{\partial t} - \Delta (D[S]) = k[P], \tag{B.6}$$

where Δ is the Laplacian differential operator, D is the diffusion coefficient that, in the most general case, might depend upon the concentration of S and temperature, i.e.:

$$D = D_0 \text{exp}\left(- \frac{E_d}{RT} - \gamma [S] \right), \tag{B.7}$$

where the parameters to be determined from experiments are E_d is the activation energy of diffusion and γ is a constant that depends on the concentration of the AcOH [131].

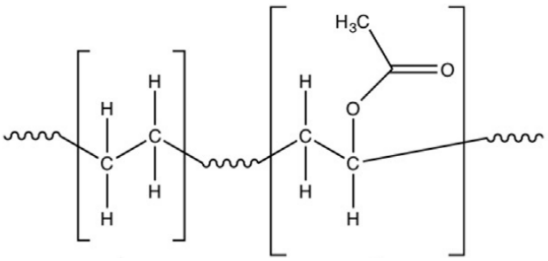

Figure B.2: Chemical structure of EVA. Adapted from [131].

More specifically, the vinyl-acetate monomer undergoes hydrolysis, resulting in the production of acetic acid [23]. The vinyl-acetate can be seen on the right of Figure B.2, with the ethylene monomer on the left.

B.2. PET hydrolysis

Due to its microstructure, PET typically degrades at temperatures above the glass transition temperature, T_g, in humid conditions [132, 133]. PET hydrolysis is a chain-scission reaction, meaning the number of molecules varies over time. The mechanism behind this hydrolysis reaction is not fully understood, but hydrolysis is thought to occur in the amorphous regions of the polymer. The reaction rate depends on the polymer's crystallinity, morphology, relative humidity and temperature [133].

The PET hydrolysis reaction scheme is depicted in Figure 3.12. The reaction scissions the polymer, producing terephthalic acid and ethylene glycol. PET polymers used for PV backsheets typically consist of chains of 100 repeating units. Sammon et al. found that hydrolysis degradation of PET occurs

preferentially at the end of the polymer chain [133], meaning hydrolysis reactions reduce the number of units in a chain, changing the polymer's materials properties and decreasing its molar mass.

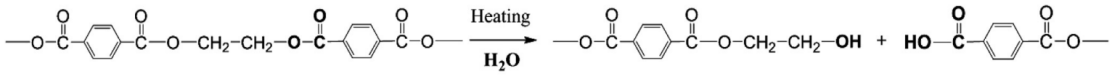

Figure B.3: PET hydrolysis reaction [134].

In this case, the most general reaction scheme is:

$$P \xrightarrow{\text{k,PET}} P^{'} + P^{''}, \tag{B.8}$$

where $P^{'}$ + $P^{''}$ are products of the reaction, the rate of formation of which is equivalent to the rate of consumption of P, i.e.:

$$-\frac{\mathrm{d}[P]}{\mathrm{d}t} = \frac{\mathrm{d}[P^{'}]}{\mathrm{d}t} = \frac{\mathrm{d}[P^{''}]}{\mathrm{d}t} = k[P]. \tag{B.9}$$

The hydrolysis process appears straightforward, but determining the reaction rate numerically is challenging [134]. Several models have been proposed, all of which assume the reaction is thermally activated and follows the Arrhenius law, similar to Equation B.3. During hydrothermal degradation, the relative number of ester groups accessible to water molecules rapidly decreases since the chain scission largely takes place within the amorphous phase. The typical behaviour of a second-order reaction is this positive feedback [134]. For PET hydrolysis, the second-order model proposed takes the following form:

$$-\frac{\mathrm{d}N_t}{\mathrm{d}t} = k[COOR][H_2O], \tag{B.10}$$

where N_t is the number of chain scission per unit mass (mol$\times$g^{1-}) and $[COOR]$ and $[H_2O]$are the concentration in the ethylene glycol and the water (mol$\times$g^{1-}), respectively. Furthermore, the initial microstructure of PET influences the hydrolysis kinetics. For example, water diffusion, and thus hydrolytic degradation, is hindered within the crystalline phase.

C

Accelerated tests/real-life

C.1. Determination of the acceleration factor

Below are the calculations performed to calculate the acceleration factor (AF) between accelerated tests and real life.

C.1.1. IEC accelerated test to real-life

The IEC 60068 damp heat (accelerated) test is (performed to evaluate PV modules as they are influenced by the absorption and diffusion of moisture and moisture vapour.) Below is the calculation performed to obtain the acceleration factor (AF) between the IEC accelerated test and real life.

$$\begin{aligned} AF = \frac{t_{\text{field}}}{t_{\text{test}}} &= \exp\left(\frac{E_a}{R}\left(\frac{1}{T_{\text{field}}} - \frac{1}{T_{\text{test}}}\right)\right) \\ &= \exp\left(\frac{0.7}{8.62 \times 10^{-5}}\left(\frac{1}{293.15} - \frac{1}{358.15}\right)\right) \\ &= 152.5. \\ 152.5 &= \frac{t_{\text{field}}}{t_{\text{test}}} \\ &= \frac{t_{\text{field}}}{1000h} \\ &\Rightarrow t_{\text{field}} = 152546.2 \text{ hours} = 17.4 \text{ years}. \end{aligned}$$

C.1.2. Kyranaki's accelerated test to real-life

Below is the calculation performed to obtain the acceleration factor (AF) between the accelerated test performed by Kyranaki and real life.

$$\begin{aligned} AF = \frac{t_{\text{field}}}{t_{\text{test}}} &= \exp\left(\frac{E_a}{R}\left(\frac{1}{T_{\text{field}}} - \frac{1}{T_{\text{test}}}\right)\right) \\ &= \exp\left(\frac{0.7}{8.62 \times 10^{-5}}\left(\frac{1}{293.15} - \frac{1}{323.15}\right)\right) \\ &= 13.09. \\ 13.09 &= \frac{t_{\text{field}}}{t_{\text{test}}} \\ &= \frac{t_{\text{field}}}{200h} \\ &\Rightarrow t_{\text{field}} = 2617.6 \text{ hours} = 109 \text{ days}. \end{aligned}$$

C.2. Accelerated test to real-life

Figure C.1 shows comparison between the experimental data (red) and simulation of the accelerated test (green) from Kyranaki, and the simulation of real-life based on the calculated acceleration factor (blue). The red x-axis corresponsd to the former, and the blue x-axis to the latter.

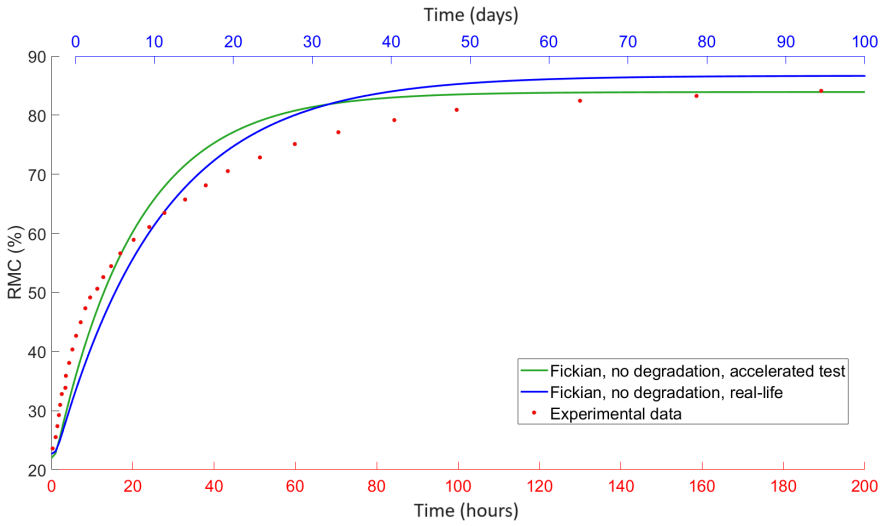

Figure C.1: The comparison between the experimental data (red) and simulation of the accelerated test (green), and the simulation of real-life based on the calculated acceleration factor (blue).

D

Material degradation in different climates

D.1. Simulations of EVA/PET degradation in different climates

This section provides the EVA/PET degradation simulations in different climates.

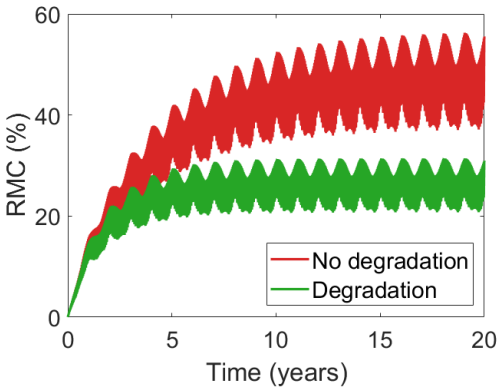

Figure D.1: Average RMC in the EVA encapsulant in Gran Canaria after 20 years, simulating no material degradation and material degradation.

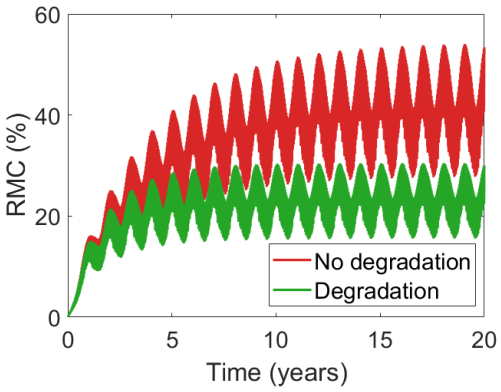

Figure D.2: Average RMC in the EVA encapsulant in Almeria after 20 years, simulating no material degradation and material degradation.

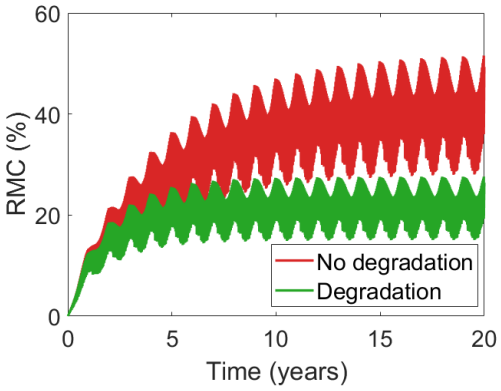

Figure D.3: Average RMC in the EVA encapsulant in LA after 20 years, simulating no material degradation and material degradation.

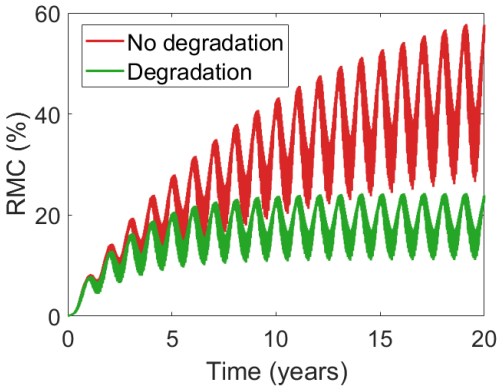

Figure D.4: Average RMC in the EVA encapsulant in Oslo after 20 years, simulating no material degradation and material degradation.

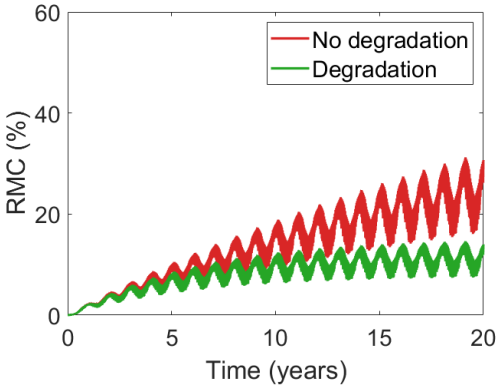

Figure D.5: Avergare RMC in the EVA encapsulant in Zugspitze after 20 years, simulating no material degradation and material degradation.

D.2. Simulations of TPO/PET degradation in different climates with a time-step of 12 hours

This section provides the simulations of the TPO/PET degradation in different climates with a time-step of 12 hours.

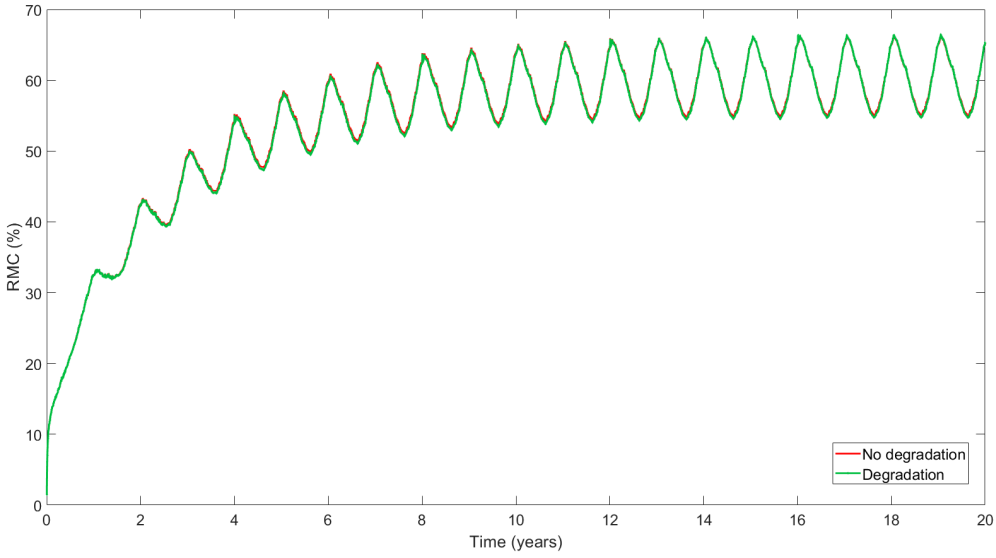

Figure D.6: Avergare RMC in the TPO encapsulant in Gran Canaria after 20 years, with a time-step of 12 hours, simulating no material degradation and material degradation. The non-degradation simulation allows more moisture ingress than the degradation simulation, until around 10 years, after which the degradation has a higher RMC in the winter months.

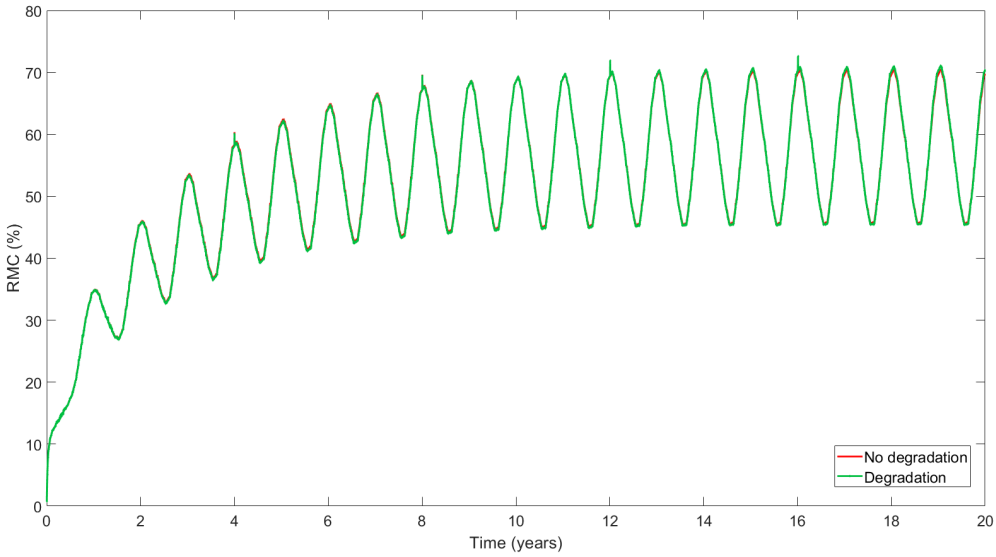

Figure D.7: Avergare RMC in the TPO encapsulant in Almeria after 20 years, with a time-step of 12 hours, simulating no material degradation and material degradation. The non-degradation simulation allows more moisture ingress than the degradation simulation, until around 10 years, after which the degradation has a higher RMC in the winter months.

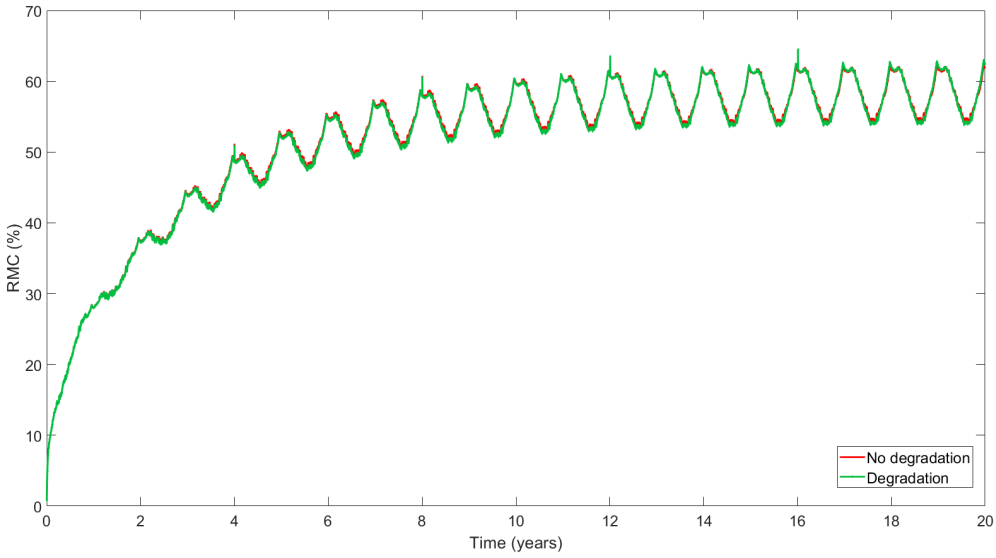

Figure D.8: Avergare RMC in the TPO encapsulant in LA after 20 years, with a time-step of 12 hours, simulating no material degradation and material degradation. The non-degradation simulation consistently allows more moisture ingress than the degradation simulation, except for a short period in winter.

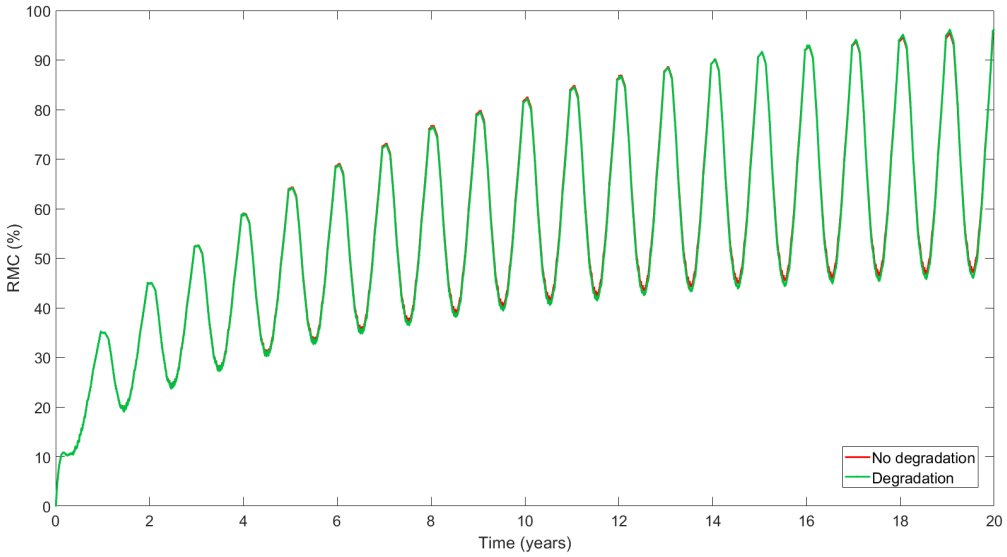

Figure D.9: Avergare RMC in the TPO encapsulant in Oslo after 20 years, with a time-step of 12 hours, simulating no material degradation and material degradation. The non-degradation simulation allows more moisture ingress than the degradation simulation, until around 14 years, after which the degradation has a higher RMC in the winter months.

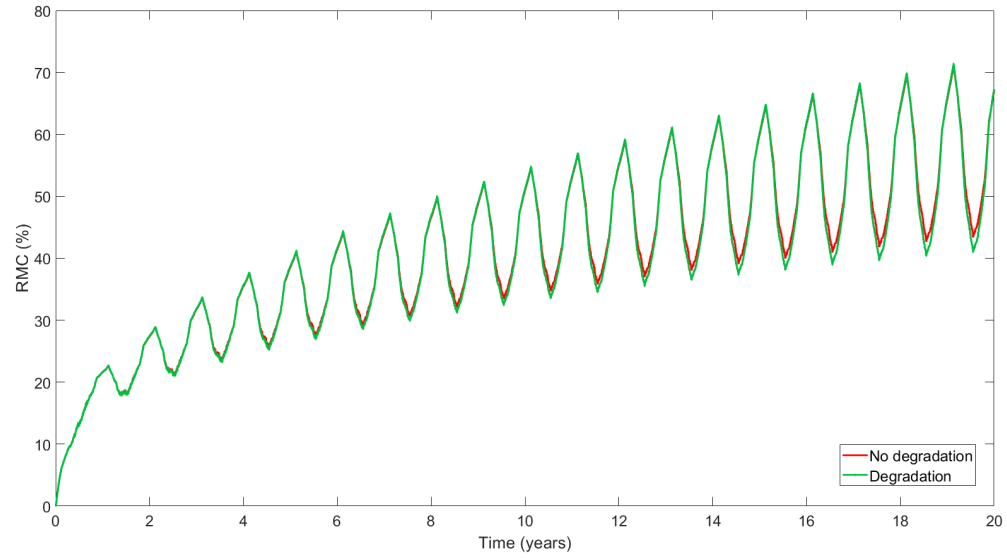

Figure D.10: Avergare RMC in the TPO encapsulant in Zugspitze after 20 years, with a time-step of 12 hours, simulating no material degradation and material degradation. The degradation simulation allows slightly more moisture ingress in the winter months, while the non-degradation simulation allows more in the summer months.

E

Data acquisition

E.1. Sensirion SHT41 humidity sensor

The information in this section is provided by the datasheet for SHT4x humidity sensors from Sensirion [164].

The Sensirion SHT41 humidity sensor uses an I2C interface to communicate information between the sensor and the microcontroller. The functional block diagram (Figure E.1) shows how the data from the SDA AND SCL are processed via the I2C interface.

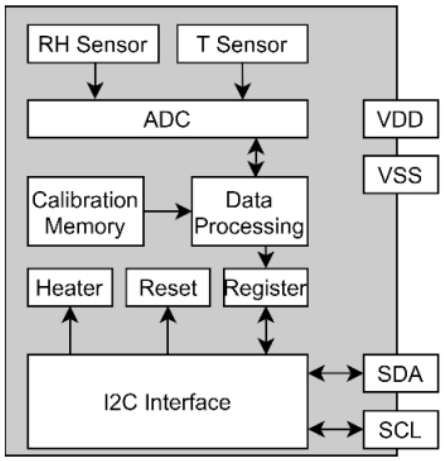

Figure E.1: Functional block diagram of the Sensirion SHT41 humidity sensor.

The digital sensor signals correspond to the following humidity values:

$$RH = \left(-6 + 125 \cdot \frac{S_{RH}}{2^{16} - 1} \right) \%\text{RH}, \tag{E.1}$$

where S_{RH} is the value measured signal. It should be noted that this formula allows values outside the range 0 - 100 %RH, which is non-physical, so the RH signal can be cropped to disregard these values.

Each sensor has a unique serial number, which is stored in the one-time-programmable memory and cannot be manipulated after production.

E.2. RS PRO humidity sensor

The RS PRO humidity sensor measures the change in voltage, from which the change in resistance can be calculated. Resistivity (Ω) is a measure of how much a material opposed the flow of direct current, while impedance (Ω) measures the opposed flow of alternating current, which considers both the resistance and the reactance. For this sensor, the reactance is zero, so its impedance is equal to its resistance. Figure E.2 shows the humidity curve for the RS PRO sensor, which enables the conversion of the measured impedance to the measured relative humidity (%).

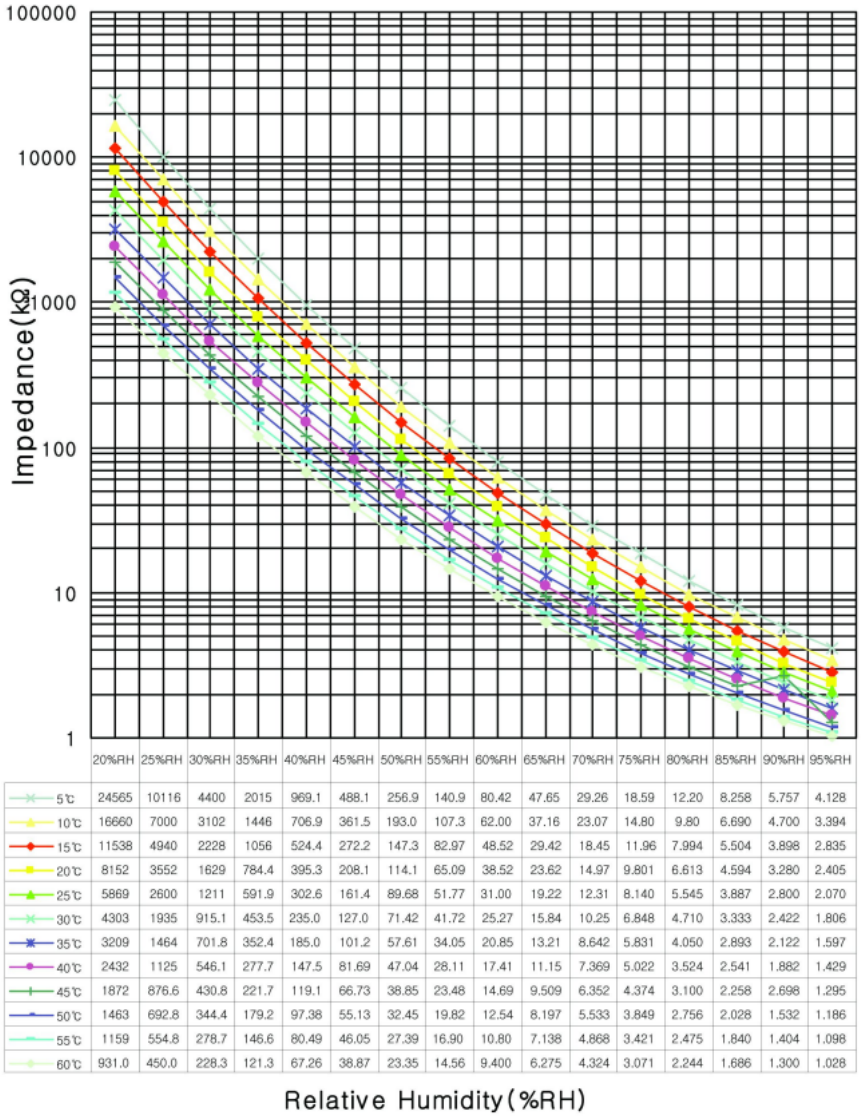

	20%RH	25%RH	30%RH	35%RH	40%RH	45%RH	50%RH	55%RH	60%RH	65%RH	70%RH	75%RH	80%RH	85%RH	90%RH	95%RH
5℃	24565	10116	4400	2015	969.1	488.1	256.9	140.9	80.42	47.65	29.26	18.59	12.20	8.258	5.757	4.128
10℃	16660	7000	3102	1446	706.9	361.5	193.0	107.3	62.00	37.16	23.07	14.80	9.80	6.690	4.700	3.394
15℃	11538	4940	2228	1056	524.4	272.2	147.3	82.97	48.52	29.42	18.45	11.96	7.994	5.504	3.898	2.835
20℃	8152	3552	1629	784.4	395.3	208.1	114.1	65.09	38.52	23.62	14.97	9.801	6.613	4.594	3.280	2.405
25℃	5869	2600	1211	591.9	302.6	161.4	89.68	51.77	31.00	19.22	12.31	8.140	5.545	3.887	2.800	2.070
30℃	4303	1935	915.1	453.5	235.0	127.0	71.42	41.72	25.27	15.84	10.25	6.848	4.710	3.333	2.422	1.806
35℃	3209	1464	701.8	352.4	185.0	101.2	57.61	34.05	20.85	13.21	8.642	5.831	4.050	2.893	2.122	1.597
40℃	2432	1125	546.1	277.7	147.5	81.69	47.04	28.11	17.41	11.15	7.369	5.022	3.524	2.541	1.882	1.429
45℃	1872	876.6	430.8	221.7	119.1	66.73	38.85	23.48	14.69	9.509	6.352	4.374	3.100	2.258	2.698	1.295
50℃	1463	692.8	344.4	179.2	97.38	55.13	32.45	19.82	12.54	8.197	5.533	3.849	2.756	2.028	1.532	1.186
55℃	1159	554.8	278.7	146.6	80.49	46.05	27.39	16.90	10.80	7.138	4.868	3.421	2.475	1.840	1.404	1.098
60℃	931.0	450.0	228.3	121.3	67.26	38.87	23.35	14.56	9.400	6.275	4.324	3.071	2.244	1.686	1.300	1.028

Figure E.2: Humidity curve to convert impedance (Ω) into relative humidity (RH).